

MASTER

Design of a controlled-force grinder for free-form lenses

Ras, M.A.J.

Award date:
2006

[Link to publication](#)

Disclaimer

This document contains a student thesis (bachelor's or master's), as authored by a student at Eindhoven University of Technology. Student theses are made available in the TU/e repository upon obtaining the required degree. The grade received is not published on the document as presented in the repository. The required complexity or quality of research of student theses may vary by program, and the required minimum study period may vary in duration.

General rights

Copyright and moral rights for the publications made accessible in the public portal are retained by the authors and/or other copyright owners and it is a condition of accessing publications that users recognise and abide by the legal requirements associated with these rights.

- Users may download and print one copy of any publication from the public portal for the purpose of private study or research.
- You may not further distribute the material or use it for any profit-making activity or commercial gain

Design of a controlled-force grinder for free-form lenses

M.A.J.Ras

DCT 2006.17

Master's thesis

Coach(es): dr. ir. P. C. J. N. Rosielle, TU/e
dr. ir. H. van Brug, TNO Science and Industry

Supervisor: prof. dr. ir. M. Steinbuch, TU/e

Technische Universiteit Eindhoven
Department Mechanical Engineering
Dynamics and Control Technology Group

Eindhoven, February, 2006

Summary

One of the research areas of the Opto-Mechanical Instruments department within TNO Science and Industry is the fabrication of optical components for scientific and industrial applications. The overall goal is to improve all steps in the manufacturing process that consists of grinding, polishing and measuring. Most of the research is focussed on the production of single piece free-form optics. The polishing research is conducted with the fluid jet polisher, FJP, on which Silvia Booij wrote her dissertation [Boo03]. Rens Henselmans, [Hen05], is currently working on the design of the NANOMEFOS, which will be able to optically measure unique free-form optics with an accuracy of 30 nm.

This thesis will describe an improvement of the grinding process using controlled-force grinding. When controlling the force applied by the grinding tool onto a brittle workpiece, such as glass, it is possible to machine it in a ductile way. Brittle ground optical components contain subsurface damage, which are cracks reaching several μm 's inside the material. The polishing process to remove these cracks is very time consuming and requires an iterative process of polishing and measuring in order to get a good shape accuracy. The grinder of this thesis features a controlled-force tool spindle that is able to limit the amount of force it applies on the workpiece. It will be able to produce optical components with high shape accuracy and a very low amount of subsurface damage. The design of the controlled-force tool spindle is emphasized, so this spindle can be build shortly after completing this thesis and can be used in an experimental setup to investigate the potential of controlled-force grinding on a brittle workpiece.

Contents

Summary	2
1 Introduction	6
2 Goals and conditions	8
2.1 Main goals	8
2.2 Other conditions	9
3 Grinding of optical components	10
3.1 Introduction	10
3.2 Fundamentals of grinding	10
3.3 Trueing, dressing, conditioning	11
3.4 Grinding methods	12
3.4.1 Position-controlled precision grinding	12
3.4.2 Precitech slow tool grinder	13
3.4.3 Controlled-force internal grinding	13
3.4.4 FAUST	14
3.4.5 WAGNER	14
3.5 Subsurface damage	15
3.5.1 Creation	15
3.5.2 Detection	16
3.5.3 Determining the grinding force	16
4 Machine concepts and layouts	19
4.1 Introduction	19
4.2 Unstacked machine concept	19
4.3 Machine layout	19
4.3.1 Introduction	19
4.3.2 Layout 1, T-configurations	20
4.3.3 Layout 2, fixed workpiece spindle, large y-slide	20
4.3.4 Layout 3, fixed workpiece spindle, small y-slide	20
4.3.5 Orientation of the machine layout	21
4.4 Measurement loop	22
4.5 Conclusion	24
5 Tool spindle concepts	25
5.1 Introduction	25
5.2 Controlled-force grinding spindle	25
5.3 Concept 1, using an elastic guideway	25
5.4 Concept 2, using an aerostatic guideway	26
5.5 Comparing spindle concepts	27
5.6 Tool drive measurement	27
5.7 Sealing	28

6	Machine design	30
6.1	Introduction	30
6.2	Machine design overview	30
6.3	Tool drive	30
6.3.1	Tool drive assembly	30
6.3.2	Tool drive components	32
6.4	Tool spindle	34
6.4.1	Spindle assembly	34
6.4.2	Tool spindle components	35
6.4.3	Motor stator	38
6.4.4	Toolholder front	38
6.4.5	Toolholder back	40
6.5	Tool disk	40
6.5.1	Tool disk assembly	40
6.5.2	Tool disk components	40
6.6	Y-slide	41
6.6.1	Y-slide assembly	41
6.6.2	Y-slide components	42
6.7	X-slide	44
6.7.1	X-slide assembly	44
6.7.2	X-slide components	44
6.8	Base	48
6.8.1	Base assembly	48
6.8.2	Base components	49
7	Conclusions and recommendations	52
7.1	Conclusions	52
7.2	Recommendations	52
	Bibliography	54
	Symbol list	57
A	Assembly drawings	58
B	Summary machine properties	62
C	Tool spindle cost	63
D	Dynamical model	64
E	FEM-calculations	67
E.1	Introduction	67
E.2	X-frame	67
E.3	Vacuum seal	67
E.4	Membranes	70
E.5	X-frame airbearings	70
F	Calculations	72
F.1	Stiffness related to overhanging length	72
F.2	Tool spindle accuracy model	72

G	Alternative machine designs	76
G.1	Alternative 1	76
G.2	Alternative 2	77
G.3	Alternative 3	79
G.4	Alternative spindle design	80
G.4.1	Alternative spindle design 1	80
G.4.2	Alternative spindle design 2	80
H	Materials	82
H.1	Optical materials	82
I	Data sheets	83

Chapter 1

Introduction

Optical components, like lenses and mirrors, are made to manipulate the propagation of light rays so they can be used to measure objects, as done with interferometry, or to manufacture products, for example making IC's using lithography. To achieve a good optical performance first of all a material must be chosen with the right physical properties. This material is then to be shaped into its desired form. One of the ways of shaping optical components is grinding. Grinding is often used with very hard materials, such as glass. The grinding method must provide a number of things, starting with a high shape accuracy to ensure a high imaging performance. Also the surface must be smooth enough to avoid scattering and the amount of subsurface damage has to be low to avoid deterioration if the lens is used with high power laser beams, [Fäh99].

There is an increasing demand for free-form shaped lenses. An aspherical lens for example can avoid geometrical aberrations and this will reduce the number of lenses needed for an application, thus reducing the number of optical surfaces and absorption. This way the required space inside an application is also reduced. The processes to polish and measure free-form lenses are currently being developed, [Booo3],[Hen05].

Subsurface damage arises when the grinding process takes place in brittle mode, see chapter 3. The problem with this kind of damage is that it is possible for chips to break out of the lens when it is being used, reducing its quality significantly. The damage also increases the amount of light absorbed by the lens, causing the lens to heat up which is undesirable for a lot of applications. The lens is polished to remove the subsurface damage, but this will decrease the shape accuracy, because most polishing processes have an averaging effect on the surface form. This also is a very time-consuming process with repeatedly polishing and measuring.

Grinding glass into free-forms without leaving subsurface damage using position-controlled machines is very challenging with currently available machines, because it requires a depth of cut smaller than one tenth of a micrometer. Because of machine vibrations and height variations of the roughly ground workpiece, even if the infeed is set small enough, the critical depth of cut is often exceeded. Another problem is wear of the abrasive grains. Sharp grains can cut away material of the workpiece with a very small normal force pressing them into the workpiece. When the grains dull, they tend to rub more and cut less, so a larger normal force is necessary to achieve the desired depth of cut. When the normal force reaches a value that is larger than the force correlated to the critical depth of cut, brittle fracture and subsurface damage occur.

This thesis will discuss the design of a grinding machine that uses a controlled-force grinding method. The force at which subsurface damage arises is, depending on the tool used, around 1 N. By on one hand positioning the tool accurately and on the other hand ensuring the normal force on the workpiece never exceeds 1 N, it should be possible to produce an accurately shaped lens without subsurface damages. The machine accuracy is necessary only for the shape accuracy of the workpiece,

not for limiting the grinding force. This way a larger machine error can be allowed, this will not lead to subsurface damage.

At the locations where the force would be larger than 1 N if position-controlled grinding was applied, the shape will differ from the desired shape. This is shown in figure 1.1. In previous grinding steps the workpiece surface was ground into the shape as shown with the dotted line. A depth of cut, d_{set} , is set to reach the final shape given by the straight dashed line. However, because d_{set} is larger than the critical depth of cut d_{crit} related to the maximum allowable grinding force, the desired shape is not achieved in one step. A lump still remains on the left part of the figure. Most of the right part of the figure did reach its final shape. If this lump is small enough, so the desired shape accuracy is achieved, the grinding process is complete. Else an extra step is necessary.

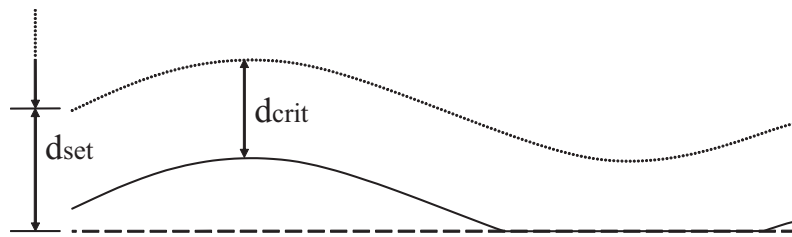


Figure 1.1: Controlled force toolpath

Chapter 2

Goals and conditions

2.1 Main goals

Controlled force

The primary objective of this grinder is to control the force applied by the tool onto the workpiece. This can be done by controlling the position of the tool relative to the workpiece very accurately, but this is very difficult, because a depth of cut of about 10 nm is necessary. There have been done experiments with a position-controlled grinder grinding in ductile mode, [Bif91], but this has only been applied on flat workpieces, not with free-form ones.

Because controlling the grinding force is difficult with a position-controlled grinder, a design will have to be made that will allow the grinding force to be set. This way the position of the tool and the grinding force are no longer related. The tool is positioned to a desired depth of cut and the tool tip can vary somewhat in position so the force on the tool tip can be lower than the set maximum. The workpiece can push the tool away, to avoid the grinding force to become too large. If the position variation of the tool tip is so large that the shape accuracy is not achieved, another grinding pass is needed. Extra time is then needed to grind the workpiece, but it does not suffer from subsurface damage.

Free-form surfaces

Free-form optical components can have many advantages compared to rotational-symmetric components. They allow light to be manipulated using less optical surfaces. The grinder must be able to grind such surfaces. Because many lenses are (almost) rotational-symmetric, even the free-form ones, a machine layout has to be chosen that is best suited for this kind of workpieces. This grinder can be less suited for entirely non-rotational-symmetric components such as cubes and prisms.

Shape accuracy

Currently a maximal accuracy of 1 μm is achieved, when grinding rotational-symmetric lenses. Experiments on grinding free-form lenses with a grinder built for rotation-symmetric lenses resulted in far less accurate workpieces. The goal for this machine is to produce lenses with an error less than 1 μm . This means that the produced axis of rotation of the workpiece should not be more than 1 μm away from the desired axis of rotation. Also the height variations should be less than 1 μm .

Tool spindle unit

There are plans to first build the tool spindle and use it on an existing platform, e.g. a milling machine. This way experiments can be done to analyze the potential of controlled-force grinding. Therefor the

tool spindle should be designed as a stand-alone unit that can be placed onto a platform as a whole. To get a good shape accuracy during these experiments, the position of the tool relative to the tool spindle housing should be measured with $0.2\ \mu m$ accuracy.

2.2 Other conditions

Most glass lenses that are currently being produced have a diameter of less than 200 mm. Therefore this diameter was set as the maximum diameter for the grinder. Because this grinder will be used for experiments to examine the possibility of controlled-force grinding, a high production rate is not an important issue. It must show the potential of controlled-force grinding. To optimally control the grinding process it is important to have a stable grinder with a good dynamical behaviour. This means material has to be used in an optimal way, resulting in stiff machine components with a limited weight. Critical components are to be statically determined.

Chapter 3

Grinding of optical components

3.1 Introduction

In this chapter the basics of grinding are explained. First is examined how forces act on an individual abrasive grain, then the forces on the entire grinding tool are shown. To get a tool that has a defined geometry with sharp grain, it needs to be trued and dressed. Further a number of grinding methods are discussed, to give the reader an overview of the different grinding processes. Finally the creation and detection of subsurface damage is discussed.

3.2 Fundamentals of grinding

Like all classes of machining, grinding is used to remove unwanted material from the workpiece [Hegoo]. An abrasive surface is pressed against the workpiece and by mechanical action of the abrasive grains, material is removed, shown in figure 3.1. A grain is moved into the workpiece with tool speed v_t . A normal force F_n pushes the grain into the workpiece, while the cutting force F_c removes material. Usually diamonds bonded in bronze are used for grinding glass. For the design in this thesis a cup wheel is chosen, because it can be used to grind small concave areas, shown in figure 3.2. The normal grinding force in these wheels can be almost perfectly axial, which is best suited for the concept used, described in chapter 5. F_c is pointing into the paper. The angle α is best kept low to reduce the influence of roundness errors and to minimize bending of the tool.

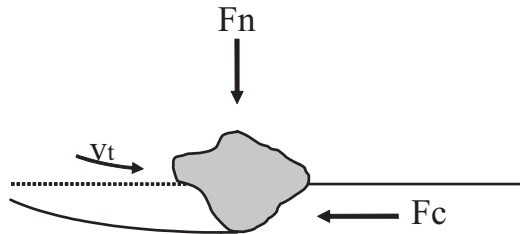


Figure 3.1: Forces on cutting grain

When an abrasive grain comes into contact with the workpiece, there are four different deformation mechanisms that can occur, providing the grain is not pulled from its bond. Figure 3.3 shows these four mechanisms. Ploughing (a) occurs when a grain is not sharp enough or is not deep enough

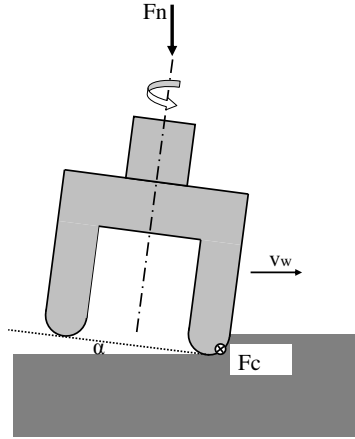


Figure 3.2: Forces on cutting cupwheel

into the workpiece to remove material. Instead material in front of the grain is pushed forward and sideward. This way a scratch is made, but no material is removed. Ideally the grains are cutting material from the workpiece and the surrounding material is unmoved (b). As a result of repeated ploughing micro-fatigue may take place (c). Finally when grinding brittle material, like glass in brittle mode, cracking can occur (d). Material from an area larger than the cutting area of the abrasive grain is removed. This leaves a rough surface and subsurface damage. Cracking is the only brittle deformation mechanism, so the other three are to be expected when grinding glass in ductile mode.

3.3 Trueing, dressing, conditioning

To achieve a ground product with a good form and finish it is necessary to true and dress the grinding wheel regularly, [Sha96]. In most cases the manufacturer of the wheel has balanced it, but for this type of grinding it will be needed to balance the wheel in the machine. This way the misalignment to the axis of rotation of the tool spindle, due to the mounting of the tool, can be compensated.

The process of removing material from the grinding surface of the tool and giving it a defined shape is called trueing. This way the runout will be decreased. However it also flattens some of the outer grains in order to reach the defined geometry. After trueing the tool needs to be sharpened.

The process to sharpen the active grids by removing wear flats and the bond material is called dressing. Finally conditioning is used to open up spaces between the active grid so chips can be accommodated. For super abrasive wheel this is mostly done by plunging an Al_2O_3 abrasive stick into the wheel and this way scratching out the softer bond material between the abrasive grid.

Currently grinders are being designed that are able to continuously dress their tools while grinding, [Qiao4]. This ELECTrolytic In-process Dressing, ELID, uses electric current to erode the bond material from the tool in a controlled way. This way dull grains are removed and the tool stays in optimal grinding condition.

Because ELID grinding is a complex process, that still needs research to get the desired results, it is not taken into account in this thesis. The major new feature of this grinder is controlled-force grinding.

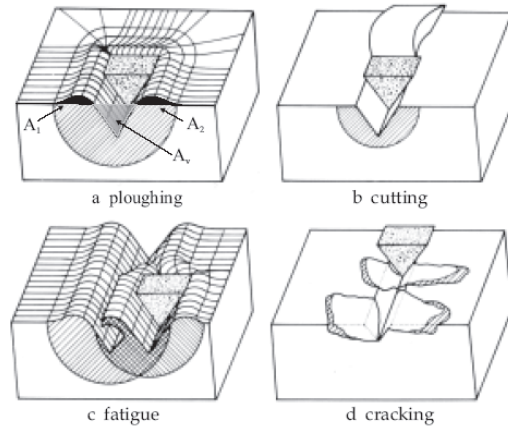


Figure 3.3: a) ploughing, b) cutting, c) fatigue, d) cracking

3.4 Grinding methods

3.4.1 Position-controlled precision grinding

One way to avoid subsurface damage is to build a high precision grinder and by using a very small infeed limiting the grinding forces. This requires a very stiff machine which drives must be able to be positioned very accurately. [Bif91] built an experimental setup (PEGASUS) for ductile grinding by placing the tool spindle onto an elastic guideway. The infeed is controlled by a piezoelectric actuator with a resolution of 2 nm over a range of 10 μm . Using PEGASUS it was possible to plunge grind fused silica with an infeed of 2 nm per revolution leaving a ductile cut surface. This illustrates the small infeed needed to grind in ductile mode. When plunge grinding the tool wheel used is much larger than the workpiece. This way no radial movement is necessary to make flat workpieces.

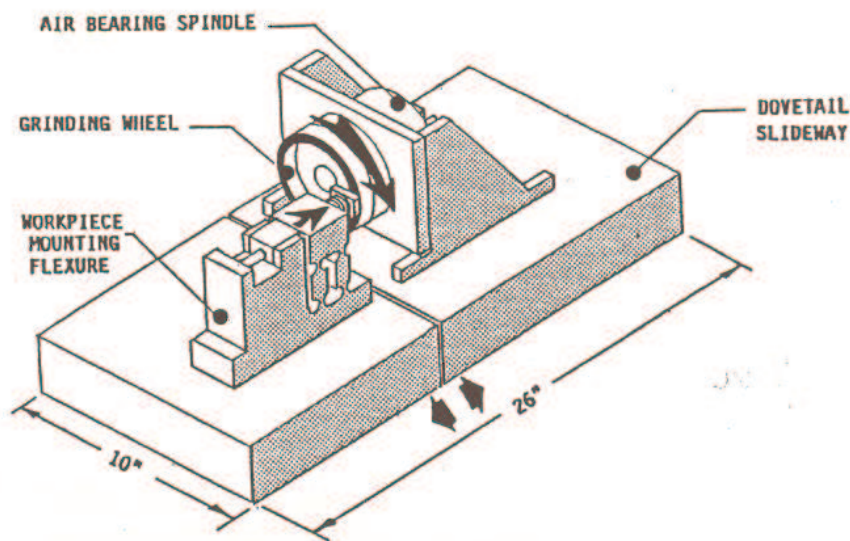


Figure 3.4: Position controlled grinding with Pegasus

Expansion of machine components by an increase in temperature causes position errors if not

properly dealt with. For the design of a grinder to grind flat optical and electronic parts, [Nam89] used a Zerodur tool spindle. Zerodur is a glass with a very small thermal expansion coefficient. Despite the low modulus of elasticity compared to steel, a flatness of $0.2 \mu\text{m}$ is achieved on an area of 18×18 mm.

The two processes described above are capable of grinding only flat surfaces. A grinder for the manufacturing of aspheric mirrors with maximal dimensions of $500 \text{ mm} \times 500 \text{ mm}$ was designed by [Suz95]. To reduce the influence of vibrations from the tool spindle motor on the workpiece, a viscous coupling between this motor and the grinding wheel spindle was designed. The slides are driven by ball screws, which are mounted to the slides with flexible couplings, so only thrust is applied. This is necessary to avoid an overconstrained slide position and gain good accuracy, [Sch98]

Another precision position-controlled grinder is designed by [Qiao4], this project is called Nano grind. The grinder is a high precision 5-axis machine integrated with ELID technology. This 'Electrolytic In-process Dressing' makes it possible to continuously keep the tool in optimal cutting condition, by eroding the bonding material in a controlled way, so dull grains can be pulled out by the workpiece. This way the grinding force is mostly prescribed by sharp grains, so the grinding force is kept at a low value. This design also features an in-situ measurement device, so the position of the tool and workpiece can directly be measured.

3.4.2 Precitech slow tool grinder

The Precitech Nanoform high precision turning machine owned by TNO, can be equipped as a grinder by removing the diamond tipped chisel and placing an extra air spindle containing the grinding wheel. Figure 3.5 shows this setup with the large workpiece spindle at the left part of the picture. The grinding spindle is placed vertically so the grinding wheel is pushed radially into the workpiece. Please note that a very small diameter wheel is used. The Nanoform also features a slow tool servo machining option. This type of servo is particularly suited for machining non-rotational continuous surfaces, because of the long stroke and low acceleration - 10 mm at 2 Hz - compared to a fast tool servo consisting of a piezo actuator and flexure elements. Fast tool servos are mostly used for discontinuous surfaces, because they are capable of large accelerations. Two translations, namely radial and axial to the workpiece, and rotation of the workpiece are sufficient to grind all sorts of free-form optics with this grinder setup. The angle between the workpiece spindle axis and the tool spindle axis does not have to be altered.

Precitech has investigated the performance of the slow tool servo precision turning a 2 mm tilted copper flat, $\varnothing 50 \text{ mm}$. With an infeed of $10 \mu\text{m}/\text{rev}$ a shape accuracy of $< 0.25 \mu\text{m}$ has been achieved. This result was made by turning, not by grinding. The first difference between the two processes is that the turning setup contains far less mass than the grinding setup. The turning setup contains the chisel and a small mounting frame, while the grinding setup contains an airbearing spindle and a larger mounting frame. So the speed of the slow tool servo would be much lower than the specification given. Also a decrease in stiffness is to be expected because of the longer structural loop and because the tool is being bent. Especially when a slim tool is used as shown in figure 3.5 the radial grinding force should be very small to limit tool deflections and achieve a good shape accuracy.

3.4.3 Controlled-force internal grinding

A problem described by [Hah64] when internally grinding for example cylinder bores, is that when the tool is radially moved away from the centre line, the grinding forces between the tool and workpiece causes the tool to bend, see figure 3.6. When this is done with a constant velocity, the grinding forces may differ depending on the sharpness of the grains, the local hardness of the workpiece etc. Because of this, the bending of the tool is also varying, so it is difficult to predict the taper of the bore, the surface quality and the final diameter. These problems can be solved by applying a constant force onto the tool, which is pushed in radial direction. This way the bending of the tool can be predicted. When the desired diameter is achieved the tool slide is stopped by an end stop.

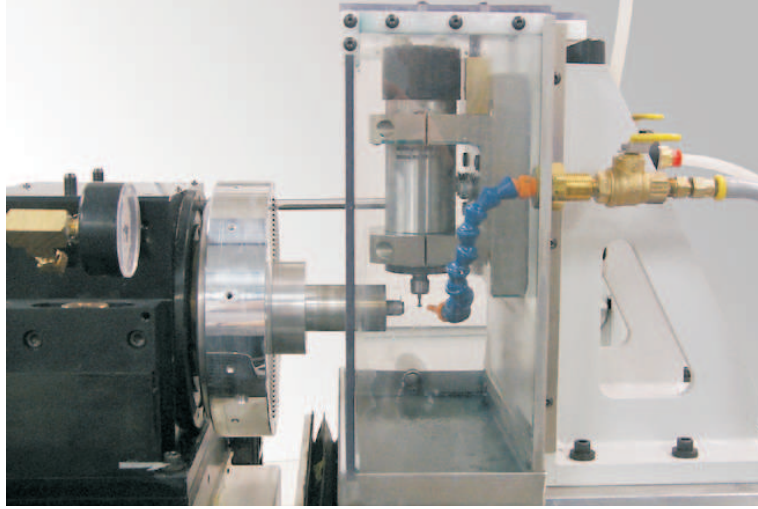


Figure 3.5: Precitech's aspheric grinding setup

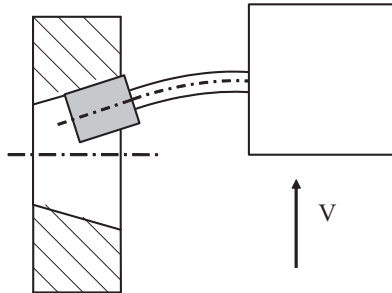


Figure 3.6: Deflection by uncontrolled grinding force with constant tool speed V

3.4.4 FAUST

Oliver W. Föhnle, [Föh98], describes in his dissertation the fabrication technique 'Fabrication of Aspherical Ultra-precise Surfaces using a Tube (FAUST)'. This method uses the edge of an elliptically shaped tube to grind parabolic and hyperbolic surfaces. Figure 3.7 shows the tool T having an angle α with workpiece W . By choosing the right rotational speeds of the workpiece ω_1 and the tool ω_2 , after a certain time all the grinding points on tube M have been in contact with the entire workpiece surface. During grinding the tool will be moved into $-z$ direction until the desired shape is acquired. So only one degree of freedom is actuated during grinding and this is done by using a spring. This way the tool is pressing against the workpiece with a constant force until it reaches its end stop.

3.4.5 WAGNER

A machining tool based on the same concept as FAUST is 'Wear-based Aspherics Generator based on a Novel Elliptical Rotator (WAGNER)'. This tool consists of a small diameter cup wheel that is placed on a pantograph. The pantograph describes the elliptical trajectory for the cup wheel. By choosing

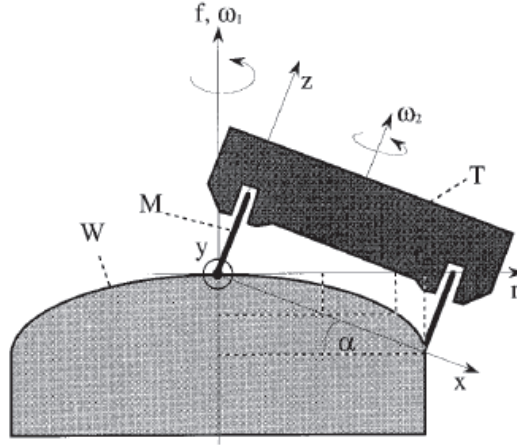


Figure 3.7: Functional principle of FAUST

the right rotational speeds of the workpiece and the pantograph, any positional errors of the tool are averaged over the whole workpiece surface. Again the tool is pressed onto the workpiece with a constant force until it reaches an end stop, just as with FAUST. This way an excellent workpiece shape can be manufactured. B. Bollen has wrote his thesis on the design of a grinder using the WAGNER concept, [Bol99]. This assignment was conducted for TNO.

3.5 Subsurface damage

3.5.1 Creation

An abrasive grain pressing onto the workpiece will plastically deform the material until the contact area is large enough to support the load, [Fäh98], [Law95]. This is similar with making an impression with a sharp indenter. When the indenter applies pressure there will be a plastically deformed zone as shown in figure 3.8. Increasing the pressure further will lead to the generation of two types of cracks, if the load exceeds a critical value. A radial crack will grow deeper into the material. These cracks are the cause of subsurface damage, which need to be removed by polishing. The other type of crack is a lateral one. This crack will expand and widen when the load is released. When it reaches the surface a chip is removed in brittle mode leaving a rough surface, as shown in subsection 3.5.2 . The type of cracks formed this way differ entirely from cracks formed with a blunt indenter, so called "cone-cracks", [Fis00].

If the energy introduced by the indenter remains below the energy needed to initiate a crack, material can be removed by viscous flow (ductile material removal) instead of brittle fracture. The energy E_p needed for plactical material deformation is proportional with the deformed volume and the energy E_c needed for the generation of a crack is related to the crack area. The ratio of the two energies can be written as

$$\frac{E_p}{E_c} \propto d \quad (3.1)$$

where d is the penetration depth of the deformation. This shows that with a sufficient small d it is energetically favorable for the material to deform plastically. [Bif91] and [Booo3] show that the critical penetration depth d_c can be determined with

$$d_c = 0.15 \left(\frac{E}{H} \right) \left(\frac{K_c}{H} \right)^2 \quad (3.2)$$

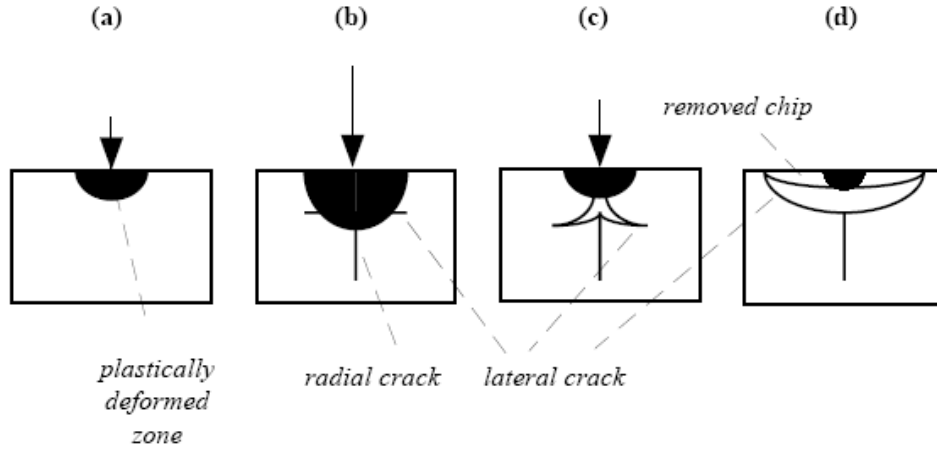


Figure 3.8: Crack generation beneath a sharp indenter

For BK7 with an E-modulus $E=81 \text{ GPa}$, a fracture toughness $K_c=0.86 \text{ MPa}\sqrt{\text{m}}$ and a hardness $H=5.2 \text{ GPa}$, this gives $d_c=64 \text{ nm}$. Because of this very shallow d_c it is very hard to apply a depth of cut small enough. Machine vibrations and local height variations of the workpiece can temporarily cause the depth of cut to be too deep and this will result in subsurface damage.

3.5.2 Detection

To investigate the amount of subsurface damage on a given optical component, a number of measuring techniques are available. One often used technique is the dimple method, where the surface of the component is etched revealing the damage. This is however not a very convenient measuring method, because it destroys the optical surface and the hydrofluoric acid used is very aggressive. [Lam97] and [Pau87] have studied the relationship between the amount of subsurface damage and the surface roughness. [Lam97] tested a number of lapped, optical glasses and showed that the subsurface damage is proportional with the surface roughness, peak-to-valley. For BK7 the surface roughness is 3 to 5 times the amount of subsurface damage. This is only valid for relative high surface roughness values, about $1 \mu\text{m}$ rms or more. At lower roughness values the grinding process has been in ductile mode. This allows a different way to determine if subsurface damage may or may not exist on a particular workpiece sample. [Fano4] examined BK7 that was cut by high precision diamond turning. Figure 3.9 shows a brittle cut surface caused by an infeed of $2 \mu\text{m}$ and a ductile surface with an infeed of $0.6 \mu\text{m}$. The power spectral densities giving the spatial frequencies of the surfaces, show that the brittle mode holds more high frequencies. So examining the sample surface shows whether it was cut brittle or ductile.

3.5.3 Determining the grinding force

To get a better understanding of the grinding process, different kinds of models were developed. The model proposed by [You87] describes three mechanisms that occur during chip formation, namely ploughing, cutting and rubbing. The model is described using the chip thickness coefficient, the friction coefficient between the grit tip area and the workpiece, the stress coefficient arising during ploughing and finally the loading coefficient. These coefficients are determined for specific configurations during normal grinding operations. The coefficients will therefore be different for different configurations i.e. grinding other materials, with another tool etc. However this model gives a good insight in the relationship between the parameters. The model for F_n is given in 3.3 and consists of the normal cutting force, F_{nc} , the normal rubbing force, F_{nr} , and the normal ploughing force, F_{np} .

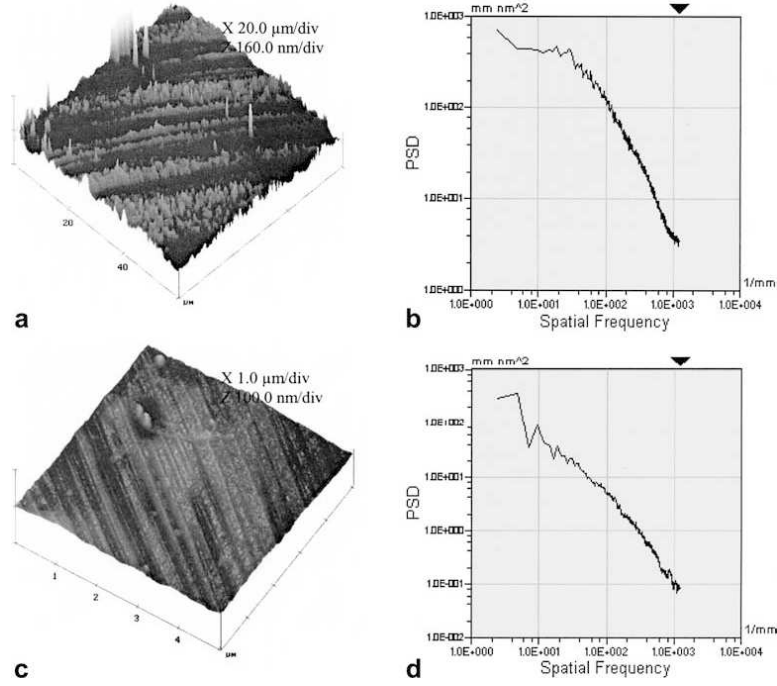


Figure 3.9: a) brittle mode, b) power spectral density of brittle mode, c) ductile mode, d) psd of ductile mode

$$F_n = F_{nc} + F_{nr} + F_{np} \quad (3.3)$$

$$F_{nc} = wk_1 \frac{v_w}{v_g} S_n - L_a \frac{k_1 v_w}{100 v_g} S_n \quad (3.4)$$

$$F_{nr} = w L_a K_L l_c \quad (3.5)$$

$$F_{np} = w \alpha_f \frac{v_w}{v_g} l_c - w L_a \alpha_f \frac{v_w}{v_g} L_c \quad (3.6)$$

w	width of cut	$[m]$
k_1	chip thickness coefficient	$[\frac{N}{mm^2}]$
v_w	speed workpiece	$[m/s]$
v_g	speed grinding tool	$[m/s]$
S_n	Depth of cut	$[m]$
L_a	Loaded area / Total tool area	$[-]$
K_L	Loading force coefficient	$[\frac{N}{unitLa}]$
L_c	Contact lenght	$[m]$
α_f	ploughing grain coefficient	$[\frac{N}{mm^2}]$

With w the width of cut. The chip thickness coefficient, $k_1 [\frac{N}{mm^2}]$ gives the connection between the chip surface and the cutting force. $v_w [\frac{m}{s}]$ and $v_g [\frac{m}{s}]$ are respectively the speed of the workpiece and the speed of the grinding tool. The depth of cut is given by S_n . $L_a [-]$ is percentage of the total area that is loaded, i.e. the part of the total tool surface that actually makes contact with the workpiece. L_a is time dependent because initially sharp grains will flatten during grinding and thus increasing the loaded area. $K_L [\frac{N}{unitLa}]$ is the loading force coefficient, which gives the connection between the tip area contact of the grains and the rubbing force. L_c is the contact length between grains and workpiece. Finally $\alpha_f [\frac{N}{mm^2}]$ is the coefficient that is determined by the ploughing grain geometry. This

coefficient gives the relation between the surface of the ploughing grains and the required force.

The model determined by [You87] shows many parameters that depend on the workpiece and tool material, grain shapes, coolant used etc. All these coefficients are best to be determined by grinding experiments, which were not conducted during this thesis project.

A more simple model is used to determine the maximum force, so the specifications of the actuator that will supply that force can be acquired. Figure 3.7 shows the cup wheel with angle $\alpha = 0$, in this way the contact area is as large as possible. All of the active tool area is in contact with the workpiece, not only the grain tips. Individual grains are not considered. When looking at the bottom side of the tool, one can see the contact area, which is a semi-circle band with width L_c . Because of $L_c \ll R_2$, L_c is considered to be a straight line. The maximal depth of cut $d_{max} = 1\mu m$. The contact area A_c can now be determined with

$$A_c = \frac{\pi}{2}(R_1 + L_c)^2 - \frac{\pi}{2}R_1^2 \quad (3.7)$$

$$L_c = \sqrt{2R_2d_{max}} \quad (3.8)$$

Using [Couo4] who determined the grinding forces when machining 416 stainless steel, which has a slightly higher hardness than glass, a grinding pressure p can be determined. The pressure when grinding the steel with a depth of cut of $1\mu m$ is $p = 870kPa$. Using equation 3.10 a maximum grinding force of 1.3 N is achieved.

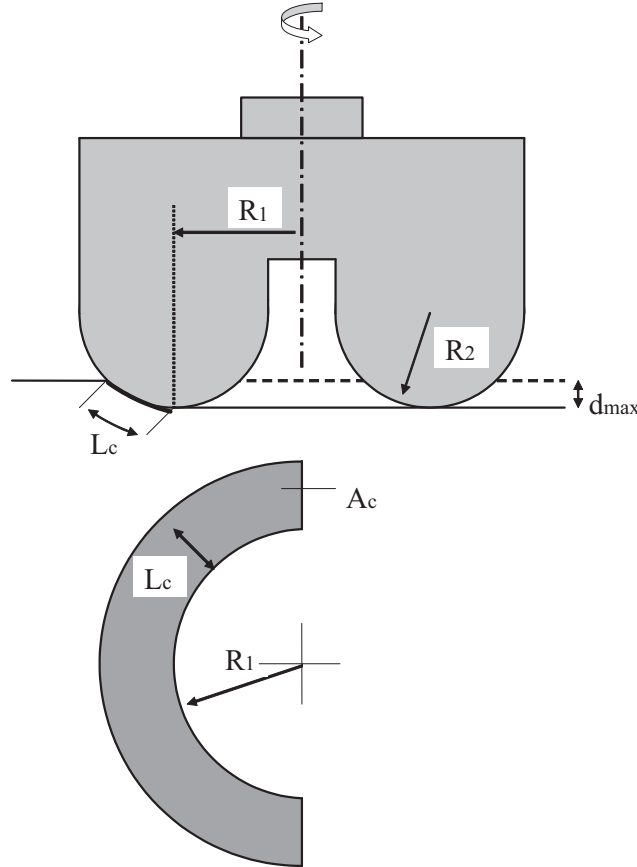


Figure 3.10: Maximum contact area A_c

Chapter 4

Machine concepts and layouts

4.1 Introduction

In this chapter different machine concepts and layouts are given. These will describe the basic form of the grinder. Also the measurement system concept is described. In the next chapter, chapter 5, the concepts of the machine parts are given.

4.2 Unstacked machine concept

The tool should be able to move relatively to the workpiece in radial direction (x), axial direction (y) and should be able to rotate in Rz-direction. This way free-form lenses can be produced when also the workpiece is rotated. The movement in x-direction is slow and with a constant speed. The movement in y-direction is the fast movement and is used to grind free-form features. Movement in this direction should be relatively fast, because a free-form feature passes the tool every rotation of the workpiece. The y-position of the tool relative to the workpiece is dependent on the rotational position of the workpiece. The rotation in Rz-direction is needed to orientate the tool axis nearly perpendicular to the workpiece surface. This gives a defined edge of the tool being used and reduces the influence of the tool runout.

When the tool is placed onto a bearing on a plane, all these degrees of freedom, DOF's, are unconstrained while the others are not. Figure 4.1 shows the tool on its airbearing and the unconstrained DOF's. The tool is floating on the plane of the paper. Those other DOF's are constrained almost directly to the fixed world, i.e. the plane. Compared to a stacked layout this allows a higher stiffness and limits the amount of errors caused by accumulated manufacturing tolerances. Because of this limited error it is not necessary to adjust the constrained DOF's during the machining process, there is no need to use additional actuators and guideways.

4.3 Machine layout

4.3.1 Introduction

This section will describe a number of different machine layouts. All the layouts use the unstacked machine concept from 4.2. The plane is provided by a block of granite. The advantages and disadvantages are examined and finally a choice for one of the layouts is made.

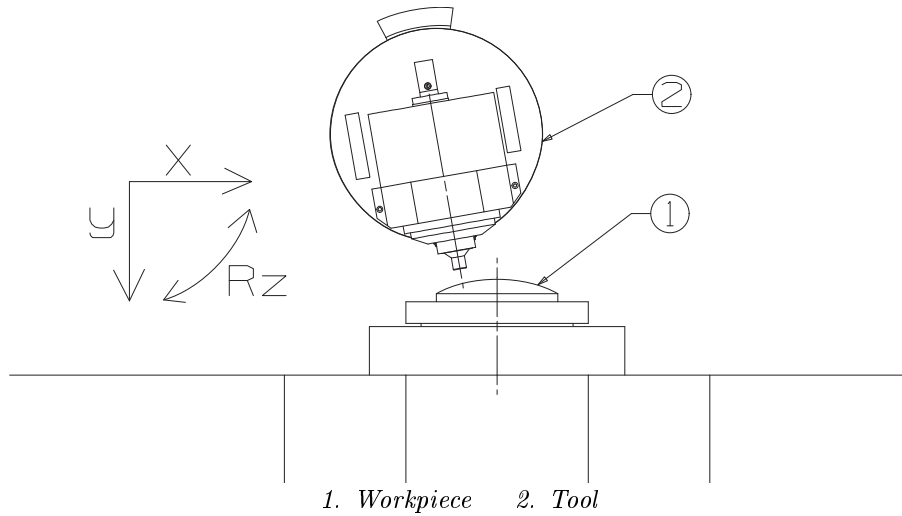


Figure 4.1: The tool spindle on a plane can move in X, Y and Rz direction

4.3.2 Layout 1, T-configurations

Layout 1a

This layout is a T-configuration that is also used on the Precitech Nanoform diamond turning machine. The tool can move in y-direction and can rotate in Rz-direction. The workpiece is able to move in the x-direction. The greatest advantage here is that the two translating guideways can basically be the same. The only differences are the direction in which they move, namely perpendicular to each other, and perhaps the dimensions of the guideway because the workpiece spindle is much heavier than the tool spindle. The movement of this heavy workpiece spindle however is its major disadvantage. The weight of such a spindle is about 150 kg and all of this mass plus the mass of the guideway itself has to be carried by the guideway bearings. Connecting this spindle to the fixed world will improve the machines dynamic behavior and working speed.

Layout 1b

Here the x-slide holds the tool, which can rotate in Rz inside the x-slide. The workpiece spindle can translate in y-direction. This layout offers the same advantages as the T-configuration of layout 1a, but here the heavy spindle must be moved fast in the y-direction. This requires a lot of power and a very good controller.

4.3.3 Layout 2, fixed workpiece spindle, large y-slide

In this layout the workpiece spindle is directly attached to the fixed world. By only moving the light tool spindle, the dynamical behavior of the grinder is improved. This results in a faster machine which uses less power. The y-slide holds the x-slide. This will result in a large machine because the x-translation is about three times larger than the y-translation. When moving in the fast y-direction a great amount of mass is moving, so this concept is not suited for a good dynamical performance.

4.3.4 Layout 3, fixed workpiece spindle, small y-slide

Layout 3a

This concept also has got a fixed workpiece spindle. The x-slide holds the y-slide. The tool spindle can rotate inside the y-slide. When translating in x-direction the biggest mass is moved. This is favourable

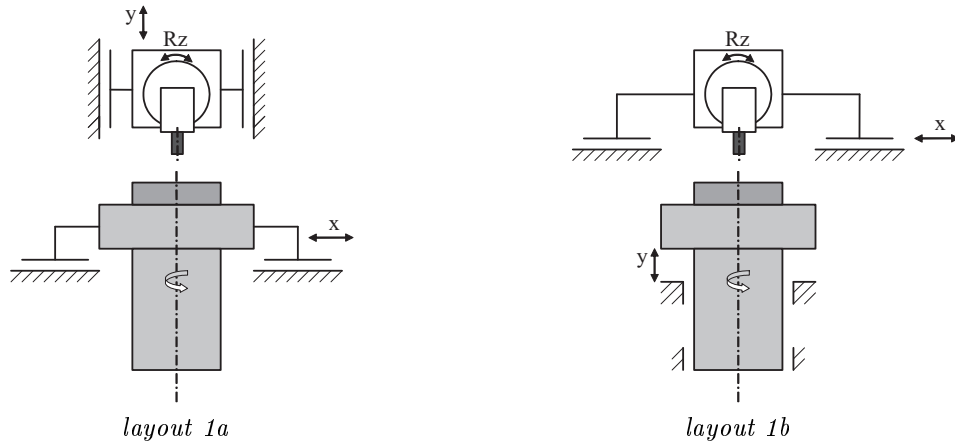


Figure 4.2: layout 1, T-configurations

because this is the slowest moving translation, moving radially across the workpiece surface in minutes. The mass moved by the y-slide is far less than that of the x-slide, so non-rationally symmetric features can be ground fast with these features passing every rotation of the workpiece. A feature passes the tool every few seconds.

Layout 3b

This concept also has the workpiece spindle directly connected to the fixed world. But now the y-slide is placed inside the rotating part, rotating in R_y . The main advantage here is that the centre of rotation of the tool can be put exactly onto the workpiece surface. This means a rotation of the tool will not lead to any translation. This shortens the strokes in x- and y-directions. However when the centre of rotation is on the workpiece surface, the rotating part can only be quarter of a circle. Else it would hit the workpiece at a given angle of the tool. Because the rotating part can only be quarter of a circle, a stiff bearing connection in the direction lateral to the tool axis is very difficult.

4.3.5 Orientation of the machine layout

For each of the given layouts the choice can be made whether the plane on which the tool moves, as described in 4.2, is horizontal or vertical and if the workpiece spindle axis should be orientated horizontally or vertically. The vertical plane and vertical workpiece axis of figure 4.5(a) prevents the weight of the workpiece bending the workpiece spindle radially. It also features a good accessibility for loading and unloading workpieces. Weight compensation for the tool spindle and the y-slide are necessary to reduce required motor capacity. Else the motor has to generate a continuous force, which will lead to a lot of dissipated power causing the grinder to heat up. Tool weight compensation is dependent on the angle of the tool disk, because the centre of mass of the tool spindle and disk is not in the disk centre. A vertical plane also puts the machine's centre of mass up high, so environment isolators should be placed carefully to have a stable isolating system.

Figure 4.5(b) also shows a vertical plane on which the tool spindle moves, but features a horizontally oriented workpiece spindle. Weight compensation as described for the previous orientation is still needed. The centre of mass is still very high. Chips and grinding fluid are easily removed from the workpiece, even from concave ones.

Figure 4.5(c) features a horizontal plane, which brings down the centre of mass significantly. This decreases the space needed for a stable isolator platform. It is safe to preload the x-slide bearings with

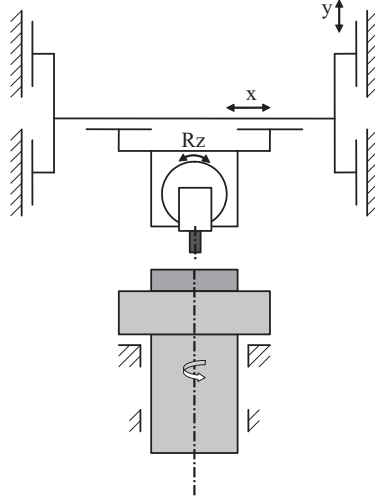


Figure 4.3: Layout 2, fixed workpiece spindle and large y-slide

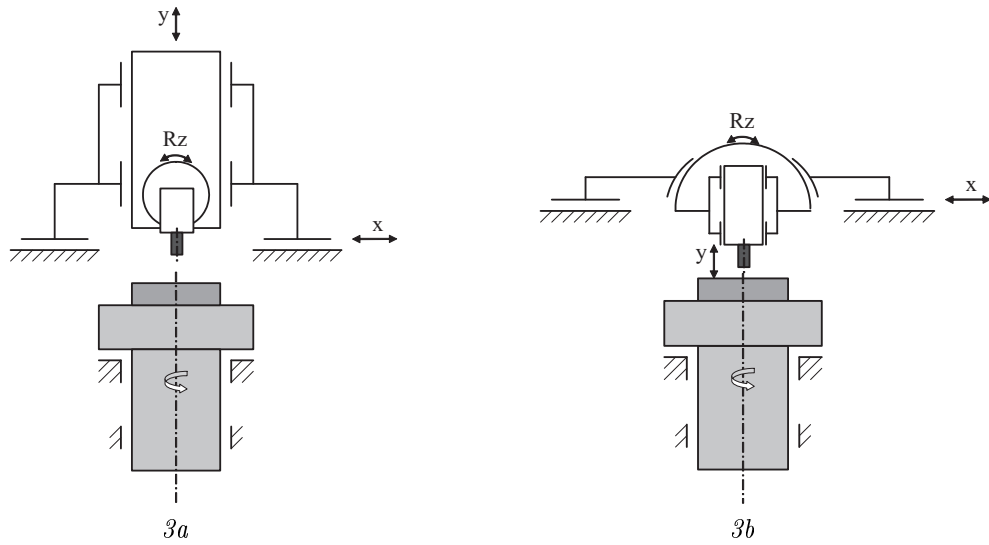


Figure 4.4: Layout 3, fixed workpiece spindle and small y-slide

underpressure. In case the underpressure is disturbed or lost, the frame stays on the granite table. The vertical orientations will need brackets to prevent the frame falling to the ground and destroying the machine. The horizontally orientated workpiece axis allows easy chip removal.

4.4 Measurement loop

In order to get products with a good shape accuracy it is important to know the position of the tool tip relative to the workpiece. Ideally the position of the tool tip itself is measured and compared to a reference on the workpiece. However this is not possible, because the tool tip is covered in grinding fluid and often is inside the workpiece. A measurement loop as shown in figure 4.6 is designed. The workpiece spindle is mounted in the vertical granite slab. Following the measurement loop, the planar position sensor is shown at (1). This sensor is directed at a grid at the bottom of the y-slide.

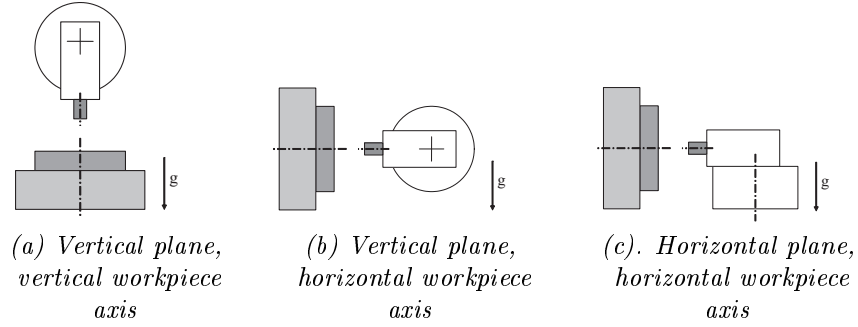


Figure 4.5: Three different machine orientations

The measurement loop continues through the y-slide, crosses the radial tool disk airbearing and goes through part of the tool spindle housing to (2). This is the position of the inductive sensors directed at a flange on the rotor, very close to the tool.

The planar position sensor (1) is used for the slide-actuators to bring the tool spindle to the desired nominal position. The inductive sensors (2), measuring the position of the tool relative to the tool spindle housing, are used for the controlled-force controller. They are also used to measure the difference between the nominal axial position of the tool inside the tool spindle housing and the real position as a result of the force applied by the workpiece on the tool. This difference can be corrected for during the next grinding pass by adding the difference to the setpoint of the slides.

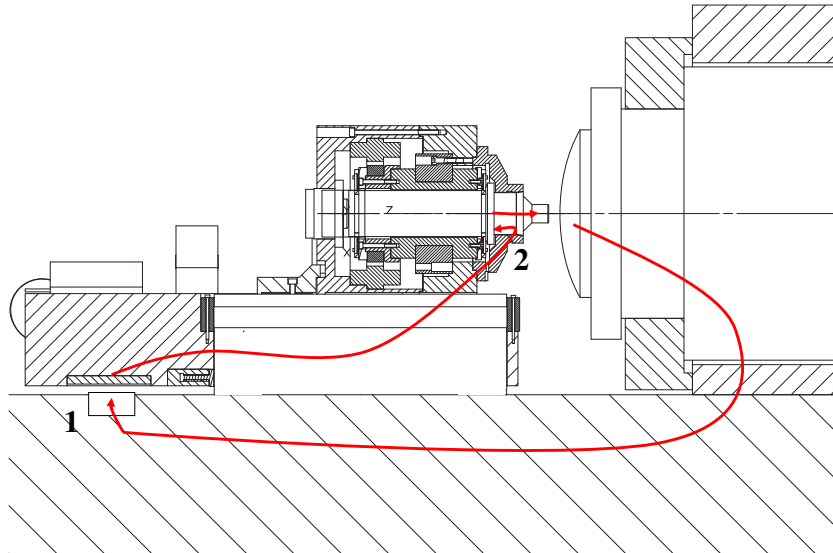


Figure 4.6: Position measurement loop

4.5 Conclusion

After evaluating the different layouts, layout 3(a) with orientation (c) is chosen as the best alternative. It gives a low amount of moving mass and a low centre of mass. The layout is robust, even in case the underpressure preloading the x-slide airbearings fails. In order to load and unload the workpiece a support has to be designed to aid the operator. Figure 4.7 shows the way the machine is loaded. Notice that the operator support frame is not designed yet, i.e. the operator is 'floating'. An operator support frame is needed first of all to make sure the operator can load and unload the machine in a proper way, without suffering from back injuries. The support frame should also envelope the entire machine so people cannot lean directly onto the granite slab and doing so tilting the machine on its isolators.

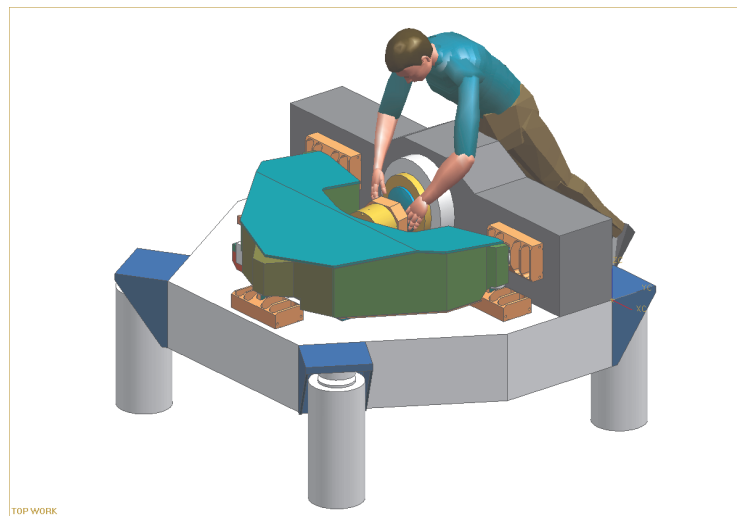


Figure 4.7: 'Floating' operator loading workpiece

Chapter 5

Tool spindle concepts

5.1 Introduction

This chapter describes the concepts that are examined in order to get the final tool spindle design. Two concepts, one with an elastic guideway and one with an aerostatic guideway are compared. Further the position of the tool has to be measured and the way this is done is described in section 5.6. Finally the seal concept is explained. This non-contact seal must prevent the grinding fluid, containing abrasive grains and glass chips, from flowing inside the tool spindle.

5.2 Controlled-force grinding spindle

In order to apply a constant force onto the workpiece the machine loop between workpiece and tool should have very low stiffness. A change in position of the workpiece relative to the tool caused by vibrations or other machine errors may not lead to a change in grinding force. Also the tool mass should be as low as possible to prevent that inertial forces can cause subsurface damage. The workpiece must be able to push away the tool tip with a limited amount of force. So the low stiffness connection of the tool should be as close as possible to the tool tip. The stiffness of this connection can be increased when grinding in position-controlled mode. This way a good shape accuracy can be achieved, while monitoring the grinding force. The rest of the machine has got high stiffness for a good dynamical behavior and a good position accuracy during position-controlled grinding.

To minimize the moving mass the choice was made to make the axial bearing stiffness of the grinding spindle controllable. Because when precision grinding the normal grinding force is about ten times higher than the tangential, cutting force, this concept results in very little deformation, compared to a radially loaded grinding wheel. The spindle of such a wheel is bent instead of compressed and this will generally cause more deflection. The wheel chosen for the controllable axial stiffness concept is a cupwheel of 20 mm in diameter. This wheel is pressed onto the workpiece axially and can be used to grind small non-rotational symmetric features.

In the following subsections two concepts are discussed that are able to control the axial stiffness of tool spindle.

5.3 Concept 1, using an elastic guideway

For this concept the tool tip is connected to a drive, which basically is a tube or rod. This drive is suspended by two membranes on both sides of the drive, allowing it to translate in axial direction, see figure 5.3. This way an elastic guideway is created. A stroke of 10 μm is sufficient, because the drive only has to correct for the machines position error. A small depth of cut is programmed into

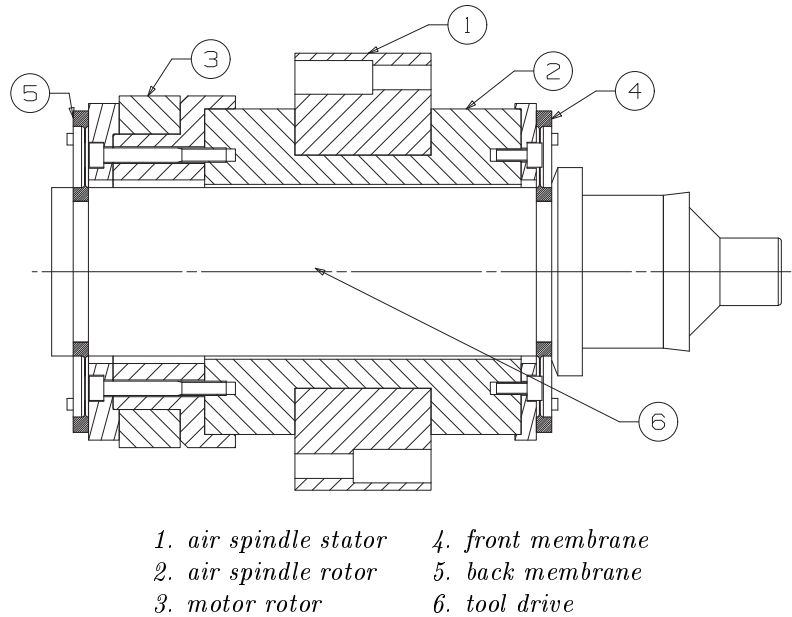


Figure 5.1: Concept 1, using membranes as elastic guideway

the machine and the spindle is moved to the right position within the machine position error. Using the membrane concept with a small axial translation results in a stiff construction, because the membranes are very stiff in radial direction when they are in their nominal position. The drive is mounted into a hollow rotor, to which a motor is connected. To actuate the drive a voice coil is placed at the back of the drive with the magnet on the rotating part, for obvious reasons. Because there is no physical contact between the coil and the magnet of a voice coil there is no stiffness, which makes a voice coil an excellent choice as drive actuator.

The main advantage of this concept is that the axial force of the motor rotor, does not interfere with the grinding force. It was shown in [Halo4] that a direct drive motor not only produces a torque to rotate the spindle, it also produces an axial force. This force has a one-cycle component which amplitude is independent of the applied current. The number of cycles of another force depends on the number of magnets used on the rotor. For example a rotor with 12 magnets will give a 12 cycle-force which is depended on the applied current. An increase in current will increase the disturbing axial more-cycle force. The Airex motor studied by [Halo4] had a one-cycle force of about 1 N, although it is assumed this value is too high. The more-cycle amplitude is about 0.15 N at 1 A and reaches to 0.5 N at 3 A. Compared to a maximum grinding force of 1 N, these values are very large. By using the membrane concept these forces do not disturb the grinding process. The bearings of the air spindle deal with these forces. The hollow rotor requires a large diameter which result in a lower maximum speed, of about 7000 rpm. Spindles for higher speeds generally have slimmer rotors.

5.4 Concept 2, using an aerostatic guideway

The second concept holds the tool drive directly inside the air bearing stator, see figure 5.2. This stator consists of two radial ring bearings, which constrain all but the axial movement of the drive and the rotation along its axis. The motor rotor is connected directly to the tool drive. This concept is relatively easily made, few components need to be aligned.

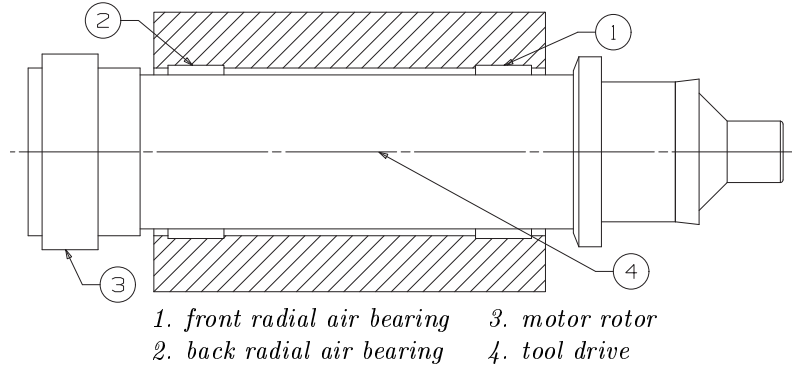


Figure 5.2: Concept 2, using an aerostatic guideway

5.5 Comparing spindle concepts

When comparing the two concepts, the second concept looks simpler. It consists of a few, robust parts, so during assembly there is little to align to get a small runout. This concept can also have more radial stiffness, because of the absence of the membrane compliance. A survey for spindles with a rotor diameter of about 50 mm and two radial air bearings, showed that a radial stiffness of $10^8 N/m$ can be expected, (www.seagullsolutions.net). These are high speed spindles with speeds up to 20.000 rpm. However such high speeds require a fast controller for the axial actuator, because of the runout of the tool. Every cycle the tool drive is excited by the tool-workpiece contact and the frequency of this excitation increases with increasing tool speed. The controller for the axial actuator must be able to follow this excitation. The first concept has got lower moving mass, because the motor rotor is not translating. The high density, $7400 kg/m^3$, magnets add significantly to the mass of the tool drive. Also as described earlier concept 1 removes the influence of force disturbances caused by the motor on the grinding process. Because the grinding process is very delicate, motor disturbances are expected to be a great problem if not properly dealt with. Table 5.1 summarizes the differences between the two concepts. After evaluating the properties of both spindle concepts, the concept with the elastic guideway seems most promising and is used in the final design.

Concept 1, elastic guideway	Concept2, aerostatic guideway
low translating mass (1.6 kg)	higher translating mass (4 kg)
insensitive to axial motor forces	axial motor forces need to be compensated
alignment of tool drive and spindle rotor	easier alignment
less radial stiffness due to membranes, $10^7 N/m$	higher radial stiffness, $10^8 N/m$
maximum speed 7000 rpm	maximum speed > 7000 rpm

Table 5.1: Comparing the concepts

5.6 Tool drive measurement

In order to control the position of the tool drive a measurement system is required. Because of planned experiments on an already existing platform, on which the tool spindle will be mounted, the choice is made to measure the position of the tool drive relative to the tool holder. Because the tool drive is rotating at a high speed there should be no physical contact between the tool drive and the measurement probe to avoid wear. The position should be measured as close to the tool tip as possible to reduce the influence of thermal expansion. However it is not possible to measure the tool tip directly, because most of the time it is inside the workpiece covered with grinding fluid. A flange is made

near the front of the tool drive, to minimize the influence of thermal expansion. Because of the harsh environment created by the grinding fluid, it is not excluded that some of the fluid comes into contact with the measurement flange. So capacitive sensors are not suited, because they are very sensitive for contamination, unless a perfect seal is designed. Because a non-contact seal is required, see 5.7, this will be very difficult.

Two inductive sensors are chosen as measurement sensors and are placed diametrically on the flange. This way the wobble of the flange can be corrected for and this allows a large manufacturing tolerance. An inductive sensor basically is a coil to which a high frequency (MHz) alternating current is applied. With this current the coil produces an alternating magnetic field. This field will induce Eddy-Currents in the nearby electrically conductive target. These Eddy-Currents increase if the distance between the target and the coil decreases. The Eddy-Currents also change the impedance of the coil and this way the voltage over the coil. This voltage is a measurement for the distance. To correct for temperature changes a second coil, the balance coil, is added. Because Eddy-Currents exists at some depth inside the material, 0.01 - 0.1 mm, the homogeneity of the material determines if there is an electrical runout. Because the tool drive is rotated relative to the sensor, the sensor is continuously measuring different parts of the flange. Differences in composition, hardness, permeability and electrical conduction will cause electrical runout, adding to the uncertainty of the measurement. Using an aluminum flange reduces the influence of electrical runout significantly, because of its homogeneous structure. If the measured flange rotates too fast, the inductive measurement system cannot take enough samples per unit of surface to achieve a reliable result. These systems need at least 50 oscillator cycles per coil diameter. This means when rotating the 70 mm diameter flange at 7000 rpm and using a 3 mm diameter probe, the oscillator frequency should be at least 420 kHz. The required resolution should be smaller than about 1/4 or 1/5 of the desired accuracy of 0.2 μm .

The chosen system, made by Lion Precision, has got a resolution of 0.04 μm at 10 kHz sample frequency. Its range of 0.50 mm is large enough for the application. The oscillator frequency of 1 MHz is high enough for the fast moving rotor. More information about this system can be found in I. The probes are equipped with thread for mounting purposes. By placing them into a threaded hole the axial position inside the measurement frame can be adjusted. A nut is then placed to lock this position. The measurement frame is connected to the tool holder. An offer invited at IBS Precision Engineering, Eindhoven showed that the total price of two inductive sensors and their drivers is just below 3000 euro.

5.7 Sealing

To protect the inside of the tool spindle from the grinding fluid containing sharp glass and abrasive particles, a seal is applied. To avoid friction influencing the translation of the tool drive, a non-contact seal is used. This seal works mostly because of the rotating spindle centrifuging the fluid away from the centreline, see figure 5.3. Most of the fluid is diverted by the edges of the rotor and the stator. Some fluid will pass through the narrow chamfered clearing. The clearing is about 0.1 mm high and about 10 mm long. Fluid on the conic surface of the rotor will be centrifuged outwards and when it stays into contact with the rotor it will be moved to the right of figure 5.3. The conic surface functions as a pump, using fluid to block incoming fluid and pushing the fluid outside the seal. The fluid that passes the conic surface is mostly collected in a groove. This way the amount of fluid that reaches the inside of the tool spindle is minimized.

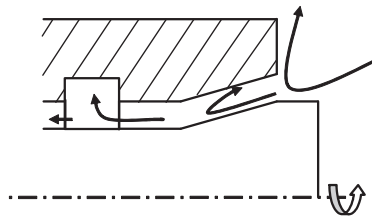


Figure 5.3: Fluid flow into tool seal

Chapter 6

Machine design

6.1 Introduction

In this chapter the design of the grinder is discussed using the concepts described in chapters 4 and 5. First an overview of the entire grinder is given. Then the grinder is divided into subassemblies and each of the subassemblies is discussed, first by giving an overview of the subassembly and then the components are described. The first subassembly described is the tool drive, because this is one of the most important features of this machine.

6.2 Machine design overview

Figure 6.1(a) shows the base assembly, consisting of a horizontal granite slab with perpendicular to it the vertical granite slab. The base assembly is placed on isolators. Figure 6.1(b) shows the tool spindle on the horizontal granite slab. The disk on which the tool spindle stands can move along the horizontal surface, because the bottom of the disk is suspended with an airbearing. In figure 6.1(c) the y-slide is added. This slide suspends the tool spindle disk in radial direction, and it can move in y-direction, parallel to the workpiece axis. The y-slide is suspended to the x-slide, because this allowed the y-slide airbearings to be preloaded in a proper way. This means that the y-slide is 'floating' above the granite slab. In figure 6.1(d) the x-slide is added and this completes the grinder. The x-slide is suspended by three airbearings on the horizontal slab and by two airbearings on the vertical slab. The x-slide can move in x-direction, radial across the workpiece.

6.3 Tool drive

6.3.1 Tool drive assembly

The front (2) and back membrane (1) are centered respectively with the front (4) and back plug (9), see figure 6.2. The two plugs are centered on the tube (3) and preloaded by the M8x130 bolt. The tool connector (7) is placed into the front plug. The tool itself (5) can then be placed onto the front plug and is preloaded with the M6x40 bolt (6). This bolt can easily be removed so the tool can be changed. At the back plug, the magnet for the voice coil (10) is glued onto its designated place. Each membrane is connected to the spindle rotor with 6 M2x12 bolts (8). Figure 6.2 also shows the edge (12) on the flange on the front plug that will be used for the position measurement of the tool drive.

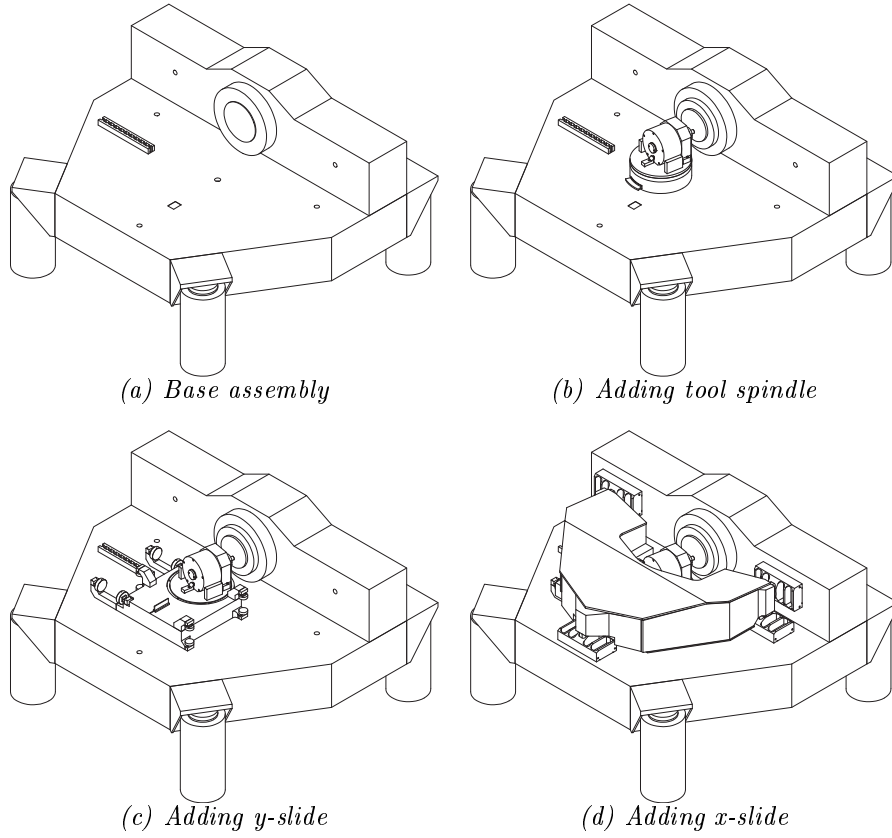


Figure 6.1: Machine design overview

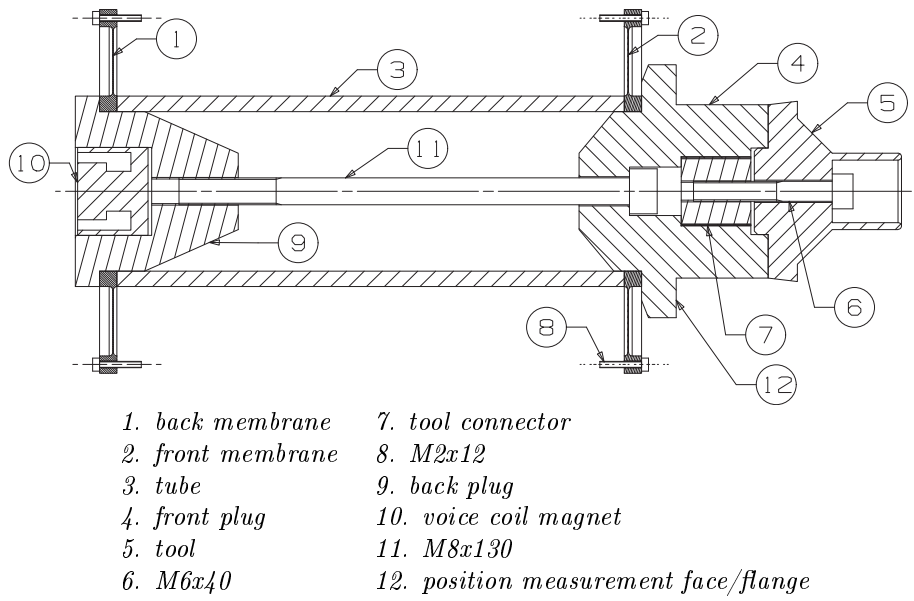


Figure 6.2: Assembled tool drive

6.3.2 Tool drive components

Membranes

The membrane consists of two concentric 5 mm thick rings connected with a 0.25 mm thick sheet. The two rings are used for clamping this component to either the tool drive or spindle rotor. Because these rings are so much thicker than the sheet, when the membrane is being used and is translating, there will be no strain at the clamping zones. This prevents hysteresis, because there is no micro-slip at the clamping zone. The membranes are made from steel, because the high E-modulus, compared to for example aluminium, allows the use of a very thin sheet having enough radial stiffness. This thin sheet has a low axial stiffness so a very good ratio between a high radial stiffness and a low axial stiffness can be achieved.

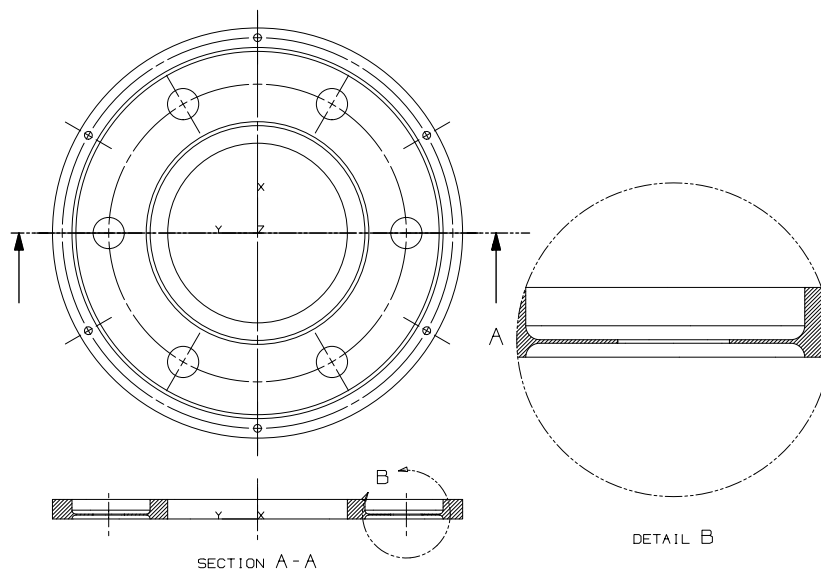


Figure 6.3: Membrane

Front plug

The front plug is used for centering the front membrane. The flange is used as a target for the position sensors. The top of figure 6.4(a) shows the tool interface with a centering bore and a plane perpendicular to the centre line, so the tool can be connected properly. Also the thread is shown that is used to connect the tool connector. The front plug is made from aluminium because of the position sensors used. A steel plug would have caused interference as described in section 5.6. Because of the regular tool changes, connecting the tool bolt directly in aluminium thread would have caused problems. The steel bolt will cut away some of the soft aluminium with each tool change, ultimately destroying the plug's thread. Therefore an insert, the tool connector, is needed.

Tool connector

This 20 mm diameter steel insert has thread on the outside and is to be placed into the front plug. When placing the tool connector, some glue may be applied, to make sure it is not loosened during a tool change. The inside hole has thread for the tool bolt (M6x40). A slot on top allows the connector to be handled with a screwdriver.

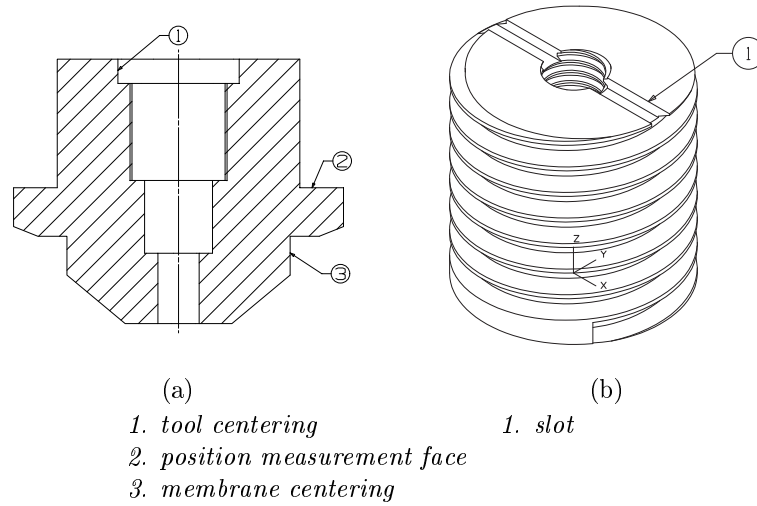


Figure 6.4: Front plug (a), tool connector (b)

Tool

A survey of commercially available tools did not result in the findings of a suited tool. The tools found had large and heavy steel cones as part of their machine interface. Because the weight of the tool is a major issue for the grinder, a custom tool is designed, see figure 6.5. The tool is centered on the front plug with a centre edge. Tilting is prevented by the large diameter of the tool interface. The outer side is chamfered as part of a seal, preventing the grinding fluid to reach the inside of the spindle. The concept is described in section 5.7. Like other cup wheels, this tool has got rounded edges.

Tube

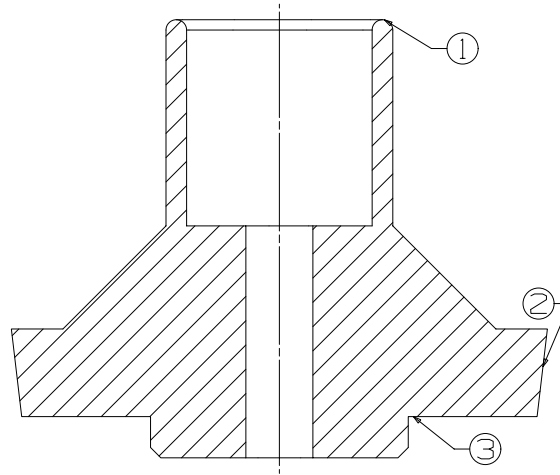
The base of the tool drive is the tube, connecting the two membranes and the two plugs. The outer diameter is 55 mm so it fits into the hollow air spindle rotor. Because of the limited outer diameter, a steel tube is chosen instead of an aluminium one. A thin walled steel tube weighs less than a thick walled aluminium one, when they have the same outer dimensions and bending stiffness. The length of the tube will be determined as described in 6.4.1.

Back plug

The back membrane is centered on the back plug. The same centering is used to place the back plug into the tube. Inside the plug there is room to place the voice coil magnet. There is also a threaded hole for the long bolt that preloads the two plugs onto the tube. This hole can also be used to press the magnet out of the plug in case of revision.

Voice coil magnet

The voice coil magnet goes in the fit in the back plug and is glued. If necessary the magnet can be removed using a bolt pressing the magnet out. The datasheet of the voice coil can be found in I.



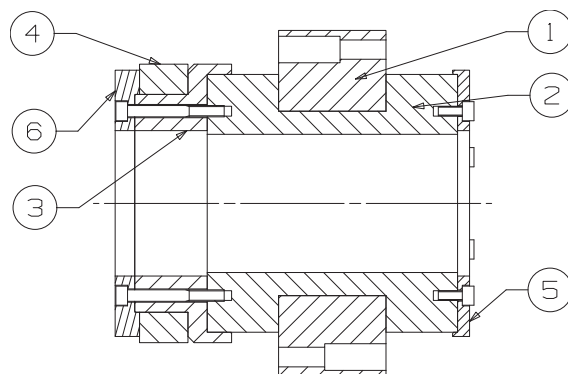
- | | |
|-----------------|--------------|
| 1. rounded edge | 3. interface |
| 2. seal | |

Figure 6.5: Tool

6.4 Tool spindle

6.4.1 Spindle assembly

In figures 6.6 - 6.9 the different assembly steps of the tool spindle are given. Figure 6.6 shows the stator (1) and the hollow rotor (2) of the Blockhead air spindle. The datasheet of this spindle can be found in appendix I. To the front of the rotor the front membrane coupling (5) is mounted. To the back of the rotor the magnet carrier (3) with the magnets (4) and the back membrane coupling (6) are connected. The back membrane coupling is clamped to the magnet carrier with the same bolts that clamp the magnet carrier to the rotor.



- | | |
|-----------------------|----------------------------|
| 1. air spindle stator | 4. motor magnets |
| 2. air spindle rotor | 5. front membrane coupling |
| 3. magnet carrier | 6. back membrane coupling |

Figure 6.6: Assembling the rotor

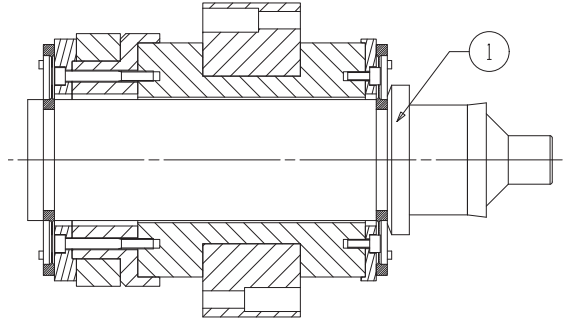


Figure 6.7: Adding the tool drive assembly (1)

In figure 6.7 the tool drive assembly, as described in section 6.3 is added. The alignment of the tool drive assembly and the rotor can be adjusted, so the tool will have minimum runout. The possibility to adjust the alignment here allows the tolerances of the parts that are centered, to be much larger. In this figure one can also see the bolts, that hold the membrane coupling. They can be reached when the membrane is in place. If the tool spindle is (partly) disassembled, the delicate membranes are protected by the membrane couplings.

To have the membranes function properly, it is crucial that the inner and outer rings of the membrane are in the same plane. Any axial misalignment between the two rings will cause the axial stiffness to increase slightly. The radial stiffness is rapidly increased, so the ratio between the radial and axial stiffness deteriorates quickly. In order to get a good working membrane, the difference between the axial positions of the two rings should not exceed 0.01 mm. This will give the membrane a $c_{ax} = 5.3 \cdot 10^3 N/m$ and a $c_{rad} = 9.1 \cdot 10^6 N/m$. There are two ways to reach this narrow axial alignment. The first one is to specify the sizes of the rotor components with very narrow tolerances. This will make the tool drive tube, the membranes, the membrane couplings and the magnet carrier very critical components. Also the height of the air spindle should be measured, because the manufacturer specifies a large height variation.

The other way is to partly assemble the rotor, as far as shown in figure 6.6. Then the distance between the outer surfaces of the two membrane couplings can be measured. So all thickness variations of the assembled parts are taken into account. Knowing this distance, the tool drive tube can be made to the right length with a tight tolerance. The exact thickness of the membranes, the membrane couplings and the magnet carrier are not important, it is important however that these parts have a good flatness.

Now the entire spindle with the tool drive assembly is placed into the toolholder front, see figure 6.8. The air spindle stator has holes for bolts to mount it onto the toolholder front. The exact position of the spindle inside the toolholder is not important, because the complete tool spindle unit will be aligned with the workpiece spindle later on.

The toolholder is closed by placing the back part onto the front part, see figure 6.9. The toolholder back holds the coil assembly for the actuation of the tool drive assembly and it also houses the motor stator. Finally the measurement frame is placed onto the toolholder front. This measurement frame contains the two position sensors that measure the position of the tool drive assembly.

6.4.2 Tool spindle components

Blockhead 4R2.25 air spindle

This air spindle built by Professional Instruments has a very low runout of 50 nm. It has got high axial and radial stiffness, $c_{ax} = 175 \cdot 10^6 N/m$ and $c_{rad} = 140 \cdot 10^6 N/m$, and can be operated at a

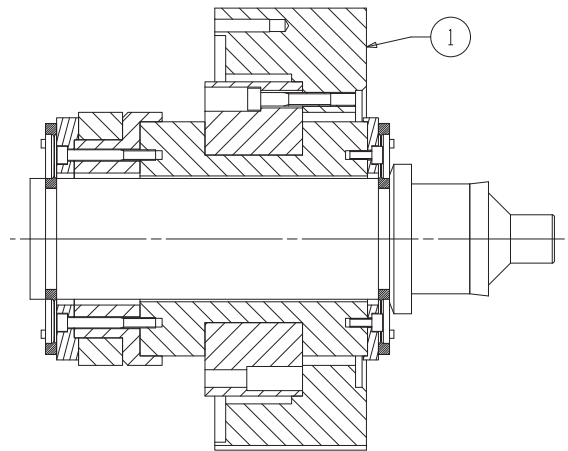
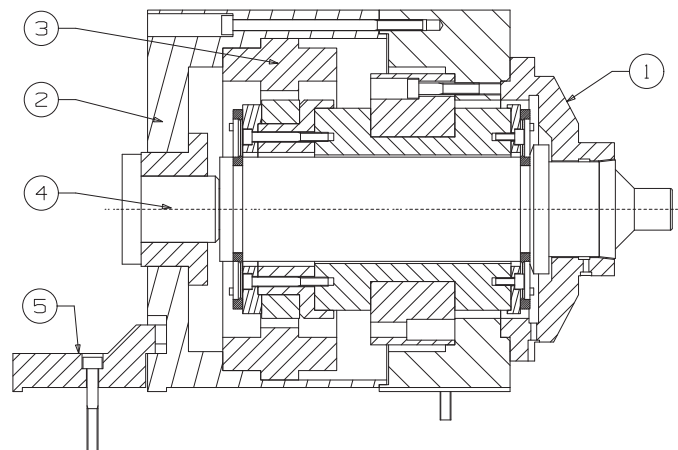


Figure 6.8: Adding spindle to toolholder front (1)



- | | |
|----------------------|------------------|
| 1. measurement frame | 4. coil assembly |
| 2. toolholder back | 5. clamp |
| 3. motor stator | |

Figure 6.9: Completing the tool spindle unit

maximum speed of 7000 rpm. More importantly it features a hollow rotor with an inner diameter of about 60 mm (2.25 inch). This allows the tool drive assembly to be placed. The Blockhead spindle has got one radial bearing and a ring shaped axial bearing. This axial bearing prevents the rotor from tilting. Spindles made for higher speeds usually have two radial and one axial bearing. Tilting of the rotor is prevented by the two radial bearings. However the spindles constructed this way do not have enough room for the tool drive assembly, due to their limited rotor diameter. Also high speed spindles have less radial stiffness than the Blockhead spindle, even though they have two radial bearings. This is because of the smaller diameter of the rotor, the airbearing surfaces are also small. Because this grinder is designed primarily for research goals, achieving high speeds and thus a high production rate is not a priority.

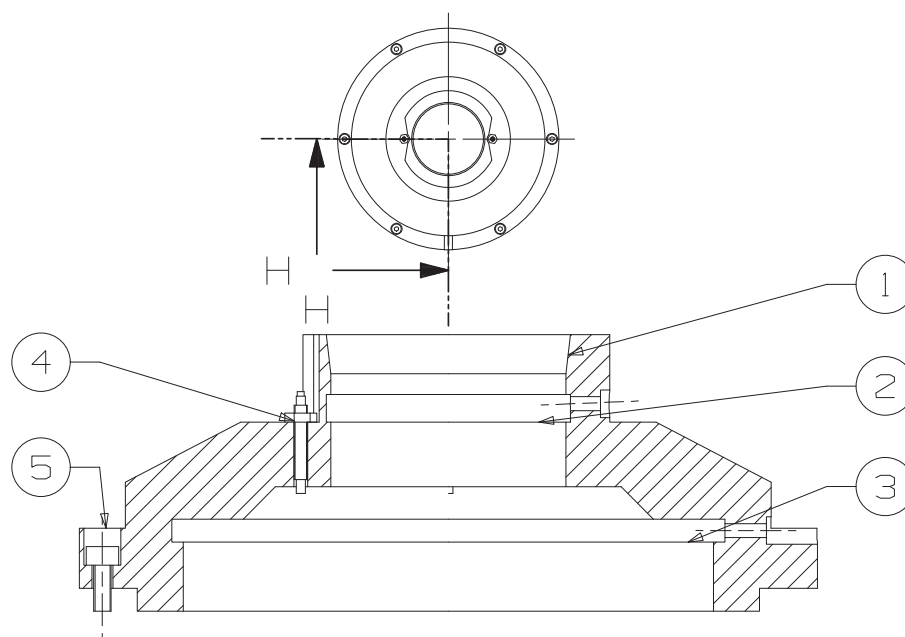
Membrane couplings

The membrane couplings are needed to enlarge the diameter of the membranes. To get a high ratio between the c_{rad} and the c_{ax} either the membrane should be large or it should be thin. Because it is difficult to manufacture a very thin membrane with the necessary thick outer and inner ring, the membrane should be large. The membrane coupling provides an interface for the outer membrane ring, the coupling itself is bolted to the mounting holes on the rotor.

Measurement frame

The measurement frame has got two functions. The main function is to provide a mounting interface for the inductive sensors looking at the tool drive. The two probes are placed diametrically so the wobble of the measurement flange on the tool drive can be acquired. The probes are mounted into threaded holes and a nut on each probe is used to lock the position of the probe, when the correct distance between the probe and the measurement flange has been set.

The second function is to shield the measurement flange of the tool drive and the air spindle from contamination, like grinding fluid. Therefore the edge of the measurement frame is chamfered to act as a seal as described in section 5.7. The fluid that passes the seal is collected in the first groove and sent out of the frame through a drain. The little fluid that passes the first groove is collected in the second groove and it also flows out through a drain. The fluid that passes the first groove can contaminate the measurement flange. Although it is not much, it is important to choose a position measurement system that is insensitive for this kind of contamination.



SECTION H-H

- | | |
|-----------------------------|---------------------|
| 1. chamfered seal edge | 4. inductive sensor |
| 2. first groove with drain | 5. mounting hole |
| 3. second groove with drain | |

Figure 6.10: Measurement frame, section view enlarged

Coil assembly

The coil assembly consists of three elements, see figure 6.11. The coil (4) is connected to the coil holder (3). The coil holder can be placed when the rest of the tool spindle unit is already assembled. In case of a coil failure, only the coil holder has to be disassembled. The coil holder fits into the coil holder base (2). This way the coil holder can be bolted to the holder base and the shape of the left side of the toolholder back (1) is not important. The inside part of the toolholder back can be machined by turning from the front side. The bottom of the inside of the toolholder back will be perpendicular to the axis of rotation with a very tight tolerance. The axis of rotation of the relatively short holder base is aligned by its wide flange. Finally the coil holder is placed inside the holder base. The coil holder also functions as an end stop for the tool drive. This way high stresses on the membranes are prevented, if a large axial force is pushing on the tool. The axial position of the coil holder can be adjusted by using a spacer, placed between the coil holder and the holder base.

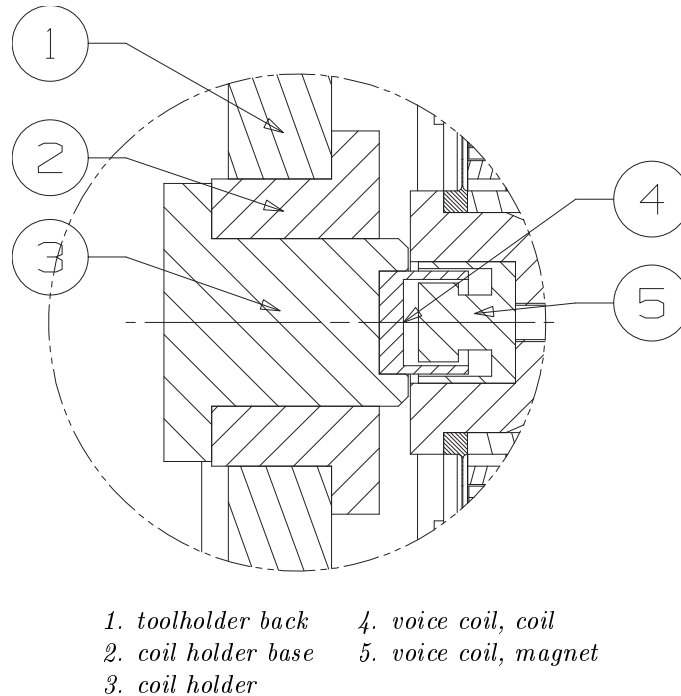


Figure 6.11: Coil assembly

6.4.3 Motor stator

The stator of the motor that rotates the tool consists of coils and iron. The exact shape of the stator needs to be determined but its size is comparable to other motor stators with the same power and speed. It is also necessary to build in three Hall-sensors with the stator. These sensors are needed to control the rotational speed of the rotor. Because only the speed has to be controlled, not the exact position, it is not necessary to use an expensive, high resolution encoder. The Hall-sensors should be sufficient.

6.4.4 Toolholder front

The outer shape of the toolholder front, shown in figure 6.12, is milled first. The mounting holes (4), (6) are also made. Then the toolholder front is placed in a lathe, so the fit for the air spindle (3) and the hole for the rotor (2) can be made. Also an edge is made to centre the toolholder back (7). This

way the toolholder front and back can be aligned, so the motor stator and the voice coil fit properly around the spindle rotor. At the front side the centre edge for the measurement frame (1) is machined.

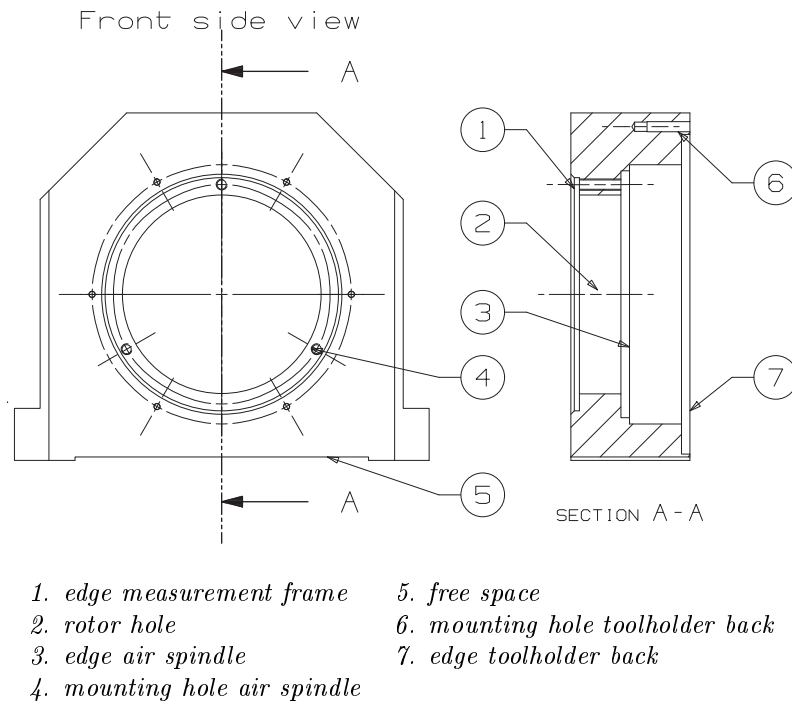


Figure 6.12: Toolholder front

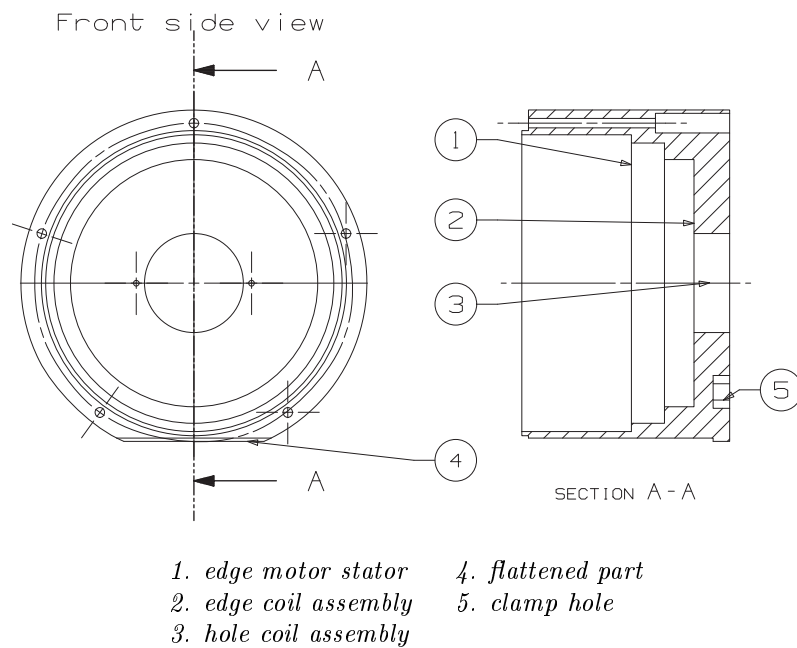


Figure 6.13: Toolholder back

6.4.5 Toolholder back

The toolholder back is made from bar stock. On a lathe the edge on which the motor stator is placed (1), is made. Then the edge (2) and the hole for the coil assembly (3) is made. On a milling machine the flattened part (4) is made. The flattened part features an elevated part, so only the back end of the toolholder comes into contact with the tool disk on which it is placed. Finally a clamping area (5) is milled, so the tool spindle can be mounted on the tool disk.

6.5 Tool disk

6.5.1 Tool disk assembly

Onto the disk base (4) the graphite parts of the radial (5) and axial bearing (6) are placed, see figure 6.14. Also the disk drive coils (2) are mounted to the side of the disk base. Inside the vacuum seal (7) is placed and it is pressed onto its place by the disk top (3). Beneath the vacuum seal is a room with underpressure, the vacuum chamber (8). This preloads the axial airbearing. The bottom of the vacuum chamber is sealed with a narrow gap surrounded with an atmospheric groove (9). Finally the tool spindle can be placed onto the three mounting holes (1). Two holes are at the front side of the tool spindle and one is at the rear.

6.5.2 Tool disk components

Vacuum chamber

To preload the tool disk, an airbearing placed at the opposite side of the horizontal granite slab can be used. However if the bearings are directly opposite to each other, a very large structure is needed, adding a large amount of - moving - mass. Reducing this mass by placing the preload bearing more to the edge of the granite slab, will induce bending of the slab, which is very disadvantageous. Therefore the choice is made to preload the tool disk using vacuum, [Ver99]. In this thesis 'vacuum' means a relative underpressure of maximal 0.6 bar (0.4 bar absolute). To limit the amount of air flowing through the vacuum chamber and thus limiting the required power for the pump, the vacuum chamber needs to be sealed. At the bottom of the disk, this requires a narrow gap that is long enough so a laminar flow goes through. A turbulent flow will induce unwanted disturbing forces on the disk. The perimeter of the vacuum chamber, w , is 0.93 m, the length of the seal (in radial direction), l , is 8.5 mm. The flow rate Q can be calculated using

$$Q = \frac{\Delta p}{R} = \frac{wh^3}{12\mu l} p_u \quad (6.1)$$

with μ is the dynamic viscosity of air, which is $17 \cdot 10^{-6} Pa \cdot s$, p_u the relative underpressure of 0.6 bar and h the gap height of $5 \mu m$. This gives a value of $Q = 1.64 \cdot 10^{-5} m^3/s$. Using the density of the air at the underpressure being $\rho_u = \rho_{atm}(1 - p_u/p_{atm})$ the Reynolds number, Re , can be calculated with

$$Re = \frac{Q \rho_u}{w \mu} \quad (6.2)$$

Using the parameters mentioned it can be shown that $Re = 0.54$ and because this is lower than the laminar-turbulent transition value of 2000, the flow is laminar. The vacuum seal at the bottom of the tool disk will work properly.

Because the disk base basically is a thick walled tube, the top of the centre hole needs to be sealed as well to create a vacuum chamber. This is done with a vacuum seal consisting of a thin sheet and a mounting ring. The ring is axially pressed onto an edge inside the disk base. Because of the underpressure beneath the vacuum seal the atmospheric pressure will try to push the seal downward. If instead of the seal a simple disk was used to seal the vacuum chamber, see figure 6.15(a), bending

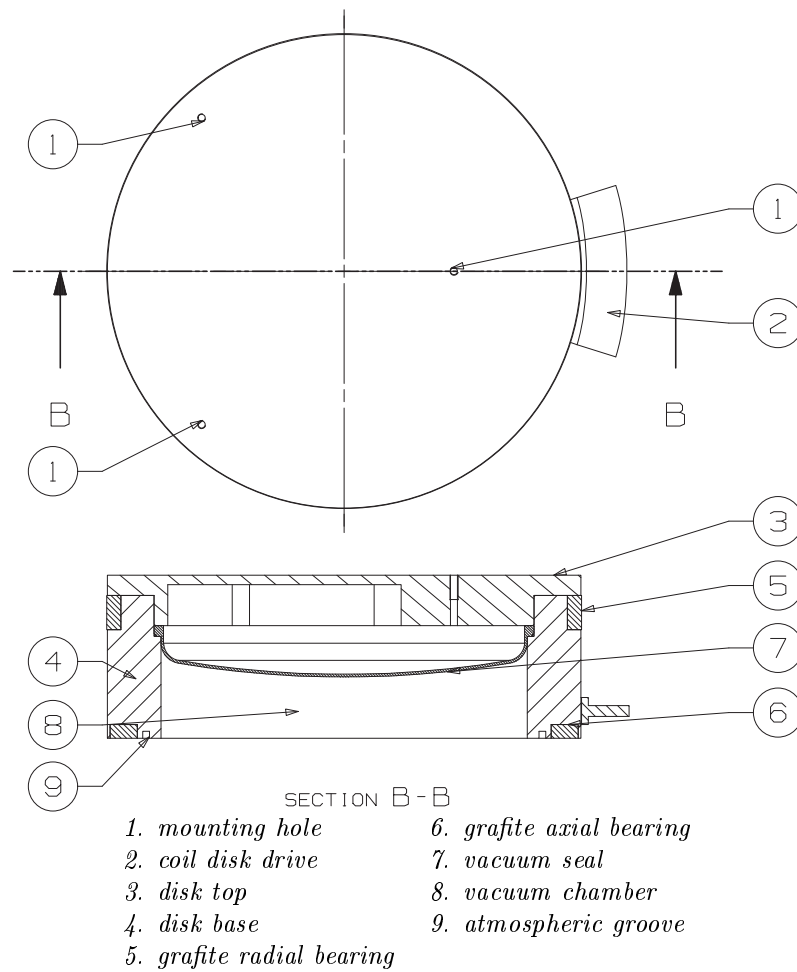


Figure 6.14: Tool disk assembly

of the disk by the atmospheric pressure would have caused the tool disk to deform radially. Also a lot of material is needed to reduce the bending stress to an acceptable level. Such an aluminium disk would weigh about 2 kg. Figure 6.15(b) shows a schematic view of the vacuum seal as used in the design. The thin sheet can resist forces only in its plane. Because the sheet is fixed in axial direction to the mounting ring, the force applied by the sheet onto the mounting ring, thus also on the tool disk, is in axial direction. The force generated by the atmospheric pressure will cause minimal radial deflection. This radial deflection would have caused the axial tool disk bearing to tilt relative to the granite base. Because the sheet is shaped almost like a sphere, stresses are low and a sheet of 2 mm thick aluminium is sufficient, see E.6. This is because there is only tension and no bending, so the material is optimally used. The weight of the vacuum seal is reduced to 0.5 kg.

6.6 Y-slide

6.6.1 Y-slide assembly

The base of the y-slide is an aluminium block to which airbearings are connected using cardan joints, see figure 6.16. A cardan joint reduces the tilt stiffness of the airbearing connection, allowing the airbearing to align parallel with the guideway. This way the mounting of the airbearing is less critical in order to avoid it getting jammed with the guideway. The gap between the airbearing and the guideway

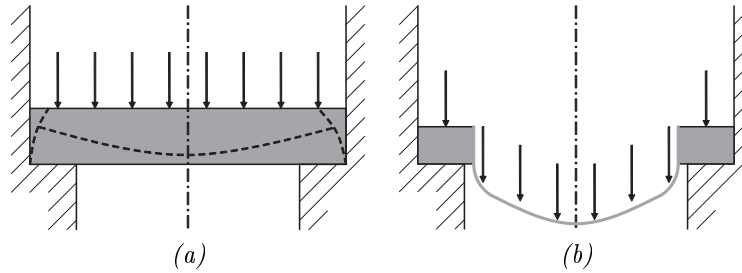


Figure 6.15: (a) Preloading causes radial displacement, (b) Radial displacement minimized

is about $5 \mu m$. The large airbearings (1) are preloaded with other large airbearings (2) that have a far less stiff connection. This way the preload bearings provide a constant force, instead of stiffness and this way an overconstrained situation is prevented. These large airbearings play an important role in the grinding process, because they play a part in the angle in Rz-direction and in the x-position. The small airbearings (3) however do not play a significant role in the grinding process, they just have to constrain the other DOF's of the y-slide. Their main task is to avoid low frequency vibrations of the y-slide and to prevent the y-slide from tilting so much that the airbearing ring, (5), runs into contact with the tool spindle disk. The small airbearings, (3), have a stiffness of $c = 5.2 \cdot 10^7 N/m$ each and with the total mass of the y-slide being 58 kg, the lowest eigenfrequency of the y-slide on its bearings is 261 Hz. The tool spindle disk will be radially suspended in the airbearing ring. This ring is made from steel to minimize its size and hereby minimizing the distance between the centre line of the disk and the workpiece. Also because this is a rotationally symmetric piece, it can be machined or ground into shape with the accuracy needed for a proper air gap. The bottom of the ring is bolted to the y-slide base. The strip of magnets for the tool spindle disk drive (6) is placed at the bottom of the base, this way the airbearing ring can be as close to the centre of mass of the tool spindle unit as possible, in z-direction. Finally the coils of the linear motor actuating the y-slide (7) are placed on the centre line of the base. This way no momentum is applied to the slide when it is being actuated, resulting in less tracking error. The coils are attached to the top of the base to minimize the distance between the line of the coil and the centre of mass of the y-slide and tool spindle unit.

6.6.2 Y-slide components

Measurement system

The position of the x- and y-slides are measured by a system connected to the y-slide, as described in section 4.4. A sensor on the horizontal granite slab determines the position of a grid at the bottom side of the y-slide. This way any x-frame errors in y-direction and any y-frame errors in x-direction are measured directly. This would not have been the case if each slide had its own separate scale.

The planar measurement system is the Nanogrid made by Optra, for a complete datasheet see I. The working principle is shown in figure 6.17. A laser beam is directed via a prism to the xy-grid. At the grid diffraction takes place and the $\pm 1^{st}$ order diffracted beam in both x and y direction is collected by the lens. The horizontal and vertical beams are then collected with a sensor and the fringe pattern is processed.

Because of the relatively large x- and y-stroke the standard solution made by Optra would have given an accuracy of $\pm 1 \mu m$. This way the desired accuracy can not be achieved. Communications with the people at Optra showed that there is a possibility to use their high accuracy, small sized grid with multiple sensor heads. When the grid is moved almost out of range of one sensor, it comes into range of another sensor. On certain x- and y-positions there are two or more sensorheads looking simultaneously at the grid. Such a system has an accuracy of $\pm 35 \text{ nm}$, sufficient for the grinder. The

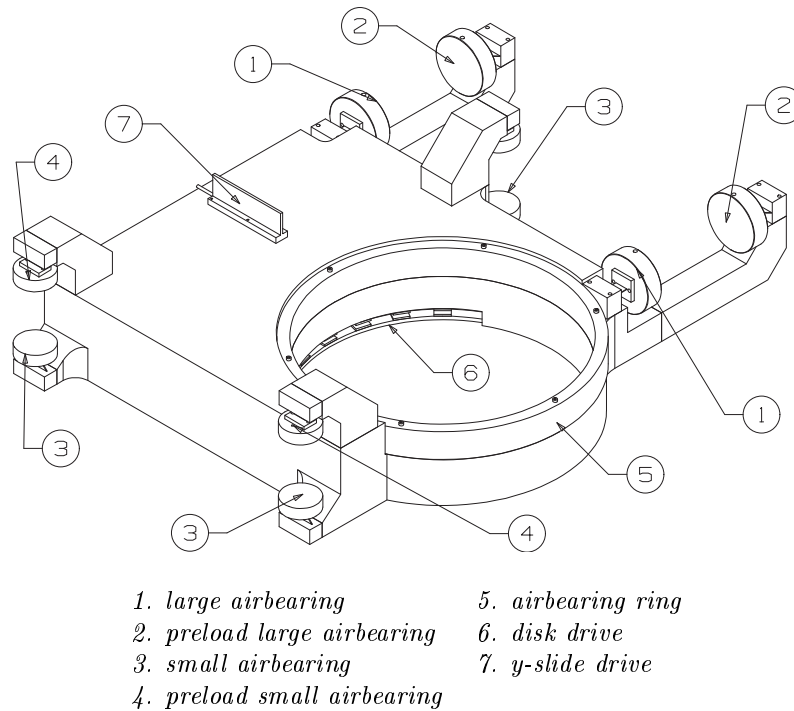


Figure 6.16: Assembled y-slide

sensorheads are mounted onto the horizontal granite slab, which makes the position of the sensorheads thermally stable, because of the large mass of the slab. Changes in the surrounding temperature will cause changes in the length of the slab on such a long time scale, it will be possible to calibrate the distance between the sensorhead and the workpiece between grinding steps.

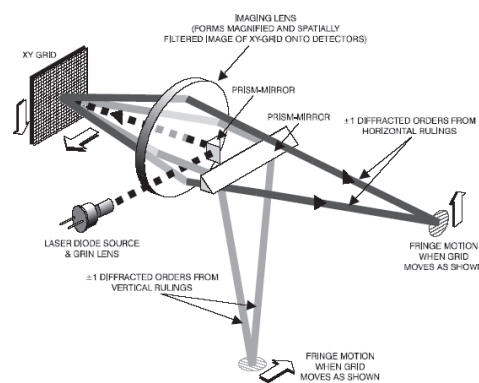


Figure 6.17: Nanogrid measurement principle

Y-slide drive

The y-slide is being actuated with an ironless linear motor. Because there is no physical contact between the two moving parts of the motor, there is no friction. Friction, together with the finite stiffness of the slide, causes virtual play, reducing the resolution of the drive. There are several reasons to prefer an ironless linear motor above a ball screw drive. First off all, a ball screw drive suffers from play and to

correct this a preloaded nut can be applied. But this creates additional friction and so increases virtual play. Also the ball screw nut should be mounted in a proper way, like [Suz95] did. For his precision grinder, he designed a coupling consisting of flexures, unconstraining all DOF's except the translation of the drive axis. This way the position of the y-slide is not overconstrained. Such a coupling must be manufactured carefully. Another type of coupling is described by [TUeo2]. A tube is cut-out at four lateral positions so a cardan joint is created. This cardan joint has a high axial stiffness and a high torsion stiffness. This fairly easily made component adds some length to the ball screw drive, but the drive is no longer overconstrained. Some advantages of a ball screw are that it is an indirect drive, so the motor used can produce a small torque at high speeds. This results in the use of a small motor that needs less current and thus produces less heat. A ball screw is also stiff above the bandwidth of the controller, a linear motor is not. An ironless motor, finally, does not have magnetic attraction between the two motor parts, as ironcore linear motors do. Ironless motors however have a lower force per volume unit than ironcore motors have. Moving the 100 kg weighing y-slide with tool spindle unit 5 mm at 1 Hz will require a force of 20 N. Adding the grinding force of maximum 1 N and a neglectable amount of friction force caused by the airbearings, an actuator of more than 21 N is sufficient.

Disk drive

The drive that actuates the tool disk resembles the y-slide drive. The coil is placed onto the tool disk and its windings are in the same way as in a disk armature motor. Instead of a translation like with the y-slide drive, a -partly- rotation is actuated. The magnets are placed on the y-slide and are orientated around the tool disk.

6.7 X-slide

6.7.1 X-slide assembly

The somewhat U-shaped x-slide, see figure 6.18, holds the y-slide near its centre line (4) so the tilting stiffness provided by the two y-airbearings (1) is maximized. The x-slide stands on three airbearings (2), suspending it on the horizontal plane. The y-slide guideways (3) are connected to either the left or right side of the frame. Some room was made so the preload airbearings of the y-slide can pass through. The magnets for the y-slide drive (4) are mounted on the centre line of the frame. The x-slide coils (5) are placed at the bottom of the right part of the frame. On top of the frame there is a top plate, for clarity reasons this plate is not shown in figure 6.18.

6.7.2 X-slide components

X-slide frame

Figure 6.19 shows the wire model of the x-frame with its system points. These points are used to mount parts to the frame and should be connected to each other in a stiff way. At the edge of the frame, the airbearings are mounted (1). This gives a high tilting stiffness, the large distance between the airbearings at the bottom side of the figure is especially important for the grinding process. Each of the y-slide guideways are connected at two points (2) so a line can be described for each guideway. The line, described by the two points of the x-slide drive coil (3), points at the centre of mass of all the moving slides. This way, when actuating the x-slide, no momentum is created that rotates the slide. Also the line described by the two points for the y-slide drive, points at the centre of mass of the y-slide and tool spindle unit. The system points are connected with lines in such a way that triangles are created. Finally aluminium is placed around the lines creating a physical frame. The lowest eigenfrequency is 257 Hz, at this mode the end points of the two 'legs' of the U-shape are symmetrically moving sideways, see E.2. The stiffness of the frame in y-direction is $c_y = 3.3 \cdot 10^8 \text{ N/m}$.

The frame assembly consists of three pieces, one centre piece and two side pieces. The connecting interfaces are just above the y-slide guideways. They are all milled from blocks of aluminium, this

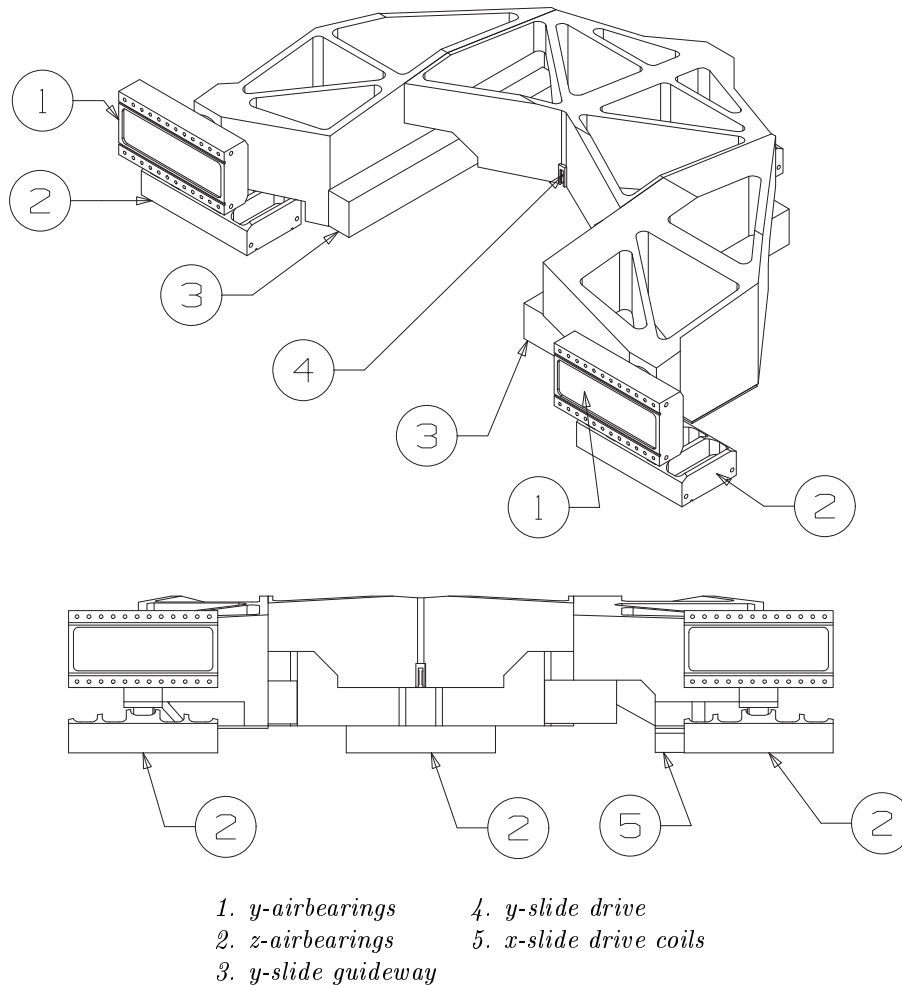


Figure 6.18: Assembled x-slide

way good interfaces can be made. The three frame pieces, the *y*-slide guideways and the five *x*-slide airbearings can be placed almost with machine accuracy. A frame made from many plates has to be assembled carefully and the interface areas for the airbearings and the *y*-slide guideways have to undergo final processing. Because there will be built only one of this grinder, the removal of the amount of material is not an important issue. Between the two interface areas of the three frame pieces, and between these three pieces and the top plate, silicone paste is applied. This paste is able to dampen frame vibrations, the aluminium is not able to do so. Inside the grinder there are many sources creating frame vibrations. First of all, the grinding process causes vibrations, because of the tool-workpiece interaction. The runout of the tool and the interaction of the different grains with the workpiece causes excitations. Secondly, the actuator forces moving the slides also cause vibrations. If all this kinetic energy is able to accumulate inside the machine frame, the amplitudes of the vibrations will increase. This can result in an unstable grinder and this will decrease the shape accuracy of the ground products. By using a material that is able to dissipate this energy, this instability can be prevented. The paste is not applied onto system points, so it does not decrease the frame stiffness. This is illustrated in figure 6.20, it shows part of the *x*-frame. The system points are connected to each other through clamp zones. Because of the high contact pressure, there is little or no hysteresis at these zones. Between the system points there are damping zones. Small amounts of material are removed from the *x*-frame, so spaces are created between the frame parts. These spaces are filled with paste. Because silicone paste, like other damping materials, behave in a viscoelastic way, the

dissipated energy depends only on the velocity of the frame part. When this velocity is reduced to zero, the material is returned to its nominal position, so there is no virtual play.

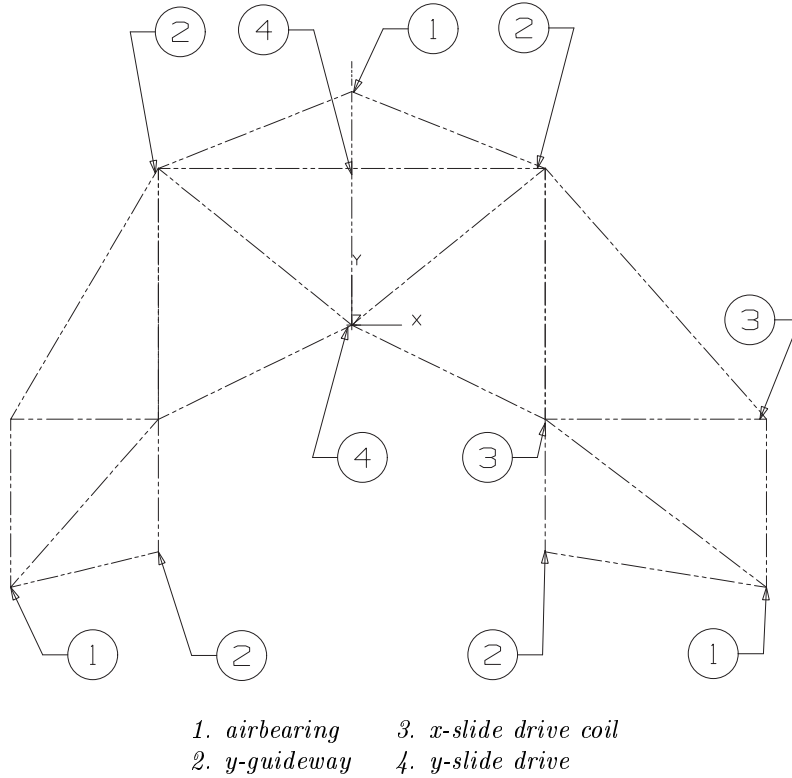


Figure 6.19: Wire model of x-frame with system points

Airbearings

Airbearings, or aerostatic bearings, are known for their frictionless movement and are used in many precision applications. In order to get a stiff bearing, the airbearing must be preloaded against a surface. There are several ways to do this. One can use the weight of the machine part that is carried by the bearing, but this does not allow fine tuning the bearing by adjusting the preload force. Another way is to use a preload airbearing at the other side of the guideway, this is done with the y-slide as shown in 6.6. For the x-slide however the preload brackets would have been very large, because they will have to reach the other side of the 300 mm thick granite block. Also the bottom of the horizontal slab must be smooth and flat enough to allow the preload bearing to work. For these reasons the choice is made to preload the bearing using vacuum (underpressure).

A number of different airbearings were examined in [Ver99]. Two of these looked very interesting for the grinder because of their stiffness, their manufacturing process and the way a vacuum chamber can be integrated. These two bearings are shown in figure 6.21. The one on the left is a bearing consisting of porous graphite. The graphite works as many restrictors. The one on the right is a bearing with a parallel gap between the bearing and the surface, and it has a graphite insert as a restrictor. This disk spreads the pressure of the flowing air more than a bearing with a single hole restrictor. The properties of bearing with a single hole restrictor may deteriorate when the restrictor is above a crack in the underlying surface. Because that surface is made from granite, it is expected that some of these cracks exist. Bearings with porous restrictors are insensitive to these cracks.

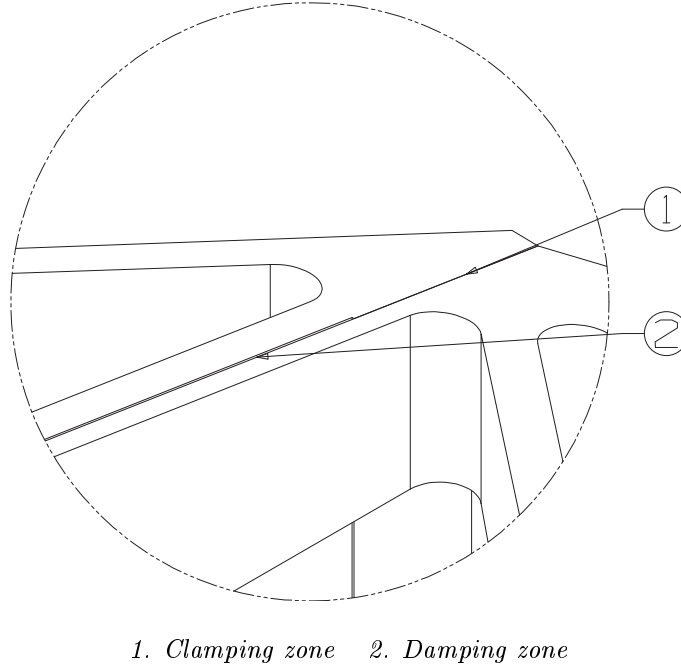


Figure 6.20: Frame interface

The properties of the two bearings are stated in table 6.1. It shows that the optimal stiffness that can be acquired per unit of surface is slightly higher with the porous grafite bearing. But this also requires a larger preload force. Because of this higher preload force, the actual bearing surface of the porous grafite bearing may be smaller, the required vacuum surface is many times larger than the surface of the grafite insert bearing. The total amount of bearing surface of the grafite insert bearing is about three times smaller than that of the porous grafite bearing. So the choice is made to use the parallel gap bearing with a grafite insert.

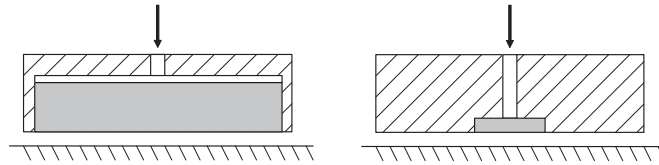


Figure 6.21: Left: porous grafite bearing, right: parallel gap bearing with grafite insert

Bearing type	Porous grafite bearing	Grafite insert 8mm	
c_{opt}/A	1.8	1.6	$[N/\mu m/cm^2]$
$F(c_{opt})/p_s A$	0.66	0.15	$[-]$
$F(c_{opt})$	3.6	0.8	$[kN]$
$A_{bearing}$	83	94	$[cm^2]$
A_{vacuum}	590	135	$[cm^2]$
A_{total}	673	229	$[cm^2]$

Table 6.1: $p_s = 6.0 \text{ bar}$, $c_{bearing} = 150N/\mu m$, the pressure in the vacuum chamber is 0.4 bar .

Figure 6.22 shows the design of the airbearing for the x-slide. The bottom view shows the airbearing surface with the grafite inserts. The space between two inserts is equal to the airbearing surface width, to optimize the surface usage. Placing the vacuum chamber between the two airbearing surfaces provides a stable system. When the airbearing is tilted to one side, the gap height between the bearing and the ground surface is decreased, causing an increase in resistance for the airflow. Less airflow causes the difference in pressure before and after the grafite insert to be less, so the air pressure at the parallel gap is increased. This increase in pressure will try to return the tilted airbearing to its nominal position. Two atmospheric grooves are necessary to have a symmetrical airflow out of the inserts. This way all of the airbearing surface is used. The air is supplied by four bores, two on each short side reaching half way across the length of the bearing. The airbearing is stiffened by six plates parallel to the short sides. The greatest deflection of the bearing is caused by the airflow pressing it up and the vacuum chamber pulling it down. So this deflection is mostly created by bending as seen from the short side. The six high plates are very suited to deal with this bending. In E.5 the stress is shown as a result of the airflow, with a maximum value in the top centre of the high plates.

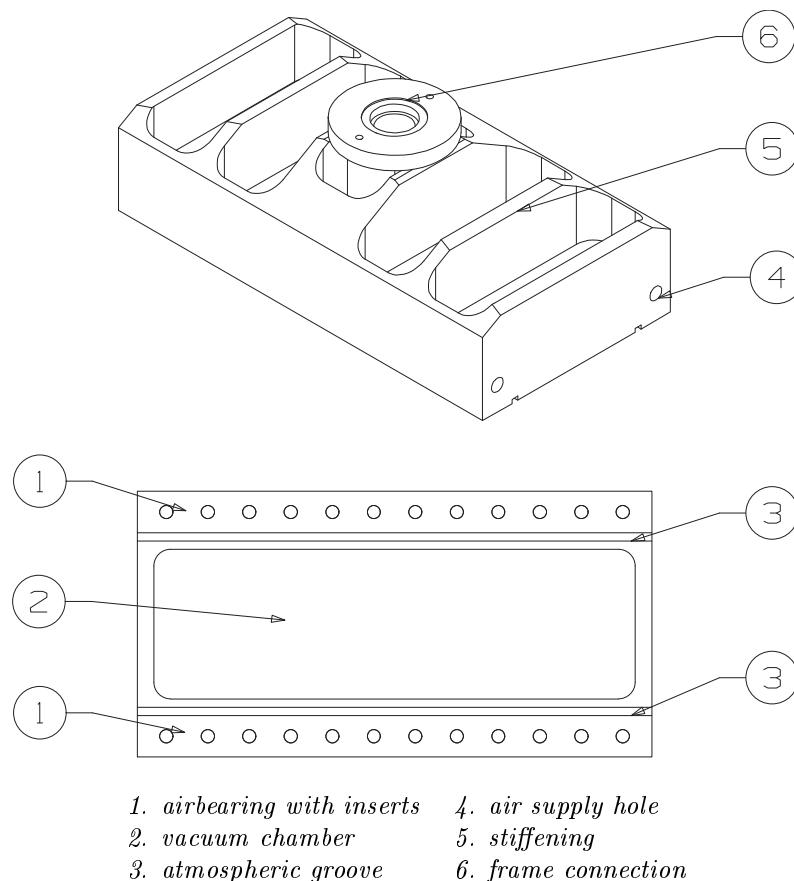


Figure 6.22: Isometric and bottom view of air bearing

6.8 Base

6.8.1 Base assembly

The base consists of two large granite slabs. The horizontal slab (3) is used as the bearing plane for the tool spindle and the x-slide. On this slab a vertical slab (2) is placed, holding the workpiece spindle

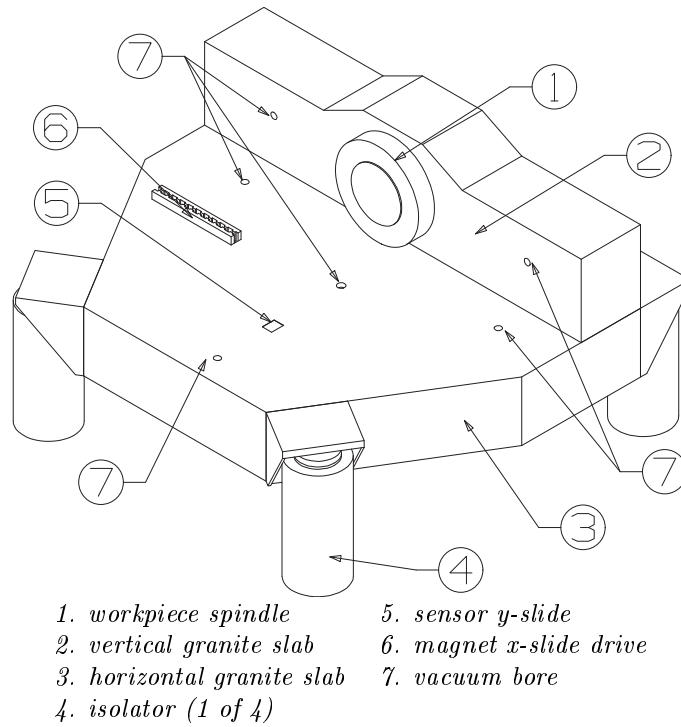


Figure 6.23: Base assembly

(1). The horizontal slab contains space for the position sensors of the y-slide and the magnets of the x-slide drive. Also four brackets are bolted to the horizontal slab for the isolator connections (4). Finally holes (7) are drilled into the granite, providing underpressure to the bearings suspending the tool disk and the x-slide. If vacuum was applied through cables, very thick cables would be needed to prevent the atmospheric pressure from squeezing the cables. These thick, stiff cables cause disturbing forces when the slides are being moved. Applying vacuum through a bore prevents the need of having moving cables at the top side of the grinder. The cables placed at the end of the vacuum bores, leading to the pump, can be properly concealed beneath the machine.

6.8.2 Base components

Granite blocks

The properties of the granite are given in I. Granite is often used for precision instruments like CMM's, because very flat surfaces can be created, less than $1 \mu m/m^2$. Also the large solid blocks are thermally very slow, so changes in temperature do not result in length changes quickly.

Isolator system

Vibrations caused by the environment of the grinder, e.g a passing truck or a slamming door, can cause shape errors on the workpiece. Therefore the grinder has to be isolated by placing it on springs with very low stiffness. Such a situation is given in figure I where a mass is placed onto two springs. The centre of mass M_c is distance h above the line between the isolators. When the machine is tilted with angle β the sum of the momentum on point A is

$$\Sigma M_a = F_c L + F_c L - mgh \sin(\beta) \quad (6.3)$$

	$m[kg]$ or $J[Nm/s^2]$	f_{eig}
x-translation	3200	1.5
y-translation	3200	1.5
z-translation	3200	1.0

Table 6.2: Lowest eigenfrequencies of isolated grinder

$$\Sigma M_a = 2cL^2 \sin(\beta) - mgh \sin(\beta) > 0 \quad (6.4)$$

$$2cL^2 > mgh \quad (6.5)$$

When equation 6.5 is true the forces applied by the two springs will be able to push the mass back to the nominal position and there is a stable system. The distance h on the grinder is reduced to almost zero by placing the isolator brackets as high as possible on the horizontal slab. The centre of mass of the entire machine is just below the top surface of the horizontal slab, so the isolator system is stable. The isolator brackets are placed in such a way that the roll frequency in the x- and y-direction is about the same. Table 6.2 shows the lowest eigenfrequencies in x-, y- and z-direction. Figure 6.25 shows the weight on each of the isolators,

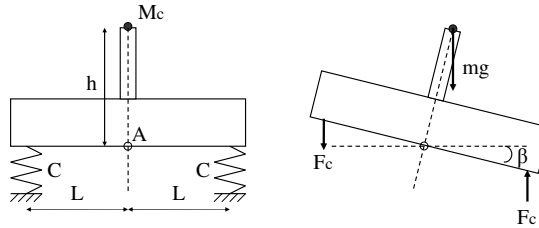


Figure 6.24: Analyzing an isolated body

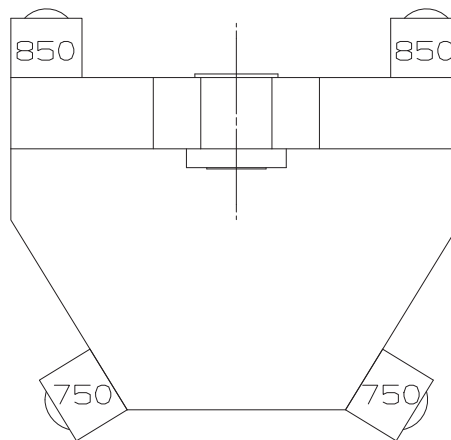


Figure 6.25: Weight per isolator (kg)

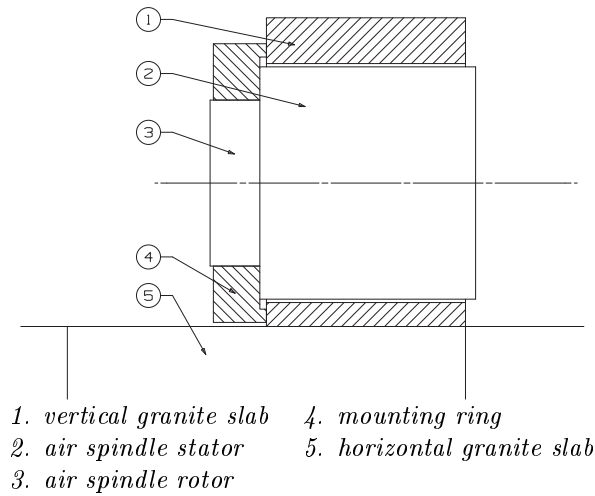


Figure 6.26: Workpiece spindle in base

Workpiece spindle

The workpiece spindle is a motorized Blockhead 10R. This spindle features a high stiffness, $c_{ax} = 1750 \cdot 10^6 N/m$ and $c_{rad} = 350 \cdot 10^6 N/m$ and a runout of less than 25 nm. The spindle should have an accurate position encoder, so free-form features may be ground at the right position on the workpiece. The mounting ring allows the top surface of the stator to be aligned with the vertical granite slab surface. This minimizes thermal length and creates a stable workpiece position. The use of the mounting ring also simplifies the manufacturing process. The vertical granite slab can have a rough through hole. The mounting ring can be made with a very good flatness, so it connects well with both the granite and the spindle. It is difficult to mill precision counterbores in granite. By moving the mounting ring, the workpiece spindle can be aligned and fixed. The mounting ring is bolted to the vertical slab using inserts.

Chapter 7

Conclusions and recommendations

7.1 Conclusions

When grinding brittle glass in a ductile way, the quality of the surface is improved, because of the absence of subsurface damage. This reduces polishing time and this is especially important for free-form optics. These optics can be polished only locally and it is a great amount of work just to improve the surface roughness, let alone remove subsurface damage. A grinder that features a controllable grinding force, so subsurface damage is prevented, is necessary for TNO to improve the manufacturing process of single piece optical components. The grinder should also be able to grind free-form optics with a good shape accuracy so they can be used for scientific and industrial purposes.

A precision grinder with a controlled-force tool spindle is designed. The tool spindle is designed in such a way it can be used for experiments on an existing platform. This tool spindle features a rotor with an elastic guideway inside. This guideway is actuated with a voice coil which can apply a set force. To reduce the influence of inertial forces of this guideway on the grinding process, the amount of mass is minimized. For the workpiece to get a good shape accuracy the position of the tool drive is measured using two inductive sensors. These sensors provide the information for the voice coil to either keep applying force on the workpiece or to stop because the desired shape is achieved.

The tool spindle is mounted on a large diameter disk that is suspended with an airbearing on a granite surface. This way the only DOF's that need to be unconstrained are not constrained. To actuate these constrains the tool disk is hold by the y-slide. This relative fast slide allows the grinder to make free-form features into rotational-symmetric workpieces. The y-slide is hold by the slow x-slide, that continuously moves radially across the workpiece surface.

By measuring the position of the y-slide directly from the granite base, many errors of the x- and y-slides can be measured. This improves the accuracy of the grinder and the desired accuracy is achieved.

Finally calculations are made showing that the required accuracy is achieved and the grinder has a good dynamical behavior.

7.2 Recommendations

Motor stator

The design of the tool spindle is emphasized so shortly after the completion of this thesis, experiments can begin examining the potential of controlled-force grinding. The motor stator however still needs to be determined. The outer dimensions have been estimated, so enough room is reserved. This

estimation was done by looking at the dimensions of similar motors and motors with more power. So this will not have a big impact on the spindle design.

Support frame

To load and unload the grinder properly, an operator support frame is needed, see figure 7.1. It must support the operator in a partly lying position. It also must prevent people from leaning onto the machine, tilting it on its isolators. This can easily bring one of the isolators to the end of its stroke. Then surrounding vibrations will not be resisted and will cause workpiece errors. The support frame can be made from tubes and plates welded together to limit the weight. The interface with the operator should be adjustable in height and angle, so the working position can be customized for each operator. Also a cover is needed to shield the surroundings from the grinding fluid. Especially the airbearings need good covering to prevent them from being scratched. A scratch can reduce the performance of the bearing.

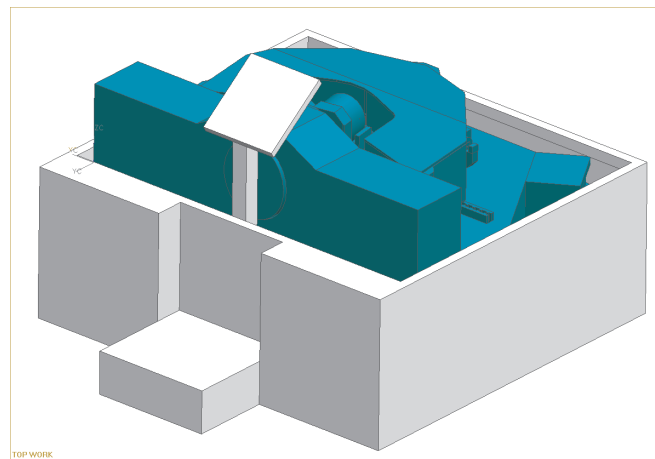


Figure 7.1: Support frame recommendation

Optimization and detailing

Some optimization can still be done to the design of the grinder. This includes improvement of the manufacturability, so parts can be made in an easier way, saving time and money. Also some machine parts need more detailing, such as the way the isolators are connected to their brackets. The position of the mounting holes and the bolts that should be used are not determined yet.

Bibliography

- [Bif91] T. G. Bifano, *Ductile-regime grinding: a new technology for machining brittle materials*
Journal of Engineering for Industry, Vol 113, pag 184-189, (1991)
- [Bla88] P. Blake, *Precision machining of ceramic materials*
Ceramic Bulletin, Vol 67, pag 1038-1044, (1988)
- [Bol99] B. P. A. Bollen, *Een ontwerp van een machine voor het fabriceren van asferische lenzen, volgens de methode van W.A.G.N.E.R.*
Master thesis, Technisch Universiteit Eindhoven, reportnumber PE99-022, (1999)
- [Boo03] Silvia M. Booij, *Fluid jet polishing*
PhD thesis Delft University of Technology, (2003)
- [Cou04] Jermiah A. Couey, Eric R. Marsh et al., *Monitoring force in precision cylindrical grinding*
Precision Engineering, Vol. 29, pag 307-314, (2004)
- [Fäh98] Oliver W. Fahnle, *Shaping and finishing of aspherical optical surfaces*
PhD thesis Delft University of Technology, (1998)
- [Fäh99] O. W. Fahnle, H. van Brug, *Novel approaches to generate aspherical optical surfaces*
Proceedings of SPIE, Vol 3782, pag 170-180, (1999)
- [Fano4] F. Z. Fang, G. X. Zhange, *An experimental study of optical glass machining*
Int J Adv Manuf Technol, no 23, pag 155-160, (2004)
- [Fis00] Anthony C. Fischer-Cripps, *Introduction to contact mechanics*
Springer-Verlag New York Inc., (2000)
- [Fra91] Jelm Franse, *Aspects of precision grinding*
PhD thesis, Technisch Universiteit Eindhoven, (1991)
- [Halo4] Layton C. Hale, *Testing a low-influence spindle drive motor*
Precision Engineering, Vol 29 pag 1-10, (2004)
- [Hah64] R. S. Hahn, *Controlled-force grinding, a new technique for precision internal grinding*
Journal of Engineering for Industry, Vol 86, pag 287-293, (1964)
- [Heg00] J. B. J. W. Hegeman, *Fundamentals of grinding, surface conditions of ground materials*
PhD thesis Rijksuniversiteit Groningen, (2000)
- [Hen05] Rens Henselmans, Nick Rosielle et. al., *Design of a machine for the universal non-contact measurement of large free-form optics with 30 nm uncertainty*
Proceedings of SPIE, Vol 5869 pag 586919-1 - 586919-12, (2005)
- [Hölo2] W. Höland, G. Beall, *Glass-ceramic technology*
The American Ceramic Society, Westervill, Ohio, (2002)

- [Kar93] H. H. Karow, *Fabrication methods for precision optics*
John Wiley and Sons Inc, New York, (1993)
- [Kra] H. J. J. Kraakman, *Precisie produktie, "Hoe en waarmee"?*
Philips Centre for Manufacturing Technology, CFT Mechatronics
- [Lam97] J. Lambropoulos, *Subsurface damage in microgrinding optical glasses*
University of Rochester, LLE Review, Vol 73, pag 45-49, (1997)
- [Law77] B. R. Lawn, *A model for crack initiation in elastic/plastic indentation fields*
Journal of Materials Science, Vol 12, pag 2195-2199, (1977)
- [Law80] B. R. Lawn, A. G. Evans, *Elastic/plastic indentation damage in ceramics: The median/radial crack system*
Journal of the American Ceramic Society, Vol 63, no 9-10 pag 574-581, (1980)
- [Law95] Brian Lawn, *Fracture of brittle solids - second edition*
Press Syndicate of the University of Cambridge, (1995)
- [Li98] K. Li, Y. Shapiro, J. C. M. Li, *Scratch test of soda-lime glass*
Acta mater., Vol 46, No 15, pag 5569-5578, (1998)
- [Mal89] S. Malkin, *Grinding technology, theory and application of machining with abrasives*
Ellis Horwood Limited, Chichester, West Sussex, England, (1989)
- [Mee05] M. Meeder, W. A. C. M. Messelink, O. W. Föhnle, *Analysis of the ductile-brittle transition in loose abrasive grinding*
Proceedings of SPIE, Vol 5869, pag 58690M-1 - 58690M-6, (2005)
- [Mül98] H. K. Müller, B. S. Nau, *Fluid sealing technology, principles and applications*
Marcel Dekker Inc, New York, (1998)
- [Nam89] Y. Namba, *Ultra-precision surface grinder having a glass-ceramic spindle of zero-thermal expansion*
Annals of the CIRP, Vol 38(1) pag 331-334, (1989)
- [Pau87] P. Paul, D. F. Edwards, *Optical glass fabrication technology. 2: Relationship between surface roughness and subsurface damage*
Applied optics, Vol 26, no 21 pag 4677-4680, (1987)
- [Qia04] J. Qian, P. Vleugels, *A novel design for a high precision freeform ELID grinding-machine*
Proc. of 4th euspen international Conference-Glasgow, Scotland(UK), (May-June 2004)
- [Row83] W. B. Rowe, *Hydrostatic and hybrid bearing design*
Butterworth&Co, London, (1983)
- [Sch98] P. Schellekens, N. Rosielle, et. al., *Design for precision: Current status and trends*
Annals of the CIRP, Vol 47(2) pag 557-586, (1998)
- [Sha96] Milton C. Shaw, *Principles of abrasive processing*
Oxford University Press Inc., New York, (1996)
- [Suz95] H. Suzuki, S. Murakami, *An ultraprecision grinding machine for non-axisymmetric aspheric mirrors*
Nanotechnology, Vol 6 pag 152-157, (1995)
- [TUeo2] Lecture note 4007 (in Dutch), *Constructieprincipes 1*
Eindhoven University of Technology, (2002)

- [TUe03] Lecture note 4U700 (in Dutch), *Uitreikbladen nauwkeurigheid van machines*
Eindhoven University of Technology, (2003)
- [Ver99] Hans Vermeulen, *Ceramic optical diamond turning machine*
PhD thesis, Technische Universiteit Eindhoven, (1999)
- [You87] M. Younis, M. M. Sadek, T. El-Wardani, *A new approach to development of a grinding force model*
Transactions of the ASME, Journal of Engineering for Industry, Vol. 109, pag 306-313, (1987)

Notation

Symbol	Unit	Description
A_c	$[m^2]$	Tool contact area
d	$[m]$	Penetration depth, depth of cut, infeed
d_c	$[m]$	Critical penetration depth
d_{max}	$[m]$	Maximum infeed for grinder
E	$[Pa]$	Young's modulus
E_c	$[J]$	Energy needed for crack formation
E_p	$[J]$	Energy needed for plastic deformation of workpiece
F_c	$[N]$	Cutting grinding force
F_c	$[N]$	Force applied by spring with stiffness c
F_n	$[N]$	Normal grinding force
F_{nc}	$[N]$	Part of normal grinding force needed for cutting
F_{np}	$[N]$	Part of normal grinding force needed for ploughing
F_{nr}	$[N]$	Part of normal grinding force needed for rubbing
H	$[Pa]$	Hardness
K_c	$[Pa\sqrt{m}]$	Fracture toughness
k_1	$[N/mm^2]$	Chip thickness coefficient
K_l	$[\frac{N}{unitLa}]^2$	Loading force coefficient
L_a	$[-]$	Loaded tool area / total tool area
L_c	$[m]$	Tool contact length
p	$[Pa]$	Pressure
R	$[m]$	Radius
v_t	$[m/s]$	Tool speed
v_w	$[m/s]$	Workpiece speed
w	$[m]$	Width of cut
α	$[^\circ]$	Angle between tool and workpiece
α_f	$[\frac{N}{mm^2}]$	Ploughing grain coefficient
ν	$[-]$	Poisson ratio

Table 7.1: Notation

Appendix A

Assembly drawings

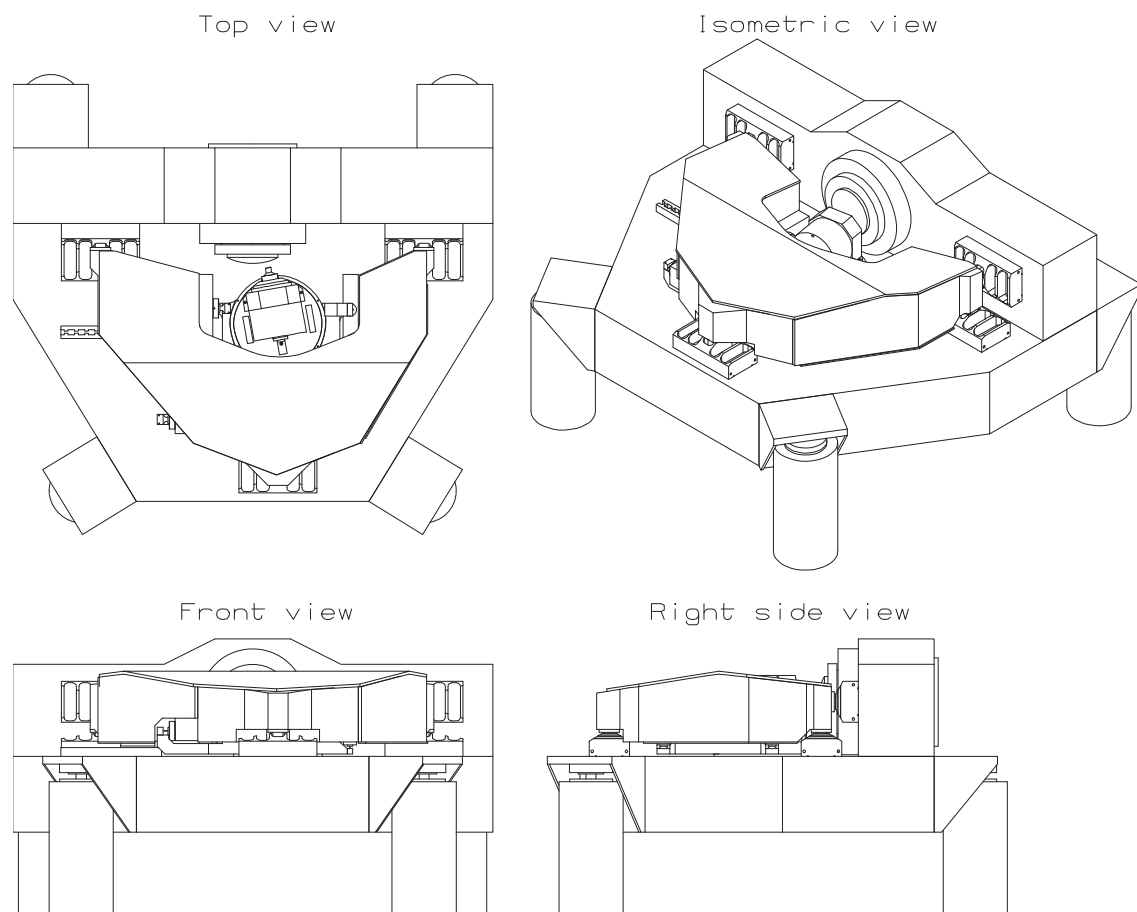
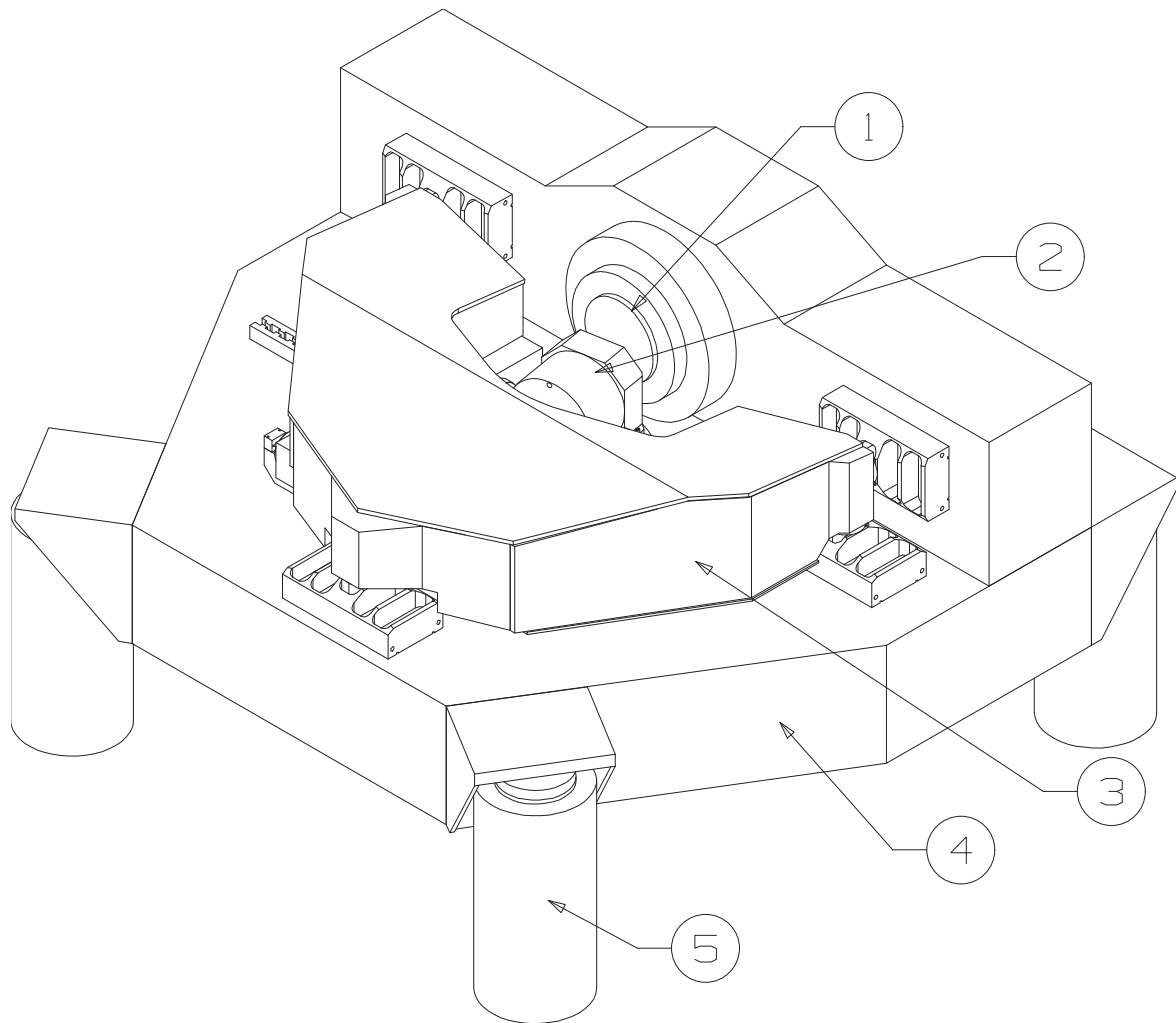


Figure A.1: Assembly views



- | | |
|-----------------|-------------|
| 1. workpiece | 4. base |
| 2. tool spindle | 5. isolator |
| 3. x-slide | |

Figure A.2: Assembly trimetric view

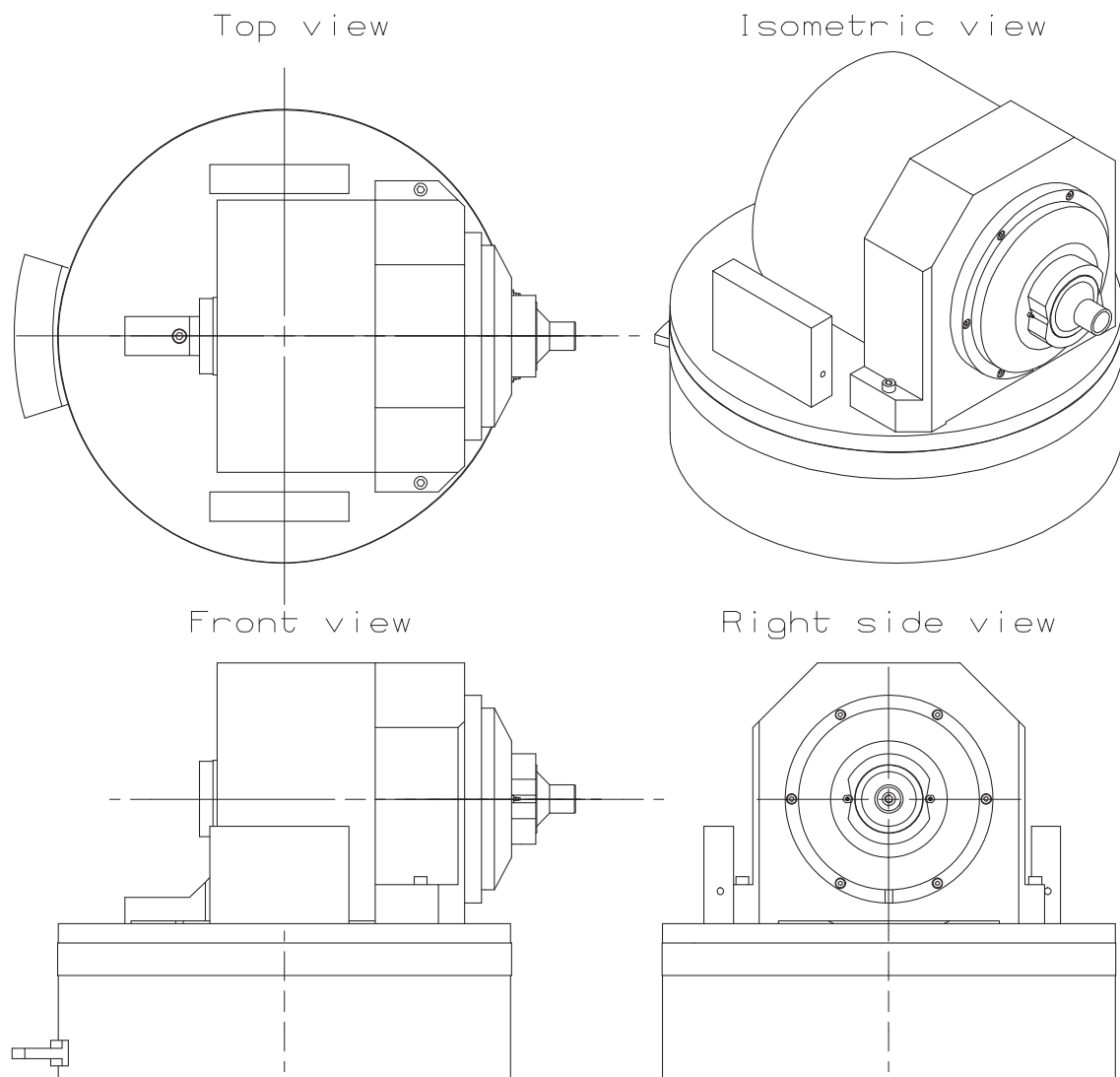
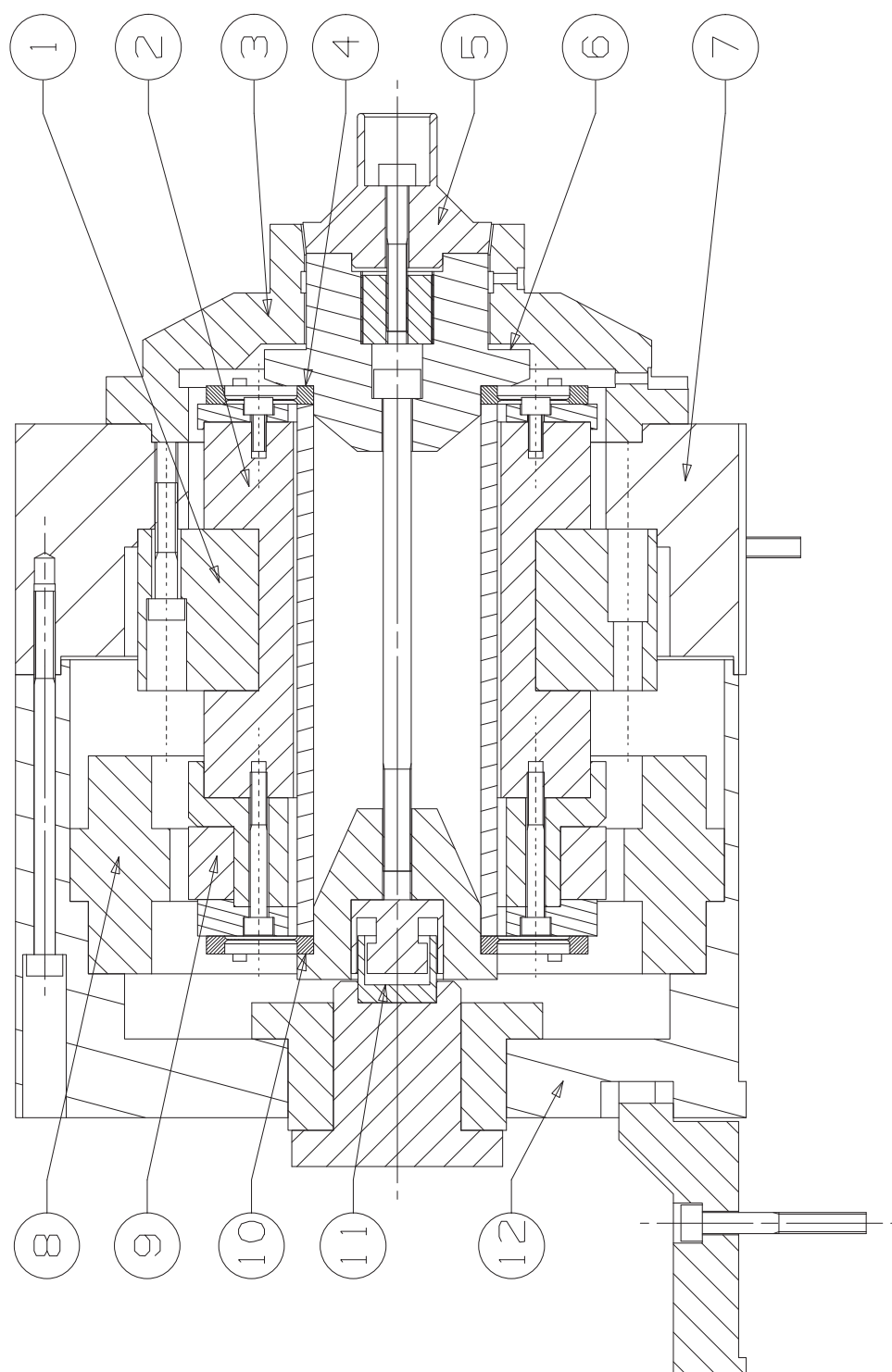


Figure A.3: Assembly views of tool spindle



- | | |
|--------------------------------|--------------------------------|
| 1. air spindle stator | 7. toolholder front |
| 2. air spindle rotor | 8. motor stator |
| 3. measurement frame | 9. motor rotor |
| 4. front membrane (inner ring) | 10. back membrane (inner ring) |
| 5. tool | 11. voice coil |
| 6. measurement flange/face | 12. toolholder back |

Figure A.4: Section view of tool spindle

Appendix B

Summary machine properties

Part	Property	Value	Description
Workpiece	Diameter	< 200 mm	One fifth of the maximal diameter Tangential speed is 1/100 of tool speed for $D_{workpiece} > 25$ mm
	Height	< 40 mm	
	Rotational speed	< 60 rmp	
Tool	Diameter	20 mm	Max. voice coil continuous force $\pi D_{tool} N_{toolspindle}/60$
	Length	30 mm	
	Max. normal force	4.6 N	
	Rotational speed	7 m/s	
Tool spindle	Rotational speed	7000 rmp	Allows use of accurate, stiff commercially available spindles Max. tangential grinding force = max. normal force $4.6 \cdot 2\pi R_{tool} N_{toolspindle}/60$
	Power	50 Watt	
X-slide	Stroke	230 mm	
Z-slide	Stroke	80 mm	
	Speed	5 mm /rev workpiece	
Disk	Stroke	-45° .. +45°	
Machine	Accuracy	0.68 μm	Off-axis error
		0.30 μm	Axial error
	Stiffness c_x, c_y	$3.2 \cdot 10^6 N/m, 21 \cdot 10^6 N/m$	

Table B.1: Machine properties

Appendix C

Tool spindle cost

Here the estimated cost of the tool spindle are given. Table C.1 gives an overview of the cost.

Air spindle

The air spindle used is a Blockhead 4R2.25, made by Professional Instruments. The price of 5000 euro is based on the price of the Blockhead 4R, which is a similar spindle, only with a smaller diameter hole in the rotor. The price of the 4R is 5000 dollar and taken into account a slightly higher price for the larger rotor hole, additional cost like shipping, the price of 5000 euro is estimated.

Motorization air spindle

The costs of motorizing the air spindle is estimated at 12000 euro. This is based on the prices of the motorization of other Blockhead air spindles. Because of the relatively low power needed from the motor, the real price is expected to be lower than the estimated price.

Inductive measurement system

The chosen inductive measurement system is the ECL100-U3B-10kHz-SAM made by Lion Precision. An offer invited at their representative at IBS Precision Engineering in Eindhoven, showed that the price of one system is 1500 euro. The total price for two systems is 3000 euro.

Fabricated parts

It is more challenging to estimate the cost of the parts that are to be custom fabricated, than the parts that can be bought. The cost of the fabricated parts depends heavily on the desired manufacturing tolerances. Tight tolerances require more time for loading the part into a machine, additional steps such as heat treatment may be necessary and the amount of material removed per time unit is smaller. Because the exact tolerances of the spindle part are not known at this time, it is possible to make only a rough estimation of the cost. These parts will cost 5000 - 10000 euro. Additional cost to assemble the tool spindle also have to be made.

Part	Cost (euro)
Air spindle	5.000
Motorization air spindle	12.000
Inductive measurement system	3.000
Fabricated parts	10.000
Total cost	30.000

Table C.1: Overview cost tool spindle

Appendix D

Dynamical model

In order to study the dynamical behavior of the entire grinder, a dynamical model has been made. This model is shown in figure D.1. All the bodies of the model can move in x-direction (horizontally), in y-direction (vertically) and can rotate along the z-axis, ϕ . The relatively stiff frame parts are modeled as rigid bodies, where as the airbearings between the different slides are modeled as springs. This way a relatively simple model is produced, giving a fairly good estimation of the lowest and thus the most important eigenfrequencies.

The tool drive is represented with the first mass, with m_1 , J_1 . It is suspended in x-direction with a spring with stiffness cx_1 and suspended in y-direction with a spring with stiffness cy_1 . Rotation ϕ_1 is suspended with torsion spring k_1 . The second mass with m_2 and J_2 is the combination of the rotor and stator of the air spindle and the tool disk. The rotor and stator of the air spindle are modeled as one rigid mass, because of the small weight of the rotor and the stiff radial airbearing between them. The mass of the rotor is 3,5 kg and using the radial stiffness of the air spindle being $c_{rad} = 120N/\mu m$ this gives an eigenfrequency of $f_{eig} = 931Hz$, which is much higher than the eigenfrequencies of the other components. So this simplification is justified. The third body with m_3 and J_3 is the y-slide and finally the x-slide is modeled with body four, m_4 and J_4 . The x-slide is connected through springs to the fixed world. Table D.1 describes the model parts and gives their values.

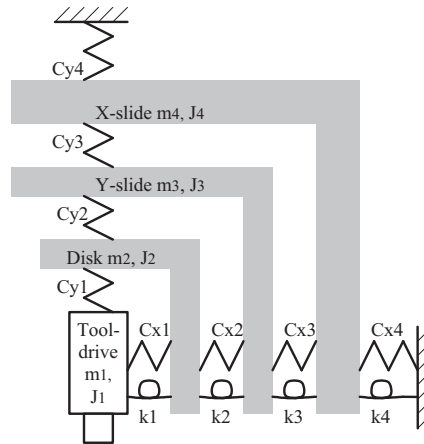


Figure D.1: Dynamical model

The model to determine the eigenfrequencies is described by

$$\mathbf{M}\ddot{\mathbf{x}} + \mathbf{K}\mathbf{x} = 0 \quad (\text{D.1})$$

Part	Description	Value	Unit
m_1	Tool drive mass	1.9	kg
m_2	Rotor+stator+tool disk mass	41	kg
m_3	Y-slide mass	57	kg
m_4	X-slide mass	214	kg
J_1	Moment of inertia of tool drive	0.0011	$kg \cdot m^2$
J_2	Rotor+stator+tool disk	0.54	$kg \cdot m^2$
J_3	Y-slide	3.2	$kg \cdot m^2$
J_4	X-slide	51	$kg \cdot m^2$
cx_1	Radial membrane stiffness	$18 \cdot 10^6$	N/m
cx_2	Radial tool disk air bearing	$100 \cdot 10^6$	N/m
cx_3	Airbearings y-slide	$220 \cdot 10^6$	N/m
cx_4	X-drive actuator	$100 \cdot 10^6$	N/m
cy_1	Radial membrane stiffness	$18 \cdot 10^6$	N/m
cy_2	Radial tool disk air bearing	$100 \cdot 10^6$	N/m
cy_3	Y-drive actuator	$50 \cdot 10^6$	N/m
cy_4	Airbearings x-slide	$300 \cdot 10^6$	N/m
k_1	Radial membrane stiffness	$51 \cdot 10^3$	Nm/rad
k_2	Airbearings disk + actuator disk	$562 \cdot 10^3$	Nm/rad
k_3	Airbearings y-slide	$5324 \cdot 10^3$	Nm/rad
k_4	Airbearings x-slide	$54000 \cdot 10^3$	Nm/rad

Table D.1: Model parameters and values

where \mathbf{M} is a matrix consisting of all the masses and moments of inertia of the model. \mathbf{K} consists of the (torsion) springs. x is an array of all the degrees of freedom of the model. Using the parameters from table D.1, then equation D.1 is as follows

$$\begin{pmatrix} m_1 & 0 & \dots & & & \\ 0 & m_1 & & & & \\ \vdots & & J_1 & & & \\ & & & \ddots & & \\ & & & & m_4 & \\ & & & & & J_4 \end{pmatrix} \begin{pmatrix} \ddot{x}_1 \\ \ddot{y}_1 \\ \ddot{\phi}_1 \\ \ddot{x}_2 \\ \vdots \\ \ddot{\phi}_4 \end{pmatrix} + \begin{pmatrix} cx_1 & 0 & 0 & -cx_1 & & & & & \\ 0 & cy_1 & \ddots & & -cy_1 & & & & \\ 0 & \ddots & k_1 & & & -k_1 & & & \\ -cx_1 & & & cx_1 + cx_2 & & & -cx_2 & & \\ & \ddots & & & \ddots & & & \ddots & \\ & & k_2 & & & k_2 + k_3 & & & -k_3 \\ & & & -cx_3 & & & cx_3 + cx_4 & \ddots & 0 \\ & & & & -cy_3 & & & cy_3 + cy_4 & 0 \\ & & & & & -k_3 & 0 & 0 & k_3 + k_4 \end{pmatrix} \begin{pmatrix} x_1 \\ y_1 \\ \phi_1 \\ x_2 \\ \vdots \\ \phi_4 \end{pmatrix} = \mathbf{0}$$

and it can be shown that the three lowest eigenfrequencies are $f_{eigen,1} = 77Hz$, $f_{eigen,2} = 87Hz$ and $f_{eigen,3} = 139Hz$. Although the real eigenfrequencies will be lower, because the frame parts are

assumed rigid, the lowest eigenfrequency is high enough for the grinding process. The figures D.2 and D.3 illustrate the corresponding eigenmodes. The first eigenmode in figure D.2 shows that the y-slide and the x-slide move the most, relatively to each other. So increasing the stiffness between them, the y-drive actuator stiffness cy_3 , is an efficient way to increase the lowest eigenfrequency. The most movement in the second eigenmode, figure D.3(a), takes place at the airbearings of the y-slide, cx_3 , where the y-slide is connected to the x-slide. When the first eigenfrequency has been increased, it will be usefull to use stiffer y-slide airbearings to increase the second eigenfrequency. Finally the third eigenfrequency can be increased by improving the torsion stiffness between the tool disk and the y-slide, see figure D.3(b). This means increasing the stiffness of the radial airbearing of the tool disk and increasing the disk drive stiffness.

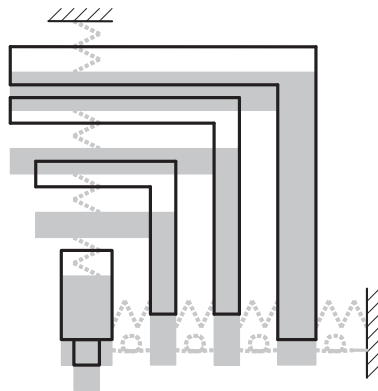


Figure D.2: First eigenmode at 77 Hz. The gray parts represent the nominal position.

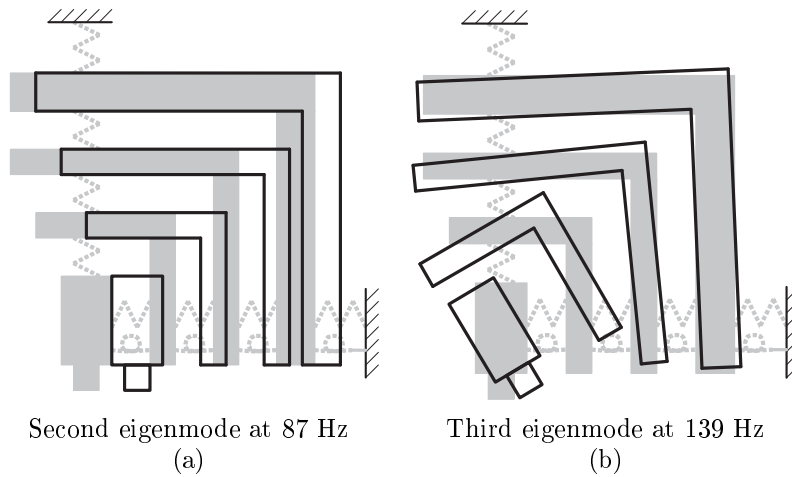


Figure D.3: Second eigenmode and third eigenmode

Appendix E

FEM-calculations

E.1 Introduction

After the global model of the entire grinder made in appendix D, some critical machine parts have been modeled with Finite Element Method. This way a more accurate dynamical behavior of the machine parts can be acquired. These models are also used to check whether the assumptions used in the dynamical model of appendix D are correct.

E.2 X-frame

A FEM-calculation is made for the frame of the x-slide to determine the stiffness and to get an insight of the level of stress inside the frame. In figure E.1 the von Mises stress is given. A force is applied on the centre line of the frame, where the y-slide drive is placed. The bottom side of the figure, where the airbearings to the vertical granite slab would be, is set as a fixed boundary condition. Because of the small process forces, the stresses on the frame are low. There is no risk of fatigue or exceeding the yield strength of the aluminum. The figure gives an insight on how the stress is divided over the frame. The exact value is not really important. The figure shows that the stress is equal on most of the frame, except for a few areas. The highest stress is in the middle of the figure on the centre line of the top plate. By moving this point as close as possible to the bottom side of the figure, the stress is reduced. More movement is not possible, because else the top plate would interfere with the tool spindle. When looking at the displacement of the point where the force is applied, the stiffness in y-direction can be determined. The y-stiffness of the x-frame is $3.3 \cdot 10^8 N/m$.

Also the dynamical behavior of the frame is examined. Figures E.2 - E.4 show that the three lowest eigenfrequencies are at 257 Hz, 462 Hz and 582 Hz. The corresponding eigenmodes are also given. Because these eigenfrequencies are much higher than the lowest eigenfrequencies of the dynamical model of appendix D, the dynamics of the x-frame do not play a significant role in the dynamics of the entire grinder.

E.3 Vacuum seal

The vacuum seal used to seal the top of the tool disk is examined more closely. A thin sheet that is fixed axially to a mounting ring must prevent the atmospheric pressure to deform the seal radially. Because of the limited height of the tool disk it is not possible to use the shape of a semi-sphere for the sheet. Therefore a shape is used, using two curvatures, as shown in figure E.5. The curvature with R_1 starts at the mounting ring in axial direction. This curvature is tangentially connected to the second curvature with R_2 , to prevent a large increase in stress on the border. The stress levels are given in figure E.6. A small increase in stress is showing at the border between the two curvatures. Because of

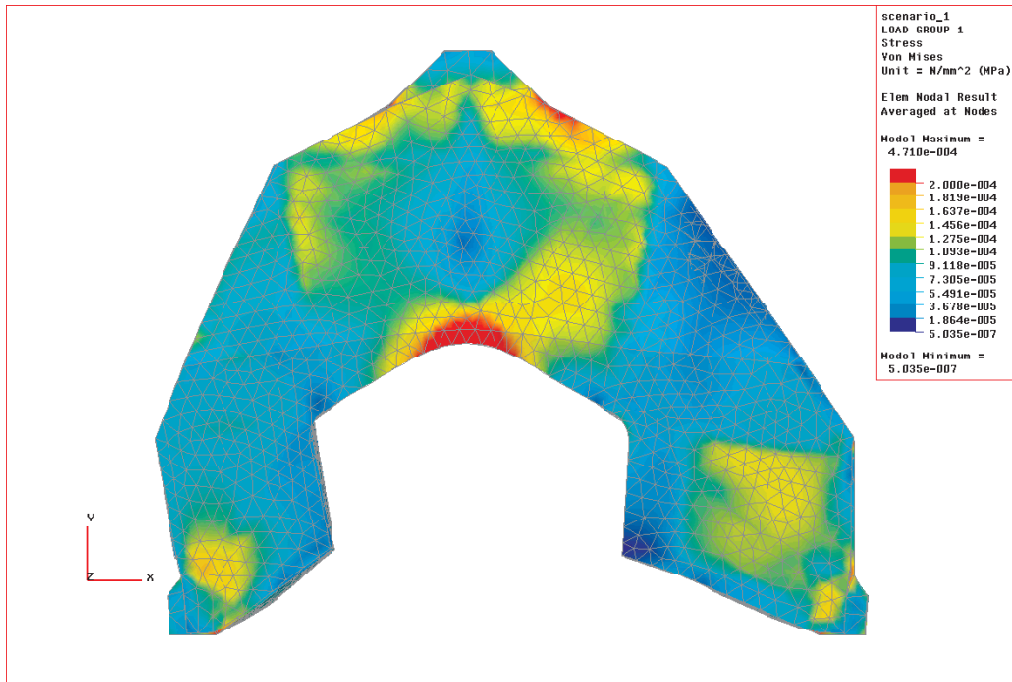


Figure E.1: Y-stiffness = $3.3 \cdot 10^8 N/m$

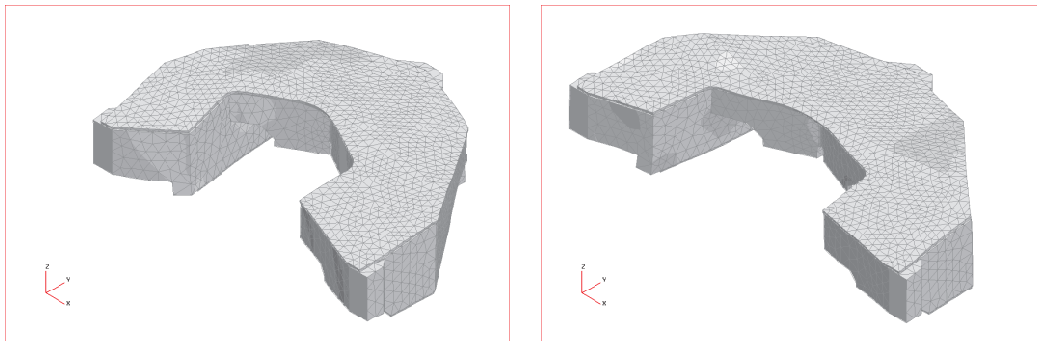


Figure E.2: First eigenmode at 257 Hz.

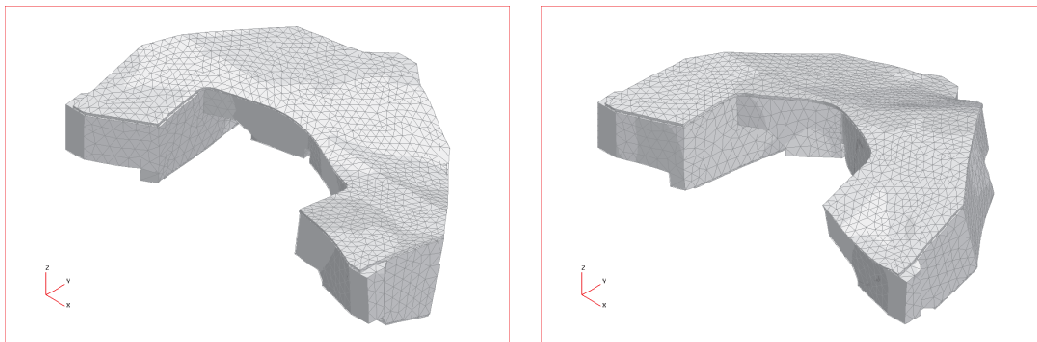


Figure E.3: Second eigenmode at 462 Hz.

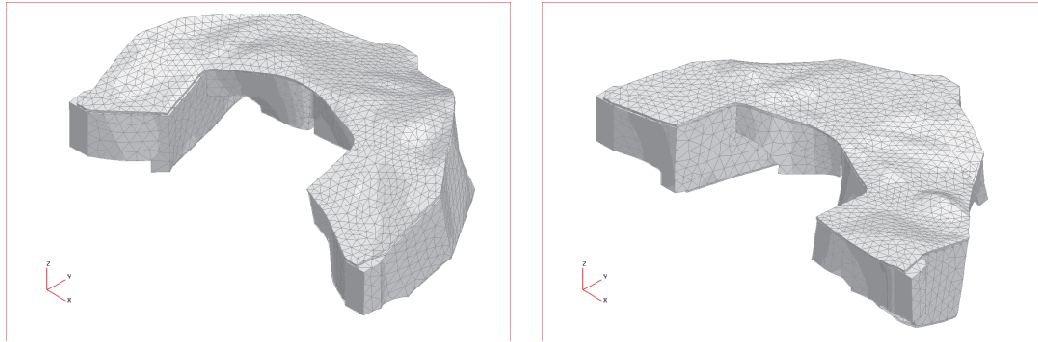


Figure E.4: Third eigenmode at 582 Hz.

the correct chosen shape a 2 mm thick aluminum sheet can hold an overpressure of 1 bar at the upper side. The maximum stress level is 46 MPa, which is acceptable.

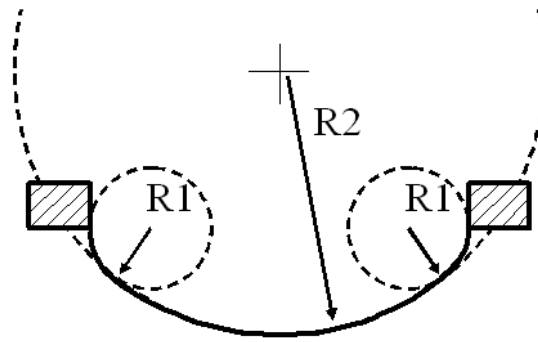


Figure E.5: Shape of sheet using two curvatures

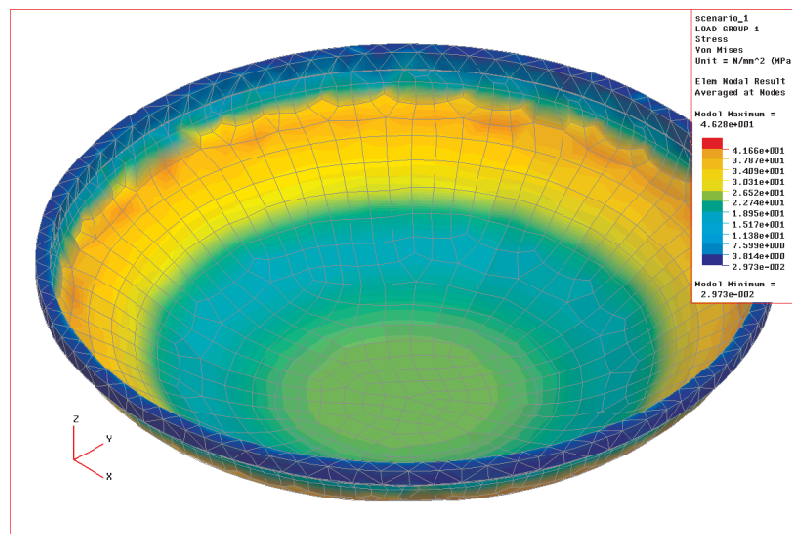


Figure E.6: $\sigma_{max} = 46 \text{ MPa}$ with $\Delta p = 1 \text{ bar}$

E.4 Membranes

When the outer and inner ring of the membrane are exactly axially aligned, the radial stiffness of the membrane is very high, $c_{rad,max} = 38 \cdot 10^7 N/m$. However due to manufacturing tolerances this will never be the case. There will always be some amount of axial offset. FEM-calculations are made to investigate the radial and axial stiffness of the membranes at an axial offset. Figure E.7 shows the maximum stress of 8 MPa when an axial offset of 0.01 mm is applied. This level is acceptable for the steel membrane, so why not allow a larger axial offset? The radial stiffness is reduced from $c_{rad,max} = 38 \cdot 10^7 N/m$ to $c_{rad} = 0.9 \cdot 10^7 N/m$. A larger increase in offset will result in an unacceptable low radial stiffness. The local axial stiffness - at the offset of 0.01 mm - is $5.3 \cdot 10^3 N/m$. The force on the tool drive caused by the stiffness of the two membranes is little more than 0.05 N for a 10 μm stroke.

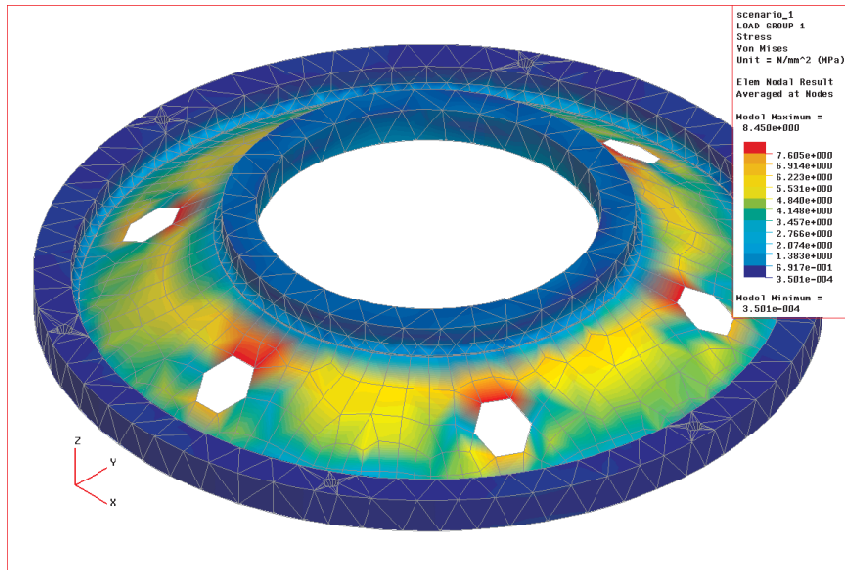


Figure E.7: Membrane: $c_{ax} = 5.3 \cdot 10^3 N/m$, $c_{rad} = 0.9 \cdot 10^7 N/m$, $\sigma_{max} = 8.0 MPa$

E.5 X-frame airbearings

To assure a proper working airbearing, the bottom side of the bearing, as described in 6.7, should be flat enough even when the air is flowing through. Because the airbearings surfaces on the edge of the bottom side are pushing the airbearing of the ground, and the vacuum chamber compensates this force by pulling the bearing down, a momentum on the air bearing is applied. This will cause the airbearing to bend, looking from the short side. Therefore six high plates are applied parallel to the short side. These plates are very suited to prevent the momentum to cause a lot of deflection. This deflection can cause the bottom side of the bearing to be convex, this will reduce the bearing stiffness and increases the change of the bearing running into the under laying surface. Figure E.8 shows the stress levels in the airbearing. The increase in stress at the top middle of the six high plates show the need for these plates. The flatness of the airbearing at the bottom side is $0.84 \mu m$, which is sufficient for the $5 \mu m$ air gap.

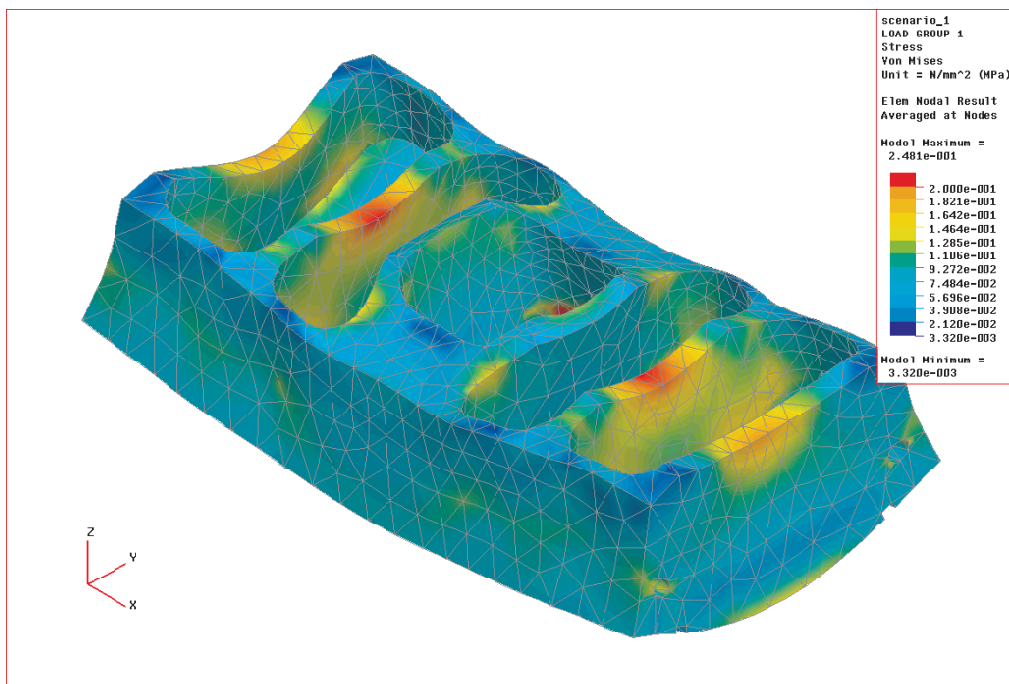


Figure E.8: Stresses on airbearing during airflow

Appendix F

Calculations

F.1 Stiffness related to overhanging length

When a body, as shown in figure F.1, is suspended on two spring with stiffness c , the deflection of the point on which the force F is acting is increased if F is not between the two springs. The distance between the two springs is L and the overhanging length is a . The two springs can be replaced by a single spring with stiffness c_t at the position of F . Figure F.2 shows the decrease in relative stiffness with an increase in overhanging length a . It shows the importance to minimize a in order to keep a stiff construction. The curve in figure F.2 can be calculated with

$$\frac{c_t}{c} = 1 / (2 \frac{a^2}{L} + 2 \frac{a}{L} + 1) \quad (\text{F.1})$$

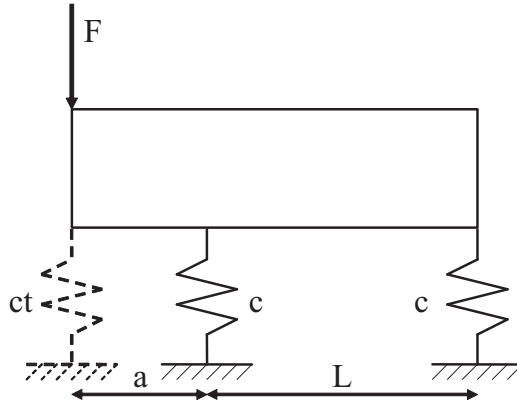


Figure F.1: Force applied on body at distance a from nearest suspension

F.2 Tool spindle accuracy model

To investigate if the desired accuracy can be produced, a simple model is made using the methode as described in [TUeo3]. Because of the partly parallel structural loop, a kinematic model can be made as shown in figure F.3. It shows a schematic view of the tool spindle unit. The movement the disk can make on the granite base is represented by slide a . The movement made by the tool drive and rotor is represented by slide b . The distance between the two slides is c in z-direction and d in y-direction.

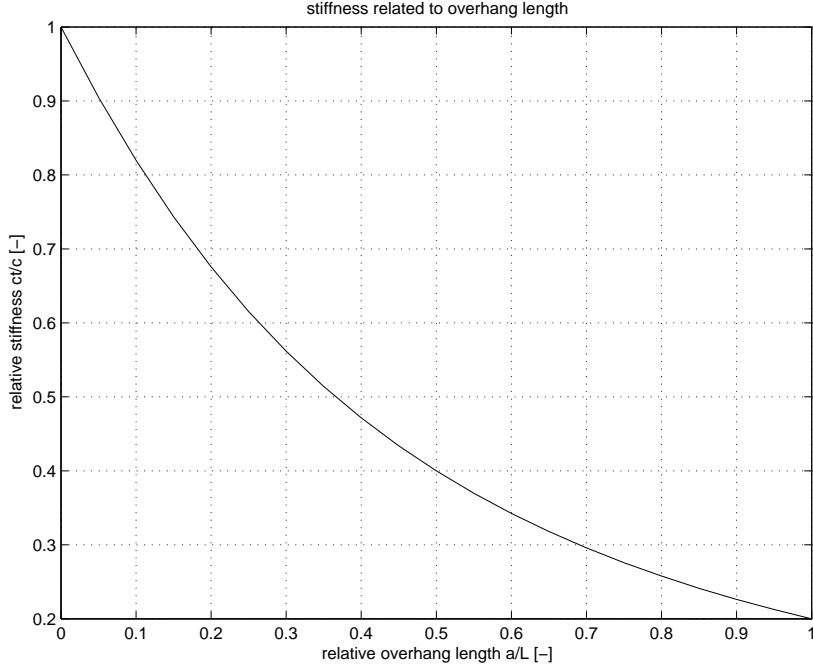


Figure F.2: Relative overhang length versus relative stiffness

The distance between slide b and the tooltip is e . Translation and rotational errors for slide a are given with

$${}_a\vec{T} = ({}_aT_{x,a} \ {}_aT_{y,a} \ {}_aT_z)^T \quad (\text{F.2})$$

$${}_a\vec{R} = ({}_aR_{x,a} \ {}_aR_{y,a} \ {}_aR_z)^T \quad (\text{F.3})$$

where the a stands for the slide, T or R stands for either a translation or rotational error, and x , y or z stands for the direction of the error. The T -components influence the position of the tooltip directly, the R -components are doing this using the local position vector, i. e. the distance between the slide and the tooltip. For both the slides the local position vectors are

$${}_a\vec{P} = (0 \quad d+e \quad c)^T \quad (\text{F.4})$$

$${}_b\vec{P} = (0 \quad e \quad 0)^T \quad (\text{F.5})$$

where a and b stands for the described slide. Now the errors of both the slides and the total error $d\vec{P}$ can be calculated.

$$d\vec{P} = d\vec{P}_a + d\vec{P}_b \quad (\text{F.6})$$

$$d\vec{P}_a = {}_a\vec{R} \times {}_a\vec{P} + {}_a\vec{T} \quad (\text{F.7})$$

$$d\vec{P}_b = {}_b\vec{R} \times {}_b\vec{P} + {}_b\vec{T} \quad (\text{F.8})$$

For the tool spindle unit $d\vec{P}$ is given by F.9 and using the data given in tabel F.1 the maximum off axis error is $0.68 \mu\text{m}$ and the height error is $0.30 \mu\text{m}$.

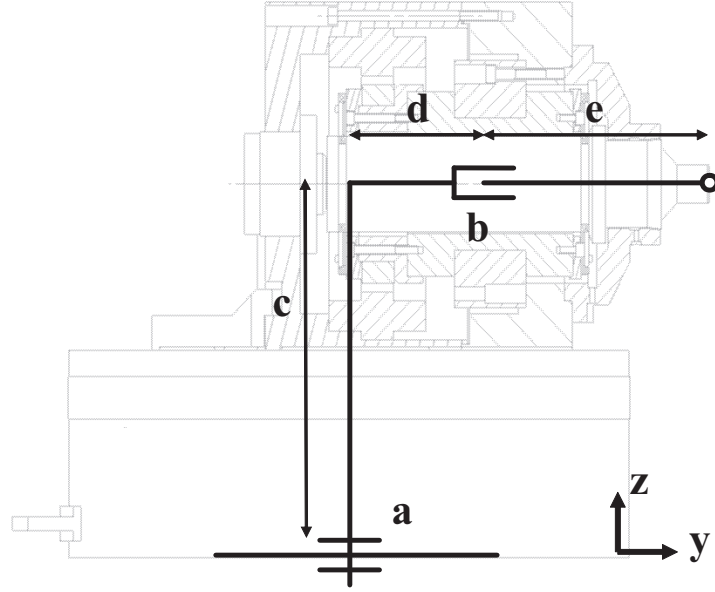


Figure F.3: Accuracy model

$$d\vec{P} = \begin{pmatrix} {}_aR_y \cdot c - {}_aR_z \cdot (d + e) + {}_aT_x - {}_bR_z \cdot e + {}_bT_x & = & 141 + 66 + 85 + 130 + 100 \\ -{}_aR_x \cdot c + {}_aT_y + {}_bT_y & = & 141 + 85 + 74 \\ {}_aR_x \cdot (d + e) + {}_aT_z + {}_bR_x \cdot e + {}_bT_z & = & 146 + 50 + 133 + 100 \end{pmatrix} \quad (\text{F.9})$$

Error	Description	Size [nm] or [μrad]
${}_aT_x$	Position error of y-slide (35) + radial disk airbearing error (50)	85
${}_aT_y$	Position error of y-slide (35) + radial disk airbearing error (50)	85
${}_aT_z$	Axial disk airbearing error	50
${}_aR_x$	Tilting caused by non-horizontal granite base	0.66
${}_aR_y$	Tilting caused by non-horizontal granite base	0.66
${}_aR_z$	Rotational error y-slide + accuracy angle measurement system	0.30
${}_bT_x$	Tooltip runout error relative to the spindle stator	100
${}_bT_y$	Tooltip runout error relative to the spindle stator	100
${}_bT_z$	Tool length change due to temperature change	150
${}_bR_x$	Tilt of tool drive in stator	1.0
${}_bR_y$	Zero because of rotating tool	0
${}_bR_z$	Tilt of tool drive in stator	1.0

Table F.1: Errors used in accuracy model

Appendix G

Alternative machine designs

G.1 Alternative 1

The first alternative machine design features a hydrostatic x-guideway, similar to the one on the Precitech Nanoform, see figure G.1. The guideway is rotated 90° compared to the normal way of mounting such a guideway. This way the guideway has got its highest stiffness in y-direction and this increases the process structural loop stiffness. Because the guideway consists of one solid piece it can not be placed at workpiece spindle level centered on the workpiece. Therefore the guideway is placed at the front side of the horizontal granite slab. This leaves a lot of open space near the workpiece, but this makes the position of the tool spindle very sensitive for tilting of the guideway in R_z , because of the long distance between the guideway and the workpiece. Also part of the y-direction stiffness is lost because the y-slide drive force is not applied at the centre line of the guideway. If the y-slide is actuated a momentum is created on the guideway in R_x -direction. The tool spindle disk uses an axial airbearing preloaded with underpressure. Because of the sensitivity for guideway tilt and the only partly increase in y-stiffness this alternative was dismissed.

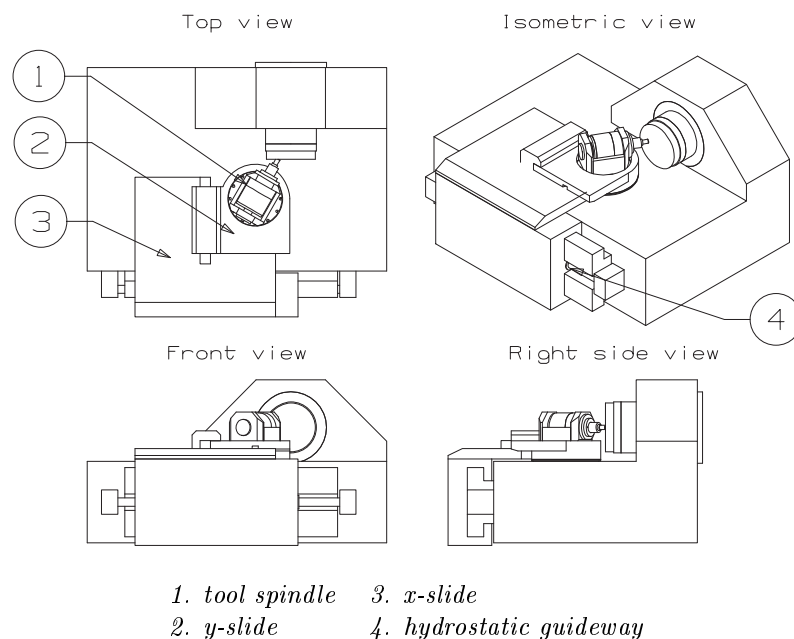


Figure G.1: Alternative 1

G.2 Alternative 2

By mounting the hydrostatic guideway in a traditional way, the distance between the y-slide drive force and the y-direction bearings of the x-slide is decreased and thus reducing the created momentum, see figure G.2. However the highest stiffness of the guideway is used in the z-direction, so this alternative also does not make advantage of the guideways full potential. The tool spindle disk is preloaded with two brackets that are connected to the y-slide. They press through the y-slide onto the tool spindle disk. This way the brackets do not have to rotate, only translate in x- and y-direction. The brackets are also supported at the bottom of the horizontal granite slab, directly beneath the connection points on the y-slide. This way only a force is applied on the slab and not a momentum. The bottom of the slab should be flat and smooth enough to function as a bearing surface. Because of the high preload force (≈ 5000 N) needed to get a stiff bearing, large and heavy brackets are needed and this mass is moving with the relative fast y-slide. So this will have its negative influence on the dynamics.

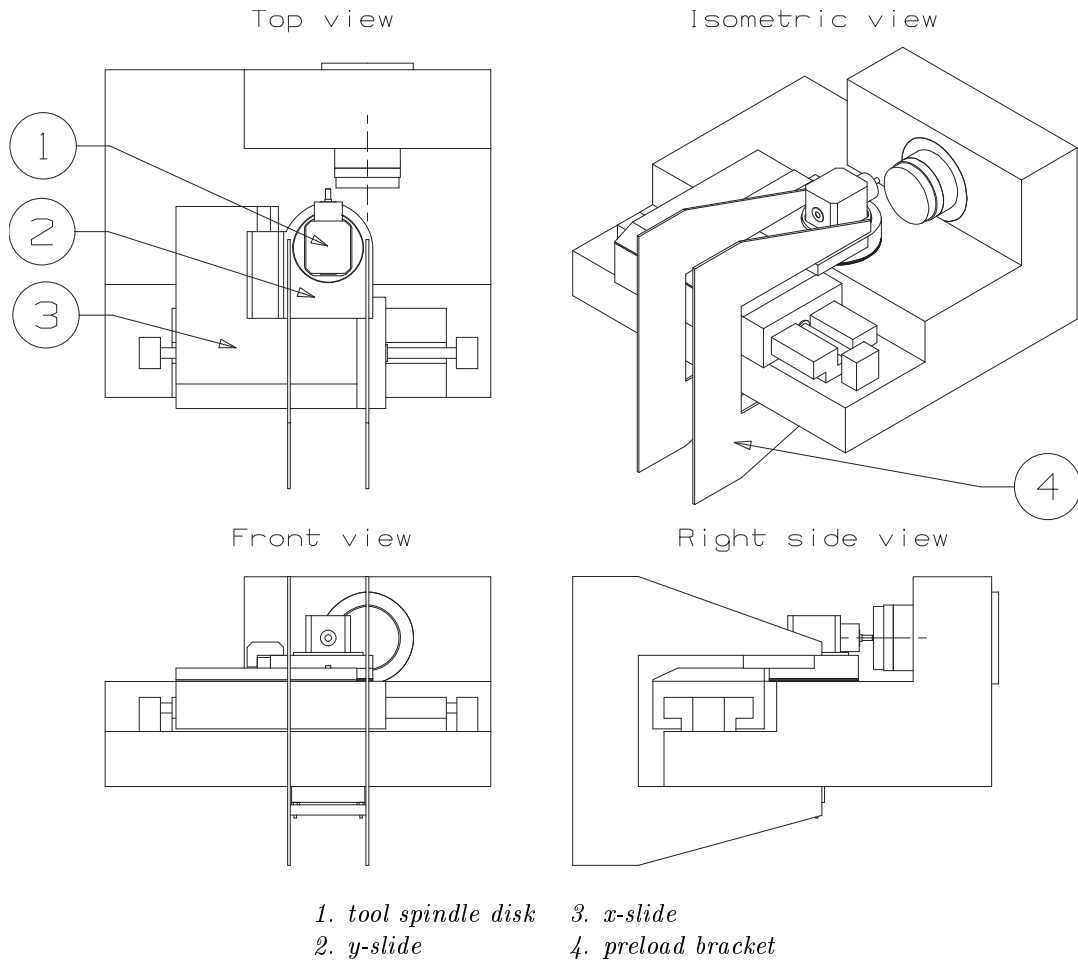
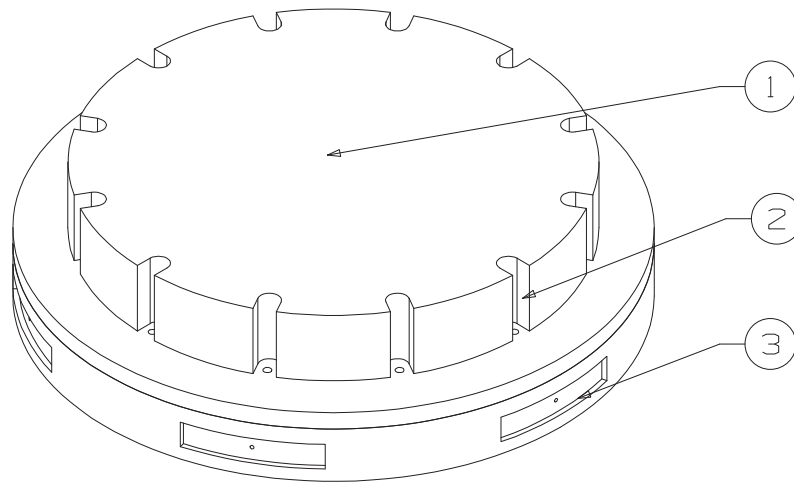


Figure G.2: Alternative 2

Figure G.3 and G.4 show the tool spindle disk that is suspended with an hydrostatic oil bearing. Oil bearings can operate with a larger gap than airbearings, $30 \mu m$ instead of $5 \mu m$. The applied pressure of about 70 bar is much higher than the 5 or 6 bar with airbearings, resulting in smaller bearings. However, because of the larger gap, the preload force has to be larger. [Row83] showed that the stiffness of an hydrostatic bearing is given by

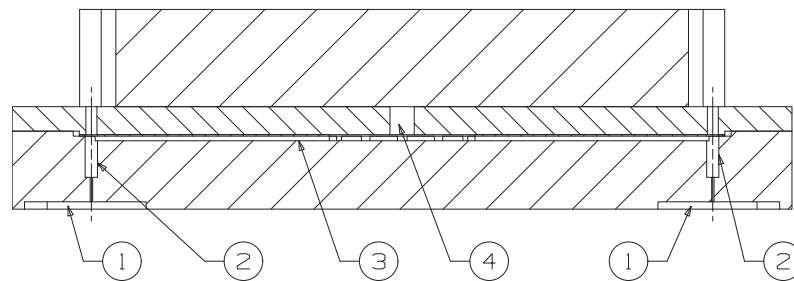
$$c = C \cdot \frac{p_s \cdot A}{h} \quad (\text{G.1})$$

C is a constant depending on the shape of the bearing and the restriction used, p_s is the supply pressure, A the bearing surface and h the gap height. Figure G.3 shows the disk on which the tool spindle will be mounted (1). On the edge of this disk slots are made (2), so bolts may be placed in the underlaying holes. Also the radial oil bearing pockets are shown (3). Figure G.4 shows the axial oil bearing pockets (1). There are six pockets at the bottom to provide tilting stiffness to the disk. The restriction (2) consists of a very narrow hole and a larger threaded hole. A bolt may be placed in the threaded hole to act as a restriction. This way the flow of oil through the bearings, both the axial and the radial bearings, can be adjusted. This way the bearing performance can be optimized. The oil flow enters the disk at the central oil canal (4) and is then divided into different oil canals (3) to each of the bearing pockets.



1. tool spindle mounting face 3. radial bearing pocket
2. slots for adjustment screws

Figure G.3: Tool disk with hydrostatic bearing, isometric view



1. axial bearing pocket 3. oil canal
2. restrictor 4. central oil canal

Figure G.4: Tool disk with hydrostatic bearing, section view

G.3 Alternative 3

This alternative has got a vertical workpiece spindle axis. This way operating the grinder is made easier. The x-slide is supported in z-direction at the workpiece surface level. This significantly decreases the influence of x-slide tilt in Ry-direction. The tool spindle disk is preloaded by a bracket, pushing onto a thin sheet of metal connected to the z-slide. Just beneath the thin sheet a bearing surface is made on top of the tool spindle disk. This way the disk is preloaded, without using a lot of extra material on the z-slide to deal with the large preload force, only a sheet is needed. By connecting the bracket to the z-slide, it does not have to rotate with the tool spindle disk, but its mass still has to be moved when actuating the fast z-slide. The vertical setup also has its disadvantages. First of all the small base and the large height creates difficulties when the grinder is placed onto isolators. In order to get a stable system the isolators should be far apart and the machine will need a lot of room in the workshop. Secondly when grinding concave lenses chips may gather inside the concave and can act as an uncontrolled abrasive. A horizontal setup will wash away the chips easily.

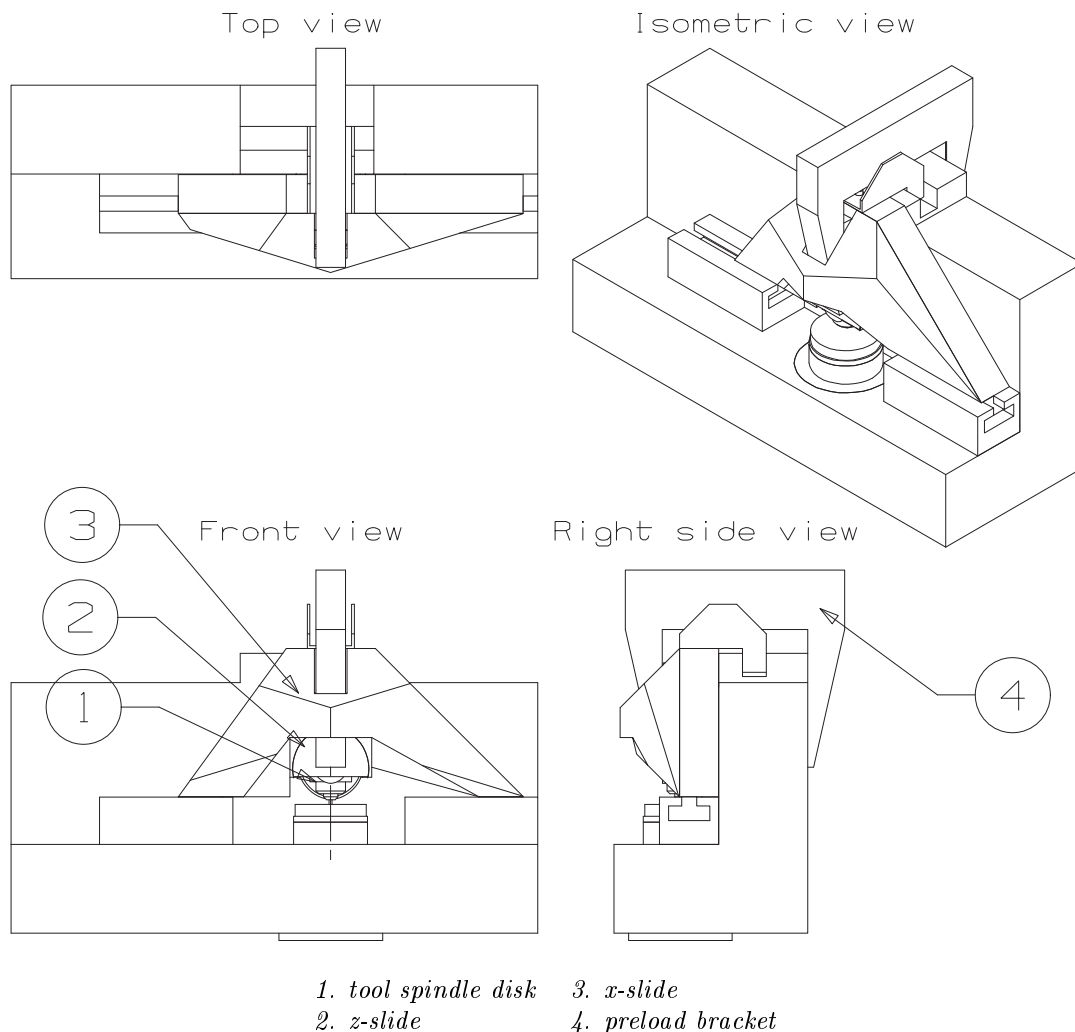


Figure G.5: Alternative 3

G.4 Alternative spindle design

G.4.1 Alternative spindle design 1

This alternative spindle design features the second spindle concept, the one that uses an aerostatic bearing for the tool drive, see chapter 5. Figure G.6 shows the air spindle stator consisting of three elements. On the outside there are two rings, that house the front and back airbearing surfaces, and in the middle there is the motor stator. This way the front and back airbearing are far apart, so the rotor has high tilting stiffness. And because the space between the two ring bearings is filled by the motor, room is spared. Also disturbing radial forces of the motor can be properly dealt with by both bearings. If the motor was placed at the back of the stator the disturbing radial forces would have caused the same situation as described in F.2 and the bearings could have provided far less stiffness to resist the radial forces. The voice coil is placed at the back on the centre line. The stator is placed inside the tool spindle holder, completing the unit. The three stator parts should be aligned very well to prevent the rotor from running into the stator at the airbearing surfaces.

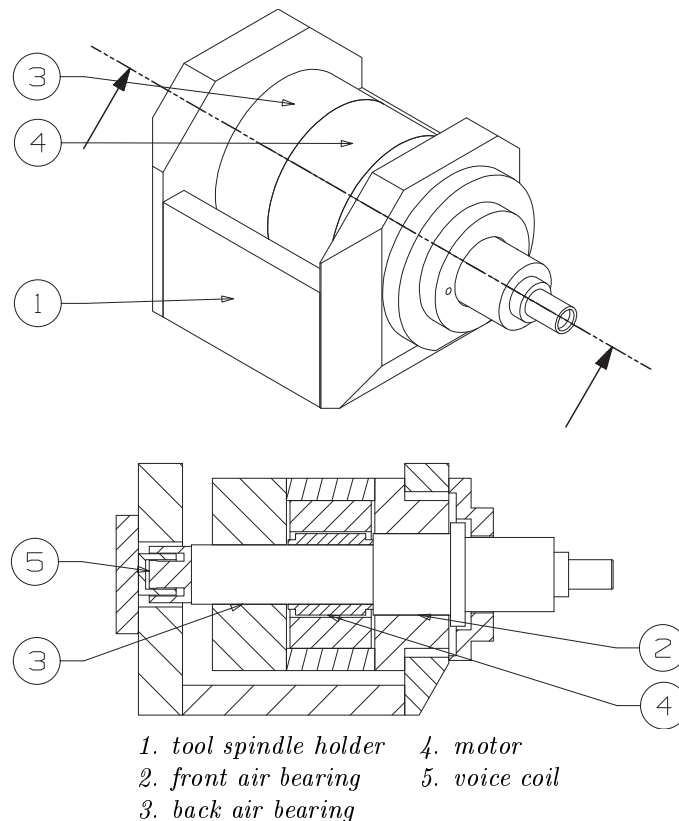


Figure G.6: Alternative spindle design 1: aerostatic tool drive bearing

G.4.2 Alternative spindle design 2

This alternative spindle design has got the entire voice coil inside the rotor. Figure G.7 shows the rotor of the tool spindle. A large bore provides space for the tool drive. The tool drive is suspended to the rotor with two membranes. At the back of the tool drive the voice coil is placed. This setup needs no extra space behind the rotor for the tool drive actuator, resulting in a smaller tool spindle. However this concepts features some difficulties. To get the required electrical current to the coil, a connection with the fixed world is needed. The possibility of a slip ring has been investigated. There

are very few slip rings available that are suited for speeds up to 7000 rpm. These rings have a small diameter, to reduce the peripheral velocity. Because of this, such a ring can not be mounted laterally to the rotor, so extra space is needed at the back of the rotor. The physical contact between the slip ring rotor and stator introduces the problem of wear. The investigated slip ring has got a life span of $100 \cdot 10^6$ revolutions. This means that when operating the grinder 40 hours per week at 5000 rpm, the slip ring has to be replaced every two months. Also a slip ring introduces electrical noise that may influence the performance of the voice coil. This influence should be investigated, adding more complexity to a grinding experiment.

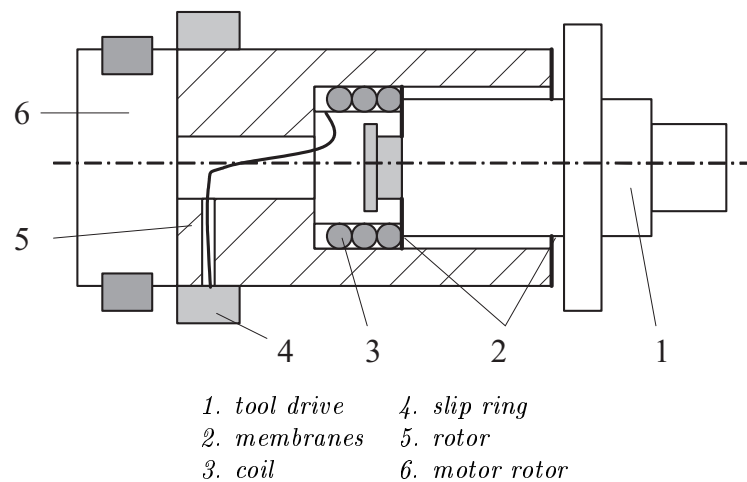


Figure G.7: Alternative spindle design 2: using a slip ring

Appendix H

Materials

H.1 Optical materials

Material	E [GPa]	K [MPa/ $\sqrt{(m)}$]	H [GPa]	d_c [nm]
BK7	81	0.86	5.2	64
Fused silica	73	0.75	5.6	35
Soda-lime	72	0.7	5.9	25

Table H.1: Properties of materials used for optical components

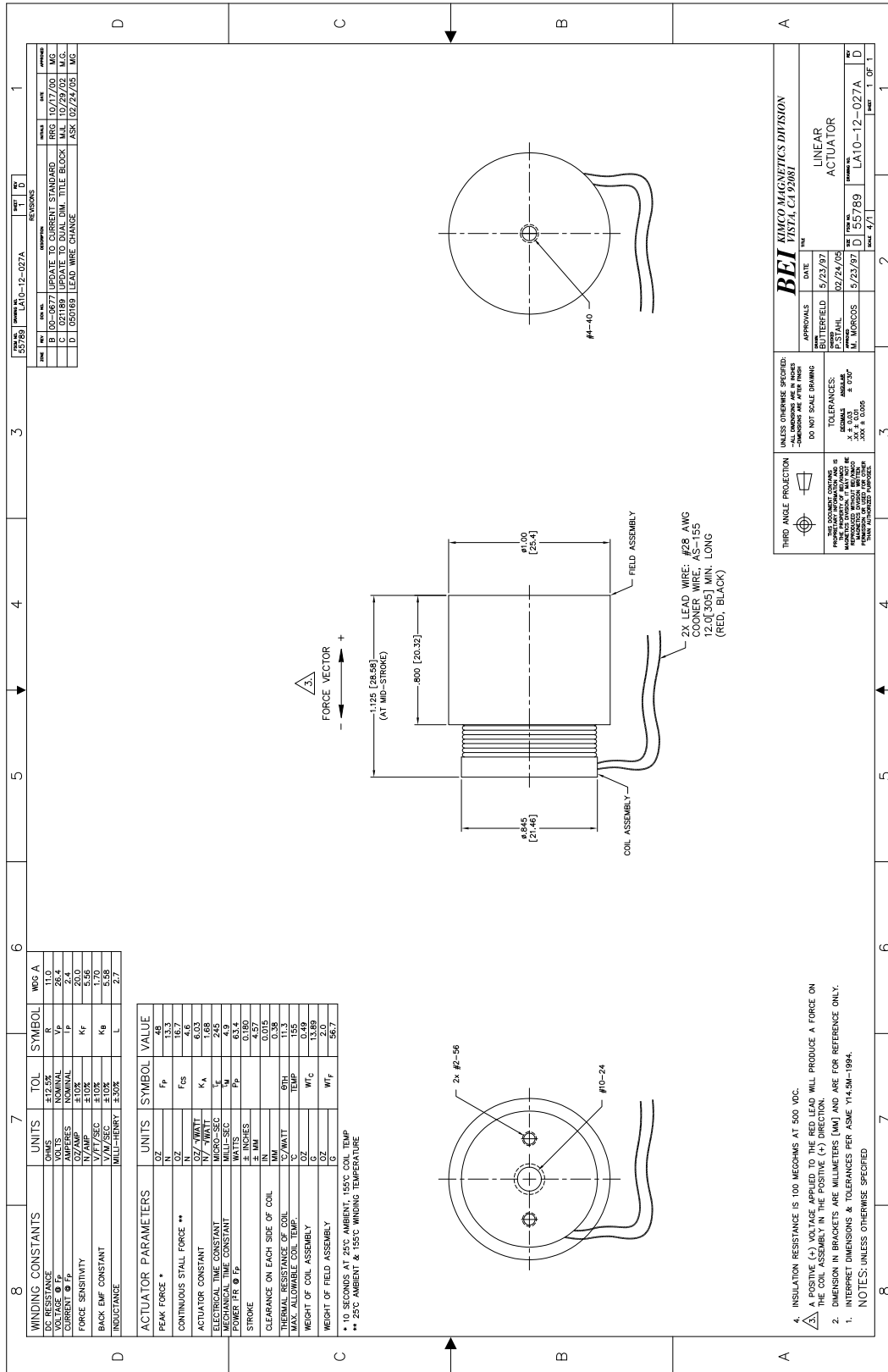
Here some properties of a number of glasses are given. Shown are the Youngs modulus E , the toughness K and the hardness H . Also the critical depth of cut d_c is given. A small d_c means a brittle material. For the greater part, brittle material behavior is caused by a high hardness and a low toughness.

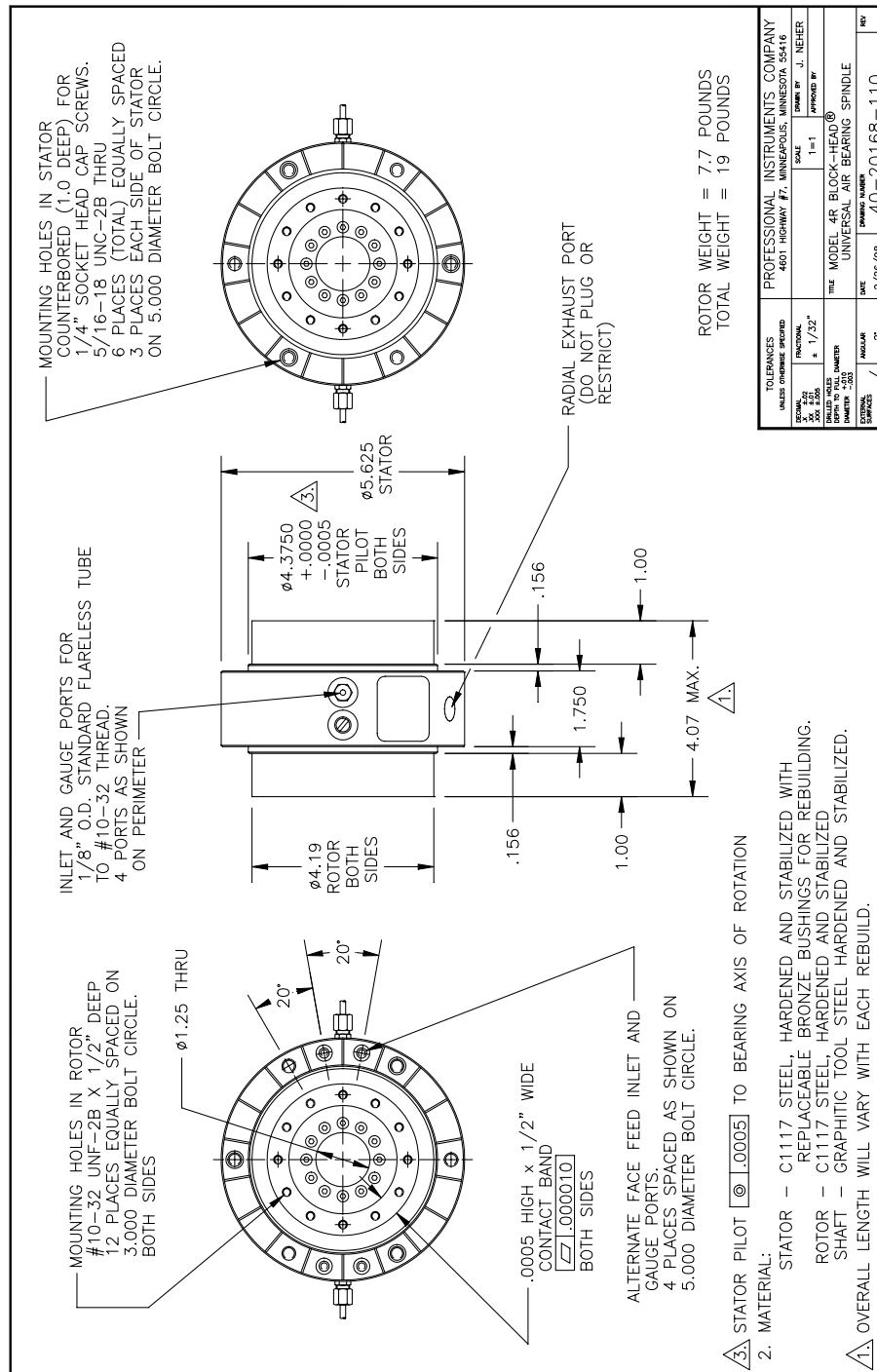
A commonly used material for optical components is BK7. The way of giving material such a name was first developed by Schott, Germany. The B stands for borosilicate. The K means it is a crown glass and this gives a certain range of values for the two most important optical properties of the material, namely the refractive index, n_d and the Abbe number, ν_d . The refractive index n_d gives the refractive power of the glass relative to air, which has a n_d of 1. The Abbe number ν_d is a measure for the dispersion of the material, i.e. the difference in refraction for different wavelengths. For crown glass those properties are $n_d > 1.60$ and $\nu_d > 50$, or $n_d < 1.60$ and $\nu_d > 55$. Finally the number 7 of BK7 means it is the seventh material developed in its category, [Kar93].

Appendix I

Data sheets

This appendix contains the data sheets of some of the components used in the grinder design. There are datasheets of the voice coil, the Blockhead air spindle used for the tool spindle, the Lion Precision inductive measurement system, the granite used for the machine base, the environment isolators and the Nanogrid measurement system.





ECL100 Linear Output Eddy Current Driver

Precision displacement measurement; new, easy to use design.

The ECL100 is small, easily mounted and provides the high performance levels you need in your application. It works with all Lion Precision Inductive probes with ranges from 0.5-15mm.

Performance

- Non-Linearity: $\pm 0.25\%FS$
- Resolution: $0.004\%FS$
- Temp. Coefficient: $0.04\%FS/^{\circ}C$
- Frequency Response to 80kHz
- Output: 0-10VDC and 0-20mA

Features

- Local and Remote Zero
- 12-24VDC Input
- Range Indicating LEDs
- Small DIN Rail Mounting
- TEDS On Board
- Synchronization of Multiple Units
- User Calibration Adjustments



Probes

Choose from our four standard body styles:

Core unit features the smallest physical size for limited access applications.

Smooth body has the strength of a stainless steel housing for clamp or set screw mounting and easy adjustment of axial position.

Threaded body provides a threaded, stainless steel housing for precise adjustment of axial position in a threaded mounting hole or a through hole using the two lock nuts provided.

Bulkhead body's flanged, stainless steel housing gives you easy axial position repeatability in a threaded or through hole.

Custom Probes

All body styles are built from the same core unit. Custom body styles are turned around quickly to get you up and running with exactly what you need in your application.

Core Unit



Smooth



Threaded



Bulkhead



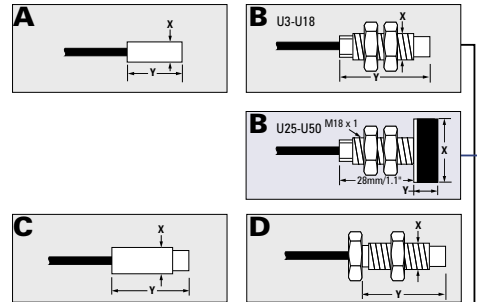
563 Shoreview Park Rd.
St. Paul, MN 55126
651-484-6544
www.lionprecision.com

Document LL02-0010 08-2004

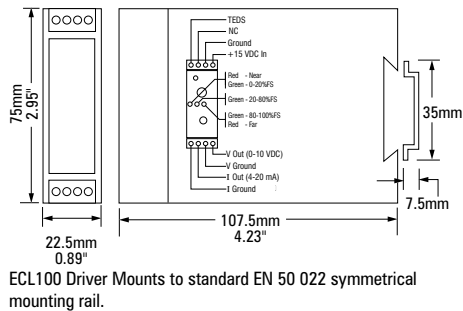
Figure I.3: Inductive measurement datasheet 1/2

ECL100 Driver Specifications:*		
Resolution: RMS @ mid-scale	DC-1kHz	0.004%FS
	DC-10kHz	0.008%FS
	DC-80kHz	0.06%FS
Non-linearity		±0.25%FS
Probe Temperature Coefficient		±0.04%FS/°C (±0.05%FS/°C for U3) from -25°C to +125°C† output @ mid-scale
Driver Input Power		+12 to +24VDC 130mA @ 15V
Driver Outputs	Voltage	0-10VDC
	Current	0-20mA
Operating Temperature:	Std. Probes	-25°C to +125°C†
	Ext. Temp. Probes	-25°C to +200°C†
	Driver	0°C to +65°C
Probe Cables	Length	3 meters
	Jacket Material	Std. Temp. PUR
		Ext. Temp. TEFLON
Ratings	Driver	IP40 (CE Pending)
	Probes	Std. Temp. - IP67 Ext. Temp. - IP63
Driver Dimensions	Height	75mm / 2.95"
	Width	22.5mm / 0.89"
	Depth	107.5mm / 4.23"
	Weight	103g / 3.7oz.
* Performance data taken with standard unshielded probes, 15VDC input, normal room ambient, 6061 aluminum target. Specs also apply to 4140 and 303 steels.		
† Probes available to less than -75°C with special calibration		

Probe Range and Resolution:*					
Probe Model	Range mm/inch	Offset mm/inch	Resolution $\mu\text{m}/\mu\text{inch}$		
			1kHz	10kHz	80kHz
U3	0.50/0.020	0.05/0.002	0.02/0.8	0.04/1.6	0.30/13
U5	1.25/0.050	0.25/0.010	0.05/2	0.10/4	0.75/30
U8	2.00/0.080	0.35/0.015	0.08/3	0.16/6	1.20/48
U12	3.50/0.140	0.60/0.025	0.14/6	0.28/11	2.10/84
U18	5.00/0.200	0.75/0.030	0.20/8	0.41/16	3.05/120
U25	8.00/0.320	1.25/0.050	0.28/11	0.57/22	4.88/192
U38	12.5/0.500	1.50/0.060	0.48/19	0.96/38	7.16/282
U50	15.0/0.600	2.00/0.080	0.66/26	1.32/52	9.91/390
*Specifications for 6061 aluminum and 4140 steel. Other ferrous and nonferrous materials will produce similar results.					



Probe Dimensions					
A	X mm/inch	Y mm/inch	B	X	Y mm/inch
—	—	—	U3B	M3x.5	21.1/0.83
U5A	3.4/0.13	13.0/0.51	U5B	M5x.8	25.0/0.99
U8A	6.2/0.24	14.0/0.55	U8B	M8x1	27.0/1.07
U12A	10.0/0.39	15.0/0.59	U12B	M12x1	29.0/1.15
U18A	15.8/0.62	16.0/0.63	U18B	M18x1	31.0/1.22
—	—	—	U25B	25.0/0.99	15.0/0.59
—	—	—	U38B	38.0/1.50	20.0/0.79
—	—	—	U50B	50.0/1.97	25.0/0.99
C	X mm/inch	Y mm/inch	D	X thread	Y mm/inch
U3C Shoulder	2.92/0.115 3.6/0.14	16/0.63 5/0.20	—	—	—
U5C	4.9/0.193	21/0.83	U5D	M5x.8	23/0.91
U8C	7.9/0.311	23/0.91	U8D	M8x1	25/0.99
U12C	11.9/0.468	25/0.99	U12D	M12x1	27/1.07
U18C	17.9/0.705	27/1.07	U18D	M18x1	31/1.22



ECL100 Driver Mounts to standard EN 50 022 symmetrical mounting rail.

LION
PRECISION

563 Shoreview Park Rd.
St. Paul, MN 55126
651-484-6544
www.lionprecision.com

Figure I.4: Inductive measurement datasheet 2/2

TABLE FOR COMPARISON

Vergleichstabelle / Vergelijkingstabel

Table for Comparison Vergleichstabelle / Vergelijkingstabel		Can be delivered by BoTech BV: Von BoTech BV lieferbar / Door BoTech BV leverbaar:				Properties for comparison only Nur als Vergleichswerte / Waarden ter vergelijking	
		Granite		Silicate Ceramics			
		Granit / Graniet		Silikat-Keramik / Silicaat Keramiek			
		Impala*	African Black* Afrika Schwarz / Afrika Zwart	Type C	Type D	Al ₂ O ₃ (92)	Al
Wasseraufnahme / Waterabsorptie Water absorption	[%]	0,2 – 0,4	0,2 – 0,4	0,0	0,0	0,0	0,0
Rohdichte / Dichtheid Specific Gravity	[10 ³ kg/m ³]	2,9	3,1	2,2	3,2	3,6	2,7
Biegefestigkeit / Buigsterkte Flexural Strength	[N / mm ²]	13	5 - 10	80	250	240	170
Elastizitätsmodul / Elasticiteitsmodulus Modulus Of Elasticity	[10 ³ N/mm ²]	65 - 85	77	80	200	300	69
Druckfestigkeit / Druksterkte Compressive Strength	[N / mm ²]	240	200-300	400	1000	3000	65-200
Lin. Längenausdehnungskoeffizient / Lineaire uitzettingscoëfficiënt Coefficient Of Linear Thermal Expansion	[10 ⁻⁶ K ⁻¹] (20 – 100 °C)	5-6	4-7	0,4	5 - 7	7	23
Spezifische Wärmekapazität / Soortelijke Warmte Specific Heat	[J / kg.K] (20 – 100 °C)	800	800	-	950	960	960
Wärmeleitfähigkeit / Thermische warmtegeleidingscoëfficiënt Thermal Conductivity	[W / m.K]	3,2	2,9-3,5	2	12	21	171
*Values must be seen as indications. (Small) variations in composition lead to variations in properties of this natural product. *Aangegeve Werte sind Richtzahlen. (Geringe) Variationen in der Zusammenstellung führen zu Variationen in den Materialeigenschaften von diesem Naturprodukt. *Weergegeven waarden zijn richtgetallen. (Geringe) variaties in samenstelling leiden tot variaties in de materiaaleigenschappen van dit natuurproduct.							

*Values must be seen as indications. (Small) variations in composition lead to variations in properties of this natural product.
*Aangegeven waarden zijn richtgetallen. (Geringe) variaties in samenstelling leiden tot variaties in de materiaaleigenschappen van dit natuurproduct.
*Weergegeven waarden zijn richtgetallen. (Geringe) variaties in samenstelling leiden tot variaties in de materiaaleigenschappen van dit natuurproduct.



Also available:
✓ Datasheet Impala
✓ Datasheet African Black
✓ Datasheet Carbon Fibre / Epoxy Composites

Figure I.5: Granite datasheet

OPTICAL TABLES

BREADBOARDS & GRID PLATFORMS

HONEYCOMB, GRANITE & RIGID STRUCTURES

ISOLATORS

WORKSTATIONS & ISOLATED PLATFORMS

STRUCTURAL RAILS & CARRIERS

TESTING, ANALYSIS & DESIGN

TECHNICAL REFERENCE

I-2000 LabLegs™

Key Features

Hybrid Chamber Design

- Maximized isolation bandwidth
- Improved center of mass stability
- Better responsiveness
- Compact design

Laminar Flow Damping

- Less amplification at resonance
- Better isolation bandwidth
- Improved settling time

High Accuracy Leveling Valves

- Improved repositioning after disturbance
- Better beam pointing stability
- User control of airflow

Trifilar Pendulum Horizontal Isolation

- Zero-friction for isolation of very low level vibration
- Excellent damping properties



Tie-Bar System



Tie-Bar Caster System

Stabilizer Pneumatic Isolators With Automatic Leveling



I-2000 Stabilizer™ vibration isolators offer a vibration isolation design that has set the standard in performance and convenience.

Exclusive laminar flow damping is the heart of the Stabilizer's unparalleled performance. Unlike single damping orifices, the Stabilizer employs thousands of tiny orifices, resulting in greater damping efficiency overall. Combined with the hybrid chamber design to minimize air volume between piston motion and damper air flow, the Stabilizer protects applications like no other.

Numerous performance advantages include:

- Faster settling time for large and small magnitude disturbances.
- Greater high-center-of-mass stability—a must for heavy equipment.
- Lower natural frequency for superior protection against hard-to-control low frequencies below 5 Hz.

- Minimized amplification at resonance, thereby maximizing the system's stability overall.

Installation is fast and easy with patented, self-centering pistons. They automatically center the piston at the top and bottom of its vertical stroke, guaranteeing unrestricted movement for optimal performance. SafeLock™ mounting brackets eliminate the need to precisely align isolators and table holes when attaching the isolator to the table.



I-4000 isolators are available from the Custom Products Group

1248

Figure I.6: Isolator datasheet 1/2

89

Specifications

Isolation Specifications

Model	Vertical Isolation*			Horizontal Isolation*			Amplification at Resonance		Damping Element Airflow	Horz. Damping	Load per Isolator [lb (kg)]
	Res (Hz)	5Hz (%)	10Hz (%)	Res (Hz)	5Hz (%)	10Hz (%)	Vert (dB)	Horz (dB)			
I-2000 Series	1	96	99	1.5	85	95	13	13	Normal	Oil	2000 (900)

* Isolation at full load

Physical Specifications

Height [in. (mm)]	10 (254), 13.5 (343), 16 (406), 19.5 (495), 22 (559), 23.5 (597), 28 (711)
Height Adjustment [in. (mm)]	1.3 (33)
Valve	IPV-S1
Re-leveling Accuracy [in. (mm)]	±0.010 (±.250)
Settling Time	1.5 sec. (typical)
Max. Air Pressure [psi (kg/cm²)]	20–85 (0.7–6.0)
Self Centering	Yes

Ordering Information

Model	Number of Isolators	Load Capacity [lb (kg)]
I-2000-4H	4	660 (300)–8000 (3640)
I-2000-6H	6	990 (450)–12000 (5455)
I-2000-8H	8	1320 (600)–16000 (7280)

Order using this general format:

I-2000-NH
Number of Isolators per set Isolator height (inches)

Example: I-2000-428 designates a system with four 28 in. isolators. To add a tie-bar caster system for a 4 ft x 8 ft table, add -TC after the Model number and order tie-bars and/or casters as below:

- 1) I-2000-428-TC
- 2) TBC-48

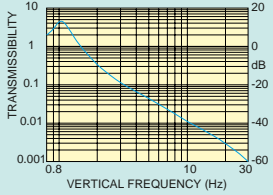
Tie-Bar/Caster System Options

Standard tie-bar/caster systems are available for the table sizes listed below. Select from the Model numbers below to add a standard load tie-bar system—with or without casters—to your table. For other table sizes, please contact Newport for price and delivery.

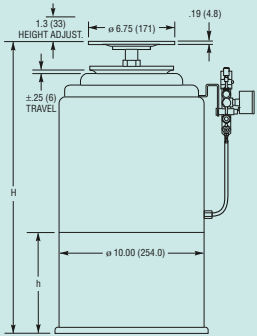
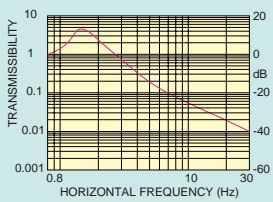
Tie-Bars with Casters		
Tables [ft (m)]	Model (Metric)	
4 (1.2) x 6 (1.8)	TBC-46 (M-TBC-46)	
4 (1.2) x 8 (2.4)	TBC-48 (M-TBC-48)	
4 (1.2) x 10 (3.0)	TBC-410 (M-TBC-410)	
4 (1.2) x 12 (3.6)	TBC-412 (M-TBC-412)	
5 (1.5) x 6 (1.8)	TBC-56 (M-TBC-56)	
5 (1.5) x 8 (2.4)	TBC-58 (M-TBC-58)	
5 (1.5) x 10 (3.0)	TBC-510 (M-TBC-510)	
5 (1.5) x 12 (3.6)	TBC-512 (M-TBC-512)	

Tie-Bars only		
Tables [ft (m)]	Model (Metric)	
4 (1.2) x 6 (1.8)	TB-46 (M-TB-46)	
4 (1.2) x 8 (2.4)	TB-48 (M-TB-48)	
4 (1.2) x 10 (3.0)	TB-410 (M-TB-410)	
4 (1.2) x 12 (3.6)	TB-412 (M-TB-412)	
5 (1.5) x 6 (1.8)	TB-56 (M-TB-56)	
5 (1.5) x 8 (2.4)	TB-58 (M-TB-58)	
5 (1.5) x 10 (3.0)	TB-510 (M-TB-510)	
5 (1.5) x 12 (3.6)	TB-512 (M-TB-512)	

Vertical



Horizontal



Other heights available upon request

Model	Dimension [in. (mm)]	
	H	h
I-2000-N10	10.0 (254)	N/A
I-2000-N13.5	13.5 (343)	1.7 (43.2)
I-2000-N16	16.0 (406)	3.8 (96.5)
I-2000-N19.5	19.5 (495)	7.3 (185.4)
I-2000-N22	22.0 (559)	9.8 (248.9)
I-2000-N23.5	23.5 (597)	11.3 (287.0)
I-2000-N28	28.0 (711)	15.8 (401.3)
Other heights available upon request		

Figure I.7: Isolator datasheet 2/2



NanoGrid Planar Encoder System: Model A (High Resolution)

PRODUCT DESCRIPTION

The NanoGrid[®] Planar Encoder System is used to measure 2-dimensional ultra-precise planar displacements. NanoGrid is an XY grid-based encoder system that avoids the turbulence effects which are commonly encountered with laser interferometers or the Abbe errors associated with separate linear scales. NanoGrid captures the precision of laser interferometry within the manufacturing process of the grid and packages it in a lower cost, more usable, and rugged format.

The XY encoder, or grid, has a basic period of 10 microns in both the X and Y directions, and the metrology system generates a measurement period of 5 microns. The NanoGrid's patented tri-phase 90-element detector captures first order laser diffracted signals reflected from the grid. The three signals generated by the detector provide an unambiguous measurement of phase for extremely small movements.

The NanoGrid Model A metrology system is unique in a number of its features, but particularly in the high degree of accurate interpolation that it provides. The NanoGrid sensor and associated high resolution phase processor electronics provide 14 bits of interpolation, corresponding to a measurement resolution of 0.3nm.

Several standard grid sizes are available to meet the requirements of semiconductor equipment manufacturers and other customers. Custom grid sizes can also be purchased for an exact fit.

The standard position output signal is in the form of a 32-bit parallel word. A-quad-B output format can be derived from the 32-bit word via a separate optional board. Yaw (rotation about the axis perpendicular to the plane) can be measured by adding a second single-axis sensor head.

NanoGrid is an excellent choice for submicron ultra precision XY positioning or as a calibration tool for high precision machine tools and stages.



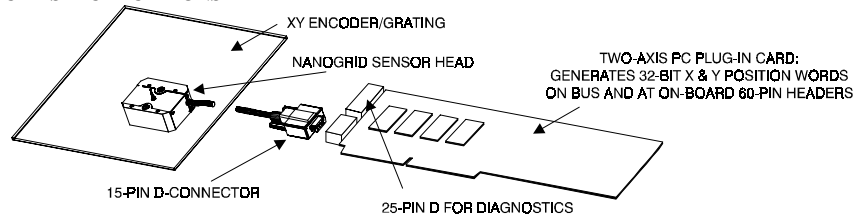
ADVANTAGES

- Sub-nanometer position resolution
- Measurement repeatability of ≤ 5 nm
- Reduce Abbe Error
- Insensitivity to turbulence and atmospheric pressure changes
- Small footprint & low moving mass
- Vacuum compatible units available
- Easy to install; stress-relieved grid mounting included
- 12 mm clearance between grid and sensor head
- Low sensitivity to alignment errors
- Full technical support; customization available

Figure I.8: Nanogrid datasheet 1/2

NanoGrid Model A (High Resolution)

TECHNICAL SPECIFICATIONS



System Performance

Repeatability	±5nm
Accuracy (175mm×175mm)*	±200nm
Accuracy (380mm×380mm)*	±1.0µm
* (Temperature stabilization to ±0.25°C)	
Maximum velocity	700mm/sec
Encoder to sensor head gap	12.0 ±0.1 mm
Measurement area (others available)	40×45mm, 150×150mm 210×210mm, 380×380mm
Operating temperature	+10°C to +40°C
Storage temperature	-20°C to +50°C

NanoGrid Sensor Head

Dimensions	23.5 × 47.0 × 60.5mm
Housing material	6061-T6 aluminum
Light source (785nm)	Class IIIB 3mW laser diode
Weight without cable	110gm
Interface cable	3 m cable, 15-pin connector

Two-Axis High-Resolution Processor

Resolution	LSB = $5\mu\text{m} \div 2^{14} \approx 0.305 \text{ nm}$
Update rate/axis	(parallel out) 375 kHz
Range	~1300 mm (32 bit rollover)
Data age	< 8µsec; stability < 25 nsec
Interfaces	25-pin test connector Two 60-pin parallel connectors PC-compatible 16-bit ISA bus 15-pin HD to Sensor Head
Output format	32-bit parallel word (each axis)
A-quad-B (optional)	Edge rate: 1.875, 3.75, 7.5, 15MHz Resolution: $5\mu\text{m} \div 2^N$; N = 9 to 14; ≈ 0.3 to 9.8 nm Edge-rate & resolution selectable
Mechanical	ISA-compatible 16-bit PC board
Power	+5VDC (+0.25/-0.13 V) @ 2.2 A; (Does not include A-quad-B board) +12VDC ±0.5V @ 120 mA; -12VDC ±0.5V @ 70 mA

NanoGrid Encoder

Pitch (mechanical/optical)	10 µm / 5µm
Soda-lime expansion coefficient:	$7.0 \times 10^{-6}/^\circ\text{C}$
Quartz (fused silica) expansion coeff:	$0.7 \times 10^{-6}/^\circ\text{C}$
Other materials available – consult factory	

System Components

The NanoGrid Model A System consists of a planar encoder (XY grid), sensor head with cable, and 2-axis hi-resolution processor board.

NanoGrid Sensor Head

The NanoGrid Sensor Head contains a single laser diode source and separate optical systems for making planar position measurements. Output signals from the Sensor Head go to the Processor.

Two-Axis High-Resolution Processor

The Two-Axis High-Resolution Processor is a full size, ISA-bus-compatible PC plug-in card. It supplies power to, and receives signals from the NanoGrid Sensor Head via an interface cable. After processing these signals, it generates 32-bit words which describe the position of the encoder relative to the NanoGrid Sensor Head. Binary (TTL) flags and board-mounted LED's indicate excess speed and low signal conditions. An optional daughter board provides an A-quad-B output with selectable resolution.

NanoGrid Encoder

The standard NanoGrid encoder is a 10 µm pitch, 2-dimensional diffraction grating on soda-lime glass. The XY grid can be attached to a metal ring with incorporated flexures that provides kinematic KineFlex mounting with stress relief and ease of installation.

Documentation Package

This package contains dimensional and tolerance information needed to properly locate the NanoGrid sensor head relative to the NanoGrid encoder, instructions for mounting the NanoGrid encoder, and an operating manual.



OPTRA and NanoGrid are registered trademarks and KineFlex is a trademark of OPTRA, Inc.

OPTRA, Inc.

461 Boston St. Topsfield, MA 01983
978-887-6600 FAX: 978-887-0022
info@optra.com or www.optra.com

NanoGrid A.doc
7/20/2000

Figure I.9: Nanogrid datasheet 2/2